KB-STAP Implementation for HFSWR
Contract Number: W7714-060999/001/SV

Maryam Ravan, Oliver Saleh, Raviraj S. Adve,
Kostas Plataniotis and Petros Missailidis

Dept. of Electrical and Computer Engineering
University of Toronto
10 King's College Road
Toronto, Ontario, M5S 3G4, Canada

maryam.ravan@gmail.com
{osaleh, rsadve, kostas}@comm.utoronto.ca ,
polixenaki@yahoo.com

March 2008

Final Report

Abstract

This project deals with the development of knowledge based space-time adaptive processing (KB-STAP) techniques for high frequency surface wave radar (HFSWR). Target detection in HFSWR is fundamentally limited by ionospheric and sea clutter, both of which are well known to be highly non-homogeneous. The goal is to develop an understanding the problem of ionospheric clutter, the formulation of knowledge based approaches to weak target detection, leveraging past work by the researchers into KB-STAP for airborne radar (a significantly more benign problem).

This effort has addressed the problem of STAP for ionospheric clutter in a comprehensive manner. Available STAP algorithms have been tested using measured HFSWR data. Two key contributions of this effort have been the development of a data model of single-bounce ionospheric clutter and the development of an extremely efficient and effective STAP algorithm based on the Fast Fourier Transform approach. It is our sincere belief that the effort undertaken has been extremely successful.

Contents

1 Introduction **1**

2 Preliminaries: Literature Review and Data Analysis **3**

2.1 Literature Review of Data Analysis as Applied to HFSWR 3

2.1.1 Data Modeling 4

2.2 Literature Review of Adaptive Processing as Applied to HFSWR 5

2.3 Preliminary Data Analysis 7

2.3.1 Element-Range Plots 8

2.3.2 Range-Doppler Plots 8

2.3.3 Angle Doppler Plots 11

2.4 Adaptive Processing 13

2.4.1 Data and Processing Model 13

2.4.2 Simulation Results 16

2.5 KB-STAP 17

3 Data Models for Ionospheric Clutter **21**

3.1 Data Model of Fabrizio [1] 21

3.1.1 Signal Processing Model 21

3.1.2 Parameter Estimation 23

3.2 Data Model of Riddolls [2] 28

3.2.1 Path integral formulation of wave packet properties 29

3.2.2 Second-order statistics 31

3.2.3 Modeling the Space-Time-Range Data Cube 32

3.2.4 Simulation Results 33

3.2.5 Summary 34

4 Space-Time Adaptive Processing of Ionospheric Clutter **40**

4.1 Joint Domain Localized Processing 41

4.1.1 Simulation Results 44
4.1.2 Discussion 51
4.2 The Direct Data Domain Algorithm 55
4.3 The Hybrid Algorithm 57
4.4 The Parametric Adaptive Matched Filtering Algorithm 58
4.5 Realistic Target Model 64
4.5.1 Discussion on STAP Algorithms 72
4.6 Fast Fully Adaptive Algorithm 74
4.6.1 System Model 75
4.6.2 Fast Fully Adaptive Algorithm 76
4.6.3 Complexity Analysis 79
4.6.4 Simulation Results 83
4.7 Interleaved FFA Description 86
4.8 Complexity Analysis 90
4.8.1 Unequal Partitions 91
4.8.2 Simulation Results 94
4.8.3 Probability of Detection versus SNR 94
4.9 Summary and Conclusions 98

5 Conclusion **100**

List of Figures

2.1 Element-range power distribution for pulse number 1 9
2.2 Element-range power distribution for pulse number 2000 9
2.3 Range-Doppler power distribution for element number 1 10
2.4 Range-Doppler power distribution for element number 8 10
2.5 Range-Doppler power distribution for element number 13 11
2.6 Angle-Doppler power distribution for range bin 1 12
2.7 Angle-Doppler power distribution for range bin 50 12
2.8 Angle-Doppler power distribution for range bin 100 14
2.9 Angle-Doppler power distribution for range bin 150 14
2.10 Angle-Doppler power distribution for range bin 200 15
2.11 Angle-Doppler power distribution for range bin 225 15
2.12 Output statistic with non-adaptive processing 18
2.13 MSMI statistic as a function of range and Doppler 18
2.14 Comparing adaptive and non-adaptive processing with target within the Bragg line . 19
2.15 Comparing adaptive and non-adaptive processing with target within the ionospheric clutter 19

3.1 Real part of (a) noisy and (b) estimated autocorrelation function. 25
3.2 Real part of (a) measured and (b) estimated autocorrelation function for range bin 220. 26
3.3 real part of (a) measured and (b) estimated autocorrelation function for range bin 140. 27
3.4 real part of (a) measured and (b) estimated autocorrelation function for range bin 180. 27
3.5 (a)Angle of arrival and (b) Doppler frequency spectrum for range bin 220. 28
3.6 (a)Angle of arrival and (b) Doppler frequency spectrum for range bin 140. 29
3.7 (a)Angle of arrival and (b) Doppler frequency spectrum for range bin 180. 29
3.8 (a) Phase power spectrum and (b) autocorrelation function of the signal. 35

3.9 (a) Real and (b) imaginary part of the simulated signal for the range bin 34 when $E(\varphi^2)$ is a random value between 1×10^2 and 2×10^2 35

3.10 (a) Real and (b) imaginary part of simulated signal for the range bin 12 when $E(\varphi^2)$ is a random value between 2×10^2 and 3×10^2 36

3.11 Angle-doppler plot of the simulated signal (a) for the range bins 34 and (b) 12. . . . 36

3.12 (a) Real and (b) imaginary part of measured signal for the range bin 230. 37

3.13 (a) Real and (b) imaginary part of measured signal for the range bin 260. 37

3.14 Angle-doppler plot of the measured signal (a) for the range bins 230 and (b) 260. . . 38

3.15 Doppler-range plot of the simulated signal (a) for antenna element 13 when $E(\varphi^2)$ is in the range of $(1 \sim 2) \times 10^2$ and (b) for antenna element 6 when $E(\varphi^2)$ is in the range of $(2 \sim 3) \times 10^2$. 38

3.16 Doppler-range plot of the measured signal (a) for antenna element 6. 39

3.17 Doppler plot of the (a) simulated signal of range bin 12 and antenna element 6 and (b) measured signal of range bin 230 and antenna element 6 39

4.1 A linear array of point sensors 41

4.2 Localized processing regions in Joint Domain Localized processing. 43

4.3 ΔMSMI versus angle and Doppler spacing ($\eta_a = \eta_d = 3$). Ionospheric clutter region. 46

4.4 ΔMSMI versus angle and Doppler spacing ($\eta_a = \eta_d = 3$). Bragg region. 47

4.5 ΔMSMI versus angle and Doppler spacing ($\eta_a = 3, \eta_d = 5$). Ionospheric clutter region. 47

4.6 ΔMSMI versus angle and Doppler spacing ($\eta_a = 3, \eta_d = 5$). Bragg region. 48

4.7 MSMI statistic (in dB) versus the range cell number for ($\eta_a = \eta_d = 3$). Ionospheric clutter region. 49

4.8 MSMI statistic (in dB) versus the range cell number for ($\eta_a = \eta_d = 3$). Bragg region. 50

4.9 MSMI statistic (in dB) versus the range cell number for ($\eta_a = 3, \eta_d = 7$). Ionospheric clutter region. 50

4.10 MSMI statistic (in dB) versus the range cell number for ($\eta_a = 3, \eta_d = 7$). Bragg region. 51

4.11 MSMI statistic (in dB) versus (in dB) versus the range cell number for ($\eta_a = 3, \eta_d = 7$). Using all range cells in ionospheric clutter region. 52

4.12 A range-Doppler plot of the data-square containing obvious targets. The targets are spread over up to 15 ranges and are at Doppler bin numbers 89, 106, 131, and 151 respectively. 64

4.13 A power profile plot of the identified targets at Doppler bin numbers 89, 106, 131, and 151 respectively. 65

4.14 Results of using the JDL, Adaptive Doppler filter, and Nonadaptive MF algorithms to detect an ideal target with amplitude 35dB inserted into the Ionospheric clutter region. 67

4.15 Results of using the JDL, Adaptive Doppler filter, and Nonadaptive MF algorithms to detect an ideal target with amplitude 45dB inserted into the Ionospheric clutter region. 67

4.16 Results of using the JDL, Adaptive Doppler filter, and Nonadaptive MF algorithms to detect a real target spread over 7 range cells and with amplitude 57dB inserted into the Ionospheric clutter region. 68

4.17 Results of using the D^3, Spatial Adaptive Doppler filter, and Nonadaptive MF algorithms to detect an ideal target with amplitude 55dB inserted into the Ionospheric clutter region. 70

4.18 Results of using the D^3, Spatial Adaptive Doppler filter, and Nonadaptive MF algorithms to detect a real target spread over 7 range cells and with amplitude 55dB inserted into the Ionospheric clutter region. 71

4.19 Results of using the Hybrid,D^3,JDL, Spatial Adaptive Doppler filter, and Nonadaptive MF algorithms to detect an ideal target with amplitude 55dB inserted into the Ionospheric clutter region. 72

4.20 Results of using the Hybrid,D^3,JDL, Spatial Adaptive Doppler filter, and Nonadaptive MF algorithms to detect a real target spread over 7 range cells and with amplitude 55dB inserted into the Ionospheric clutter region. 73

4.21 Results of using the RSC-PAMF, TASC-PAMF, Adaptive Doppler filter, and Nonadaptive MF algorithms to detect an ideal point target with amplitude 59dB inserted into the Ionospheric clutter region. 74

4.22 Results of using the RSC-PAMF, TASC-PAMF, Adaptive Doppler filter, and Nonadaptive MF algorithms to detect a real target spread over 7 range cells and with amplitude 63dB inserted into the Ionospheric clutter region. 75

4.23 A tree-like representation of the FFA method for a datacube with $M = 12$ pulses, $N = 12$ elements, spatial-partitioning-sequence=[2 2 1 3], and temporal-partitioning-sequence=[4 1 3 1]. 80

4.24 ΔMSMI versus target amplitude for JDL, and FFA algorithms 85

4.25 MSMI vs Range plots for using the Nonadaptive, JDL, and FFA methods to detect an ideal target in Ionospheric clutter region. All 4096 pulses are used in this simulation. 86

4.26 MSMI vs Range plots for using the Nonadaptive, JDL, and FFA methods to detect an ideal target in Ionospheric clutter region. Only 128 pulses are used in this simulation. 87

4.27 MSMI vs Range plots for using the Nonadaptive, JDL, and FFA methods to detect a real target in Ionospheric clutter region. All 4096 pulses are used in this simulation. 88

4.28 MSMI vs Range plots for using the Nonadaptive, JDL, and FFA methods to detect a real target in Ionospheric clutter region. Only 128 pulses are used in this simulation. 89

4.29 A representation of the Interleaved-FFA method. 90

4.30 Probability of detection versus SNR for a PFA=0.1, using JDL, regular FFA, and interleaved FFA methods. 95

4.31 MSMI versus range plot for interleaved-FFA method using 4096 pulses in an ideal target scenario 96

4.32 MSMI versus range plot for interleaved-FFA method using 4096 pulses in a real target scenario 96

4.33 MSMI versus range plot for interleaved-FFA method using 128 pulses in an ideal target scenario 97

4.34 MSMI versus range plot for interleaved-FFA method using 128 pulses in a real target scenario . . . 97
4.35 ΔMSMI versus target amplitude for JDL, FFA, and interleaved-FFA algorithms . . 98

Chapter 1

Introduction

The overall goal of this project is to develop a knowledge based space-time adaptive processing (KB-STAP) approach to deal with the non-homogeneous interference in high frequency surface wave radar (HFSWR). Performance of target detection algorithms, especially non-adaptive techniques, in HFSWR are primarily limited by sea clutter (at the near ranges) and ionospheric clutter (at the far ranges). In this regard, STAP appears to be a promising approach to deal with such interference. However, traditional STAP algorithms fundamentally assume the interference to be spatially homogeneous, i.e., that the statistics of the interference are consistent as a function of range. STAP algorithms, initially developed in the context of airborne surveillance radar, exploit this homogeneity to estimate interference statistics for clutter suppression. Specifically these statistics are estimated by averaging over the homogeneous range cells. Sea and ionospheric clutter, on the other hand, are well known to be highly non-homogeneous, requiring the development of alternative STAP approaches. However, our previous work [3, 4] suggested that the fundamental limiting factor in the available ionospheric clutter data sets is the lack of secondary range cells to estimate the interference covariance matrix.

In the field of STAP for airborne radar, a significant development is a knowledge based approach wherein information extracted in real time [5, 6] is exploited to determine the choice of adaptive algorithm, the parameters of the algorithm and the choice of range cells in the estimation process. The fundamental motivation in KB-STAP is the clutter non-homogeneity in airborne radar. In this regard, one key building block to this KB=STAP approach is the hybrid algorithm of [7] which combines the benefits of direct data domain (D^3) and statistical processing. By tailoring the algorithm, and its parameters, to the interference within a specific range cell, KB-STAP has the potential for making a greater impact on target detection in HFSWR. Fundamentally, ”the objective of this project is to formulate and evaluate practical KB-STAP algorithms for detection of surface vessels in strong ionospheric clutter by the Canadian East Coast HFSWRs”, a phrase extracted from the contract. As we will see, the issue clutter non-homogeneity was addressed by the development of a new adaptive algorithm tailored to fit the special characteristics of the HFSWR dataset.

This project, as is this report, was broadly divided into three phases: a literature survey and familiarization phase, a modeling and analysis phase and, finally, a formulation and testing phase. The first phase, which was documented in a report submitted in late-March 2007, presented a survey of the available literature in the area of modeling and adaptive processing of ionospheric clutter [8]. That report also presented results of some preliminary implementations of space-time adaptive processing without any regard to clutter non-homogeneities. Given the limited training samples available, the implementation was based on a factored approach, using a non-adaptive estimate in the Doppler dimension and restricting adaptive processing to the spatial dimension only.

In the second stage we began the formulation of a data model of ionospheric clutter. The model then focused on the work of Fabrizio [1] which presents a preliminary data model for ionospheric clutter observed via a over-the-horizon radar system. Unfortunately, the data provided by the Defense Research and Development Canada (DRDC) does not follow the model of [1]. In our June 2007 report [3] we showed that when applying the data model, the parameters that arise are physically impossible.

These progress reports [3,4] also detailed our preliminary efforts in applying space-time adaptive processing (STAP), including the hybrid approach to the data sets provided by DRDC. The results showed the significant gains possible in using STAP when detecting weak targets; targets that could not be detected using non-adaptive processing stand out by as much as 10-15dB when using adaptive processing. A crucial issue identified in previous work is the issue of sample support. All the data sets provided by DRDC can be divided into three segments: one dominated by the Bragg lines, one by homogeneous clutter and one dominated by ionospheric clutter. Since only data that is representative of the interference can be used to estimate the interference covariance matrix, the progress report in June 2007 focused heavily on the joint domain localized (JDL) processing algorithm [9, 10]. The report in September 2007 [4] presented the use of the hybrid algorithm.

The December 2007 progress report [11] detailed the development of a data model based on the work of [2]. This model developed by Dr. Ravan, in conjunction with significant input from Dr. Ryan Riddolls of DRDC, is able to match the characteristics of the *measured* data. This December report also presented a *new* adaptive processing algorithm that is able to exploit the entire space-time data set with limited training. The algorithm is based on the FFT, was dubbed the Fast Fully Adaptive (FFA) approach. We emphasize that these two aspects of the December report are the two key contributions of this effort. In this final report we describe testing and generalization of the FFA algorithm, material not described in any report earlier.

This final report compiles the information contained in our previous progress reports and details the final testing phase of the project. In some places therefore, there is some repetition of information, though this has been kept to a minimum to facilitate understanding of the material in each chapter. The report is organized as follows: Chapter 2 reviews the preliminary work undertaken in this effort. This chapter covers a literature review of relevant work and the results of some preliminary adaptive and non-adaptive data analysis for the measured HFSWR dataset. Chapter 3 presents one of the core contributions of this effort - a data model to *simulate* ionospheric data. Chapter 4 presents results of all the space-time adaptive processing schemes developed and implemented in this chapter. Of special importance are Sections 4.6 and 4.7 that present the new adaptive algorithm developed under this effort. These schemes are shown to provide huge improvements over any of the other STAP algorithms implemented. The report concludes with several remarks on the overall effort in Chapter 5.

Chapter 2

Preliminaries: Literature Review and Data Analysis

This chapter deals with the first phase in the project: the literature survey and familiarization phase. This chapter covers the specific tasks:

- Literature survey of the available public domain work on data analysis for HFSWR.
- Literature survey of STAP algorithms as applied to HFSWR.
- Preliminary data analysis of the HFSWR data set provided by the Defense Research and Development Canada (DRDC) Technical Authority, Dr. Ryan Riddolls.
- Identification of source of information for anticipated application of KB-STAP.

The goal of the first phase was largely, therefore, for the researchers to familiarize themselves with the available literature and to set the stage for following two phases.

This chapter is organized as follows: Section 2.1 provides an overview of the available literature in data gathering and modelling of HFSWR data, especially ionospheric clutter. Section 2.2 presents a similar review of data analysis and adaptive processing as applied to HFSWR. Section 2.3 presents the results of our preliminary non-adaptive data analysis of the data set provided by Dr. Riddolls. Section 2.4 presents the methodology and results of the preliminary adaptive processing work. Section 2.5 focuses on our suggestions in how to apply KB-STAP to HFSWR.

2.1 Literature Review of Data Analysis as Applied to HFSWR

In mitigating the deleterious effects of ionosphere clutter in target detection with the incorporation of HFSWR there is no consensus amongst researchers on the optimal approach. There is a variety of factors that can influence the efficacy of the algorithms and their applicability depends on the particulars of the ionosphere prevailing in a certain location. The non-stationarity and non-homogeneity properties that characterize the ionosphere provide additional intellectual challenges in contriving reliable, ubiquitously applicable mathematical models. The synergy of selection of validated models tailored to the peculiarities of a particular location, space-time processing modalities to extract the information of interest and effective decision making paradigms is imperative in addressing the issue.

There exist a few groups of researchers with the needed experimental facilities that appear to have dominated the area of signal processing for ionospheric clutter. These groups have been identified, the latest propensities have been examined and segments of their produced work is included in an attempt to incorporate the most relevant and recent accomplishments. The time limitations conduced to the deficiency of presenting the findings in a systematic and pragmatic manner. A synopsis of various papers is presented highlighting limitations and strengths.

In [12] the authors deal with phase contamination due to ionospheric clutter. The specific problem is that the Doppler spread mechanism renders the sea clutter spectrum distorted and resolution of coherent integration technique is degraded tremendously. In surface surveillance and remote sensing, temporal nonlinear phase path variations often produce significant spread of the ionospheric propagated signals so that the Bragg lines and the target echoes smear cross the Doppler frequency domain masking slow moving surface surface vessels. The phase contamination is attributed to complex geophysical mechanisms. The authors approach is based on estimating the instantaneous frequency, modelling the phase contamination by a polynomial phase. They make significant improvement in spectrum quality.

In [13] the same set of authors deal with double ionosphere transit. Bourdillon [14] suggested correcting the phase of the signal from a perturbation estimated using maximum entropy spectral analysis (MESA) as an estimator for the quasi-instantaneous frequency of the Bragg lines with time. It is likely to fail for the contamination with periods shorter than a few tens of a second integration time that is used in the autoregressive spectral estimation process. Perent and Bourdillon [15] proposed a simpler technique using time derivative of the signal phase as the estimation of the instantaneous frequency of the contamination with short periods. This method has introduced initially the concept of multiple operating frequencies but it is not suitable for regular FMCW radar due to its complexity.

Abramovich, Anderson and Soloman [16] addressed another method based on eigenvalue decomposition. It is an advanced version of noise subspace technique applied to the instantaneous frequency estimation. However, since the correlation between the adjacent range, azimuth, and frequency bins of the echo signal is unknown and varying, the autocorrelation matrix estimated from the available data set may be biased or rank-deficient. Thus the eigen-decomposition technique under these conditions is defective or even ineffective. An improved scheme is presented to compensate nonlinear phase path contamination, when the backscattered signal propagates through the ionosphere in high-frequency sky-wave radar systems, though not the surface wave radar system we consider in this project.

2.1.1 Data Modeling

The central aim of this project is the development *and testing* of STAP algorithms for HFSWR. It is therefore essential to have available both measured data, but also *simulated data* to develop and test algorithms in a controlled environment.

In terms of data modeling, in [17], the authors simulate ionospheric scintillation. The ionospheric plasma may be treated as an electron density with variation on both in space and time. Two general types of effects are produced at radar; the measurement of range is affected because of deviations of the speed of light in the refractive medium with direct ramification on radar's tracking function. It is the large-scale structure of the electron density that governs the range effects. The second effect is scintillation that occurs because of the existence of interfering optical paths between the target and the radar. Scintillation is produced by electron density structures on the size scale of the radar wavelength, and therefore tends to vary rapidly due to small motions of the radar-target path or changes in the medium. For key radar functions like object classification, scintillation is the effect which causes performance degradation. However, this may not play as significant a role in target detection.

From our literature survey, there appear to be two different approaches to modeling ionospheric and sea clutter. Our initial analysis suggested that one important and useful model has been developed by Fabrizio in his Ph.D. thesis [1]. He verifies the accuracy of space-time wave interference models and uses this theory to develop a space-time model of ionospheric clutter returns and also provides a parameter estimation technique to fit measured data into the model. This model is valid for a coherent pulse interval (CPI) shorter than a few seconds. For longer CPIs, he develops a stationary statistical model focusing on the prediction of second order statistics. The ionospheric reflections are treated as a random variable (unlike the wave interference model initially developed). He proposes hypothesis tests to accept or reject the validity of the model given measured data.

One should emphasize that the experimental data used by Fabrizio is taken from Jindalee radar run, apparently, by the Defense Science and Technology Organization (DSTO) in Australia. There was no guarantee that this model will be applicable to the Cape Race HFSWR. Furthermore, as indicated by Dr. Riddolls, the model used by Fabrizio is rather simplistic, dependent on a Gaussian assumption which is not valid in practice. The more commonly accepted distribution is based on fourth-order power law, making the power distribution fall off much slower than the Gaussian. We attemptted to modify Fabrizio's model to make it more realistic, but our efforts were unsuccessful.

An alternative approach also from DSTO is that of Coleman [18, 19]. This model was recently extended by Dr. Riddolls [20, 21] to simultaneously account for group delay, direction of arrival, location and Doppler. The author uses a ray tracing model and treats irregularities as perturbations of a "quiescent" path solution without irregularities. At first glance this model seems considerably more complicated than that of Fabrizio. However, we will attempt to implement both schemes and compare their fidelity given data sets from DRDC.

A comprehensive analysis of ionospheric clutter is by Chan [22] which can be used for model testing. This work also contributed to a detailed report by Sevgi *et al.* [23, 24] where a stochastic model package called *HFSIM* [25] is discussed. This package is also based on a Gaussian assumption. Another stochastic model is that of [26].

In summary, there are a few competing approaches to modelling ionospheric clutter. Our goal is to implement an accurate, if more complex data model. In this effort, the model of Fabrizio was investigated in some detail and the model of Riddolls was finaly implemented.

2.2 Literature Review of Adaptive Processing as Applied to HF-SWR

This section reviews some of the work in adaptive processing for HFSWR. While several of the papers were suggested to us by the DRDC Technical Authority, there are others works reviewed below, including some recent work of Fabrizio and Farina. Largely the work appears to have focused on reducing the degrees of freedom in the processing scheme to reduce computation load and requirements of statistically stationary sample support.

Some of the early works by researchers at DRDC include [27, 28] which discuss the use of horizontal dipoles as auxiliary antennas, as sidelobe cancellers, to suppress skywave interference.

The author finds the adaptive weights to optimally suppress interference. A reference signal is added; we believe to obtain the weights using a Weiner solution. In [29] the author extends this to a comparison of the use of horizontal and vertical dipoles for interference suppression. The author suggests use of horizontal polarization to cancel interference close to the target location (whose signal is vertically polarized). This work may not have significant impact on the present project since the measured data provided all uses the same (vertical) polarization.

Other efforts within DRDC, made available by Dr. Riddolls, include the coherent side canceller work of [30] where the authors investigate the optimal ordering of Doppler processing, beamforming and interference cancellation. One unfortunate, but not surprising result is that the optimal ordering is interference dependent (and hence time dependent) since in HFSWR the interference sources are highly time variant. A similar result was demonstrated in the context of airborne radar in [9]. In [30] specifically, the sidelobe canceller is shown effective against a single spatially confined source. An interesting, and sobering, presentation in this paper is the demonstration of the wide spatial and temporal variation in the ionospheric clutter characteristics.

These works would, we believe, be considered "classical" in the space-time adaptive processing community. They underline the complexity of the problem being attempted in this project and the need for knowledge-based approaches. One should mention that our search of the DRDC database generated several reports on direction finding for HF radar systems, a body of knowledge not reviewed here. One should also mention that there is continuing work in DRDC into the physics and modeling of ionospheric clutter [20, 21], work that played an important role in the next phase of our project.

A significant fraction of the work adaptive processing for HFSWR is apparently led by Dr. Yuri Abramovich and/or Dr. Giuseppe Fabrizio at DSTO (though Fabrizio has recently started also collaborating with researchers in Italy such as Dr. Alfonso Farina). In particular, Fabrizio has several contributions developed in detail in his thesis and then several later works that are reviewed below. The work of Abramovich focuses largely on the underlying phenomenology and measurements [31].

The work of Fabrizio [1] is one focus of our proposed modelling and analysis approach. The work of the group led by Fabrizio [1, 32–36] has focused on the development of the adaptive coherence estimator (ACE) and its variant the spatial adaptive subspace detector (ASD) [32] for over-the-horizon (OTH) radar systems. In the following we largely focus on their most recent contributions [34–36] presented as an improvement on their previous work [1, 32, 33].

The ACE test, like the modified sample matrix inversion (MSMI) statistic, has the important property of constant false alarm rate (CFAR); however ACE has the CFAR property even if the data within the range cell under test has a different scale from that in the secondary data. Unfortunately, ACE is highly susceptible to target mismatch and hence the motivation for the development of the ASD detector. The ASD detector treats a single target as a signal subspace with rank greater than 1 [35]. In their latest work [36], Fabrizio *et al.* address the issue of unwanted signals *in the primary data*. They propose a generalized likelihood ratio test (GLRT) to address this issue. To address the issue of target mismatch, they model both the target and the discrete interference source within the primary range cell as low-rank sources given by a linear combination of closely spaced Doppler frequencies. The GLRT is then formed by maximizing over the parameters of both the target and discrete interference. Unfortunately, a significant drawback is that the implementation of the GLRT requires exact knowledge of the parameters of the interference. This necessitates a two-pass approach wherein the the detector acquires some knowledge of the existence of the interference and its parameters in real time.

This two-pass approach is reminiscent of the two-pass approach proposed by Adve *et al.* in [5,6]. We will revisit this issue later in this document in Section 2.5. It should be noted that other than the experimental results, the formulation in [36] does not specifically target HFSWR.

The work in [36] focuses on adaptive Doppler processing exclusively. Previously the authors developed a space-time adaptive processing algorithm [34] for OTH radar using beamspace-range processing. This paper is of interest because the authors claim that with N spatial elements and M time taps, they can reduce the dimension of the STAP filter to $M + N$ as opposed to the usual MN. The move to beamspace is as in the joint domain localized processing scheme of [10] in that the spacing between beams is not restricted the use of a FFT. Interestingly, the authors use *fast time* samples to form the Doppler steering vector, *not the traditional slow time samples* - hence beamspace-range processing.

The other significant group of researchers working in adaptive processing for HF radar is in China. In [37] the authors propose a scheme for clutter mitigation that both varies the clutter weights to counter non-stationary ionospheric clutter within a coherent processing interval (CPI) while maintaining some stability in the gain on target. Two issues with this paper appear to be the need for partitioning the overall CPI in to sub-CPIs, increasing the computation load and the somewhat ad-hoc nature of the proposed processing scheme with transitions from sub-CPI to sub-CPI.

The paper [38] is the basis for experimental work reported in [39]. In [38] the authors claim that clutter and target only impacts on positive frequencies, not on negative frequencies. The basis for this is not clear and will be investigated as we move forward in this project.

In [40] the authors present a multiple matched filtering scheme to deal with clutter multipath specifically. Here the authors use the linear FM rate to distinguish the multiple paths and the center frequency to distinguish reflections from multiple layers. In this regard, this paper does not appear to be directly related to our work.

In [41] a ionospheric phase decontamination scheme using the singular value decomposition of a Hankel matrix created out the received signal is proposed. This decontamination is then combined with suppression of sea clutter by removing the eigenvalues associated with the narrowband Bragg lines. There is no adaptive processing in the sense proposed here in this project.

Beyond the groups reviewed above, a few other papers are available in the literature. For OTH systems, the authors of [42] propose to distinguish between sea clutter and the target using a coherence function. Again, no adaptive processing of the type proposed here is performed. In [43] the authors extend temporal only processing to the use of STAP. However, the approach used is the classic STAP approach of estimating the covariance using secondary data without any specific attention paid to homogeneity.

2.3 Preliminary Data Analysis

This section details the non-adaptive data processing conducted on the data set provided by the DRDC Technical Authority, Dr. Ryan Riddolls; the data set is `hfswr_data_25mar2002_030257.mat`. The data comprises $N = 16$ channels, $M = 4096$ pulses, and $K = 270$ range cells. The radar operating frequency was 3.1MHz corresponding to a wavenumber of $k = 0.065$rad/m. The first range cell corresponds to 62.75km with each range cell covering 1.5km. The 4096 pulses use a pulse repetition frequency (PRF) of 15.625Hz, setting the maximum resolvable Doppler frequency to ± 7.8125Hz.

The inter-element distance of the uniform linear array is $d = 33.33m$ (corresponding to 0.344λ).

The data analysis conducted in this phase of the project focused on non-adaptive processing. Some sample results are provided illustrating the interference distribution as a function of angle, Doppler and range.

2.3.1 Element-Range Plots

The first set of results focus on the range dependence of the interference.

Figure 2.1 plots the power distribution, in dB, of the first pulse as a function of element and range. There appear to be three distinct segments in range - a near range segment up to approximately range cell 50 with significant interference power, a segment between range cell 50 and 180 with lower power and, finally, the range cells dominated by ionospheric clutter past range cell 180. The angle-Doppler plots associated with these range cells show an interesting variation in the angle-Doppler structure of the interference in these range segments. Figure 2.2, focusing on pulse number 2000, provides another plot to confirm this impression.

The figures also point to a problem with element 13, an issue pointed out by Dr. Riddolls. This element appears to be attenuated by as much as 40dB. However, interestingly, focusing on this one element suggests that this receiver is not totally "dead". The associated angle-Doppler plot in Fig. 2.5 presented later has the appropriate characteristics, only attenuated by as much as 40dB.

2.3.2 Range-Doppler Plots

This section focuses on range-Doppler plots for individual elements. In a large part these plots were created using a snippet of MATLAB® code received from Dr. Riddolls. The only change made was in the labelling of the axis in terms of Doppler frequency and distance as opposed to Doppler/range bin. Figures 2.3 and 2.4 plot the power distribution of the radar signal returns as a function of range and Doppler. As is clearly seen, there are three distinct clutter regions; the near region extending to approximately 200km (comprising approximately the first 50 range bins) dominated by the Bragg lines and sea clutter, a region at the far ranges beyond 350km dominated by the ionospheric clutter and, interestingly, a middle region of sea clutter with less structure. This corroborates with our initial impression from Figs. 2.1 and 2.2. As we will see in later plots, this variation in clutter structure is also visible in the angle-Doppler plots presented in Section 2.3.3 and may have significant implications for interference suppression.

In both plots the Bragg lines are clearly visible. The advancing and receding lines are at $\pm 0.18 Hz$ corresponding to the expected Doppler frequency given by

$$f_B = \sqrt{\frac{g}{\pi\lambda}}, \tag{2.1}$$

where $g = 9.81\text{m/s}^2$ is the acceleration due to gravity and λ is the wavelength corresponding to the operating frequency of 3.1MHz.

The color bar on Figs. 2.3 and 2.4 corresponding to element 1 and element 8 also show a slight taper between the edge element (1) and the center element (8). This was reported to us by Dr. Riddolls. Finally, another interesting plot is Fig. 2.5 with the range-Doppler power distribution for element 13. While our initial understanding was that this channel was "dead", in fact it appears to be receiving data, but attenuated by as much as 40dB with respect to the other elements. At

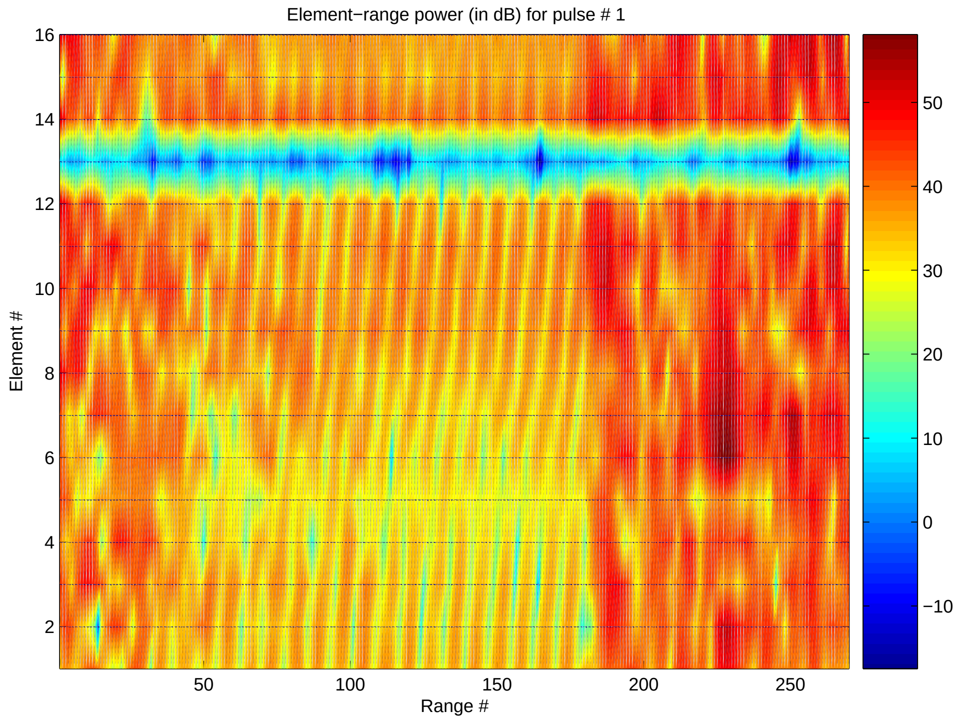

Figure 2.1: Element-range power distribution for pulse number 1

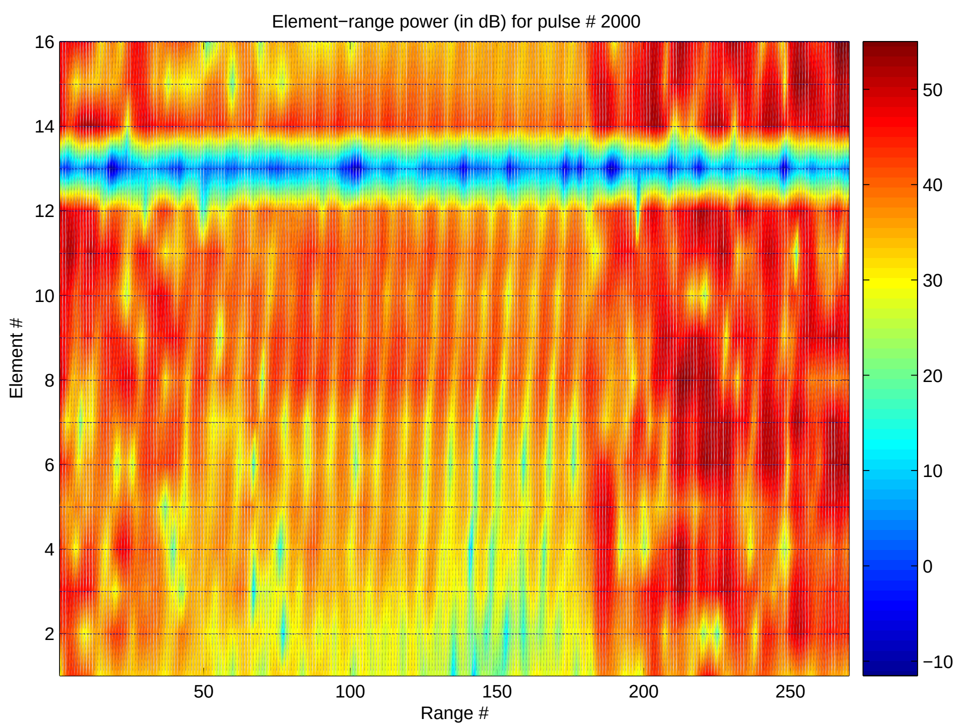

Figure 2.2: Element-range power distribution for pulse number 2000

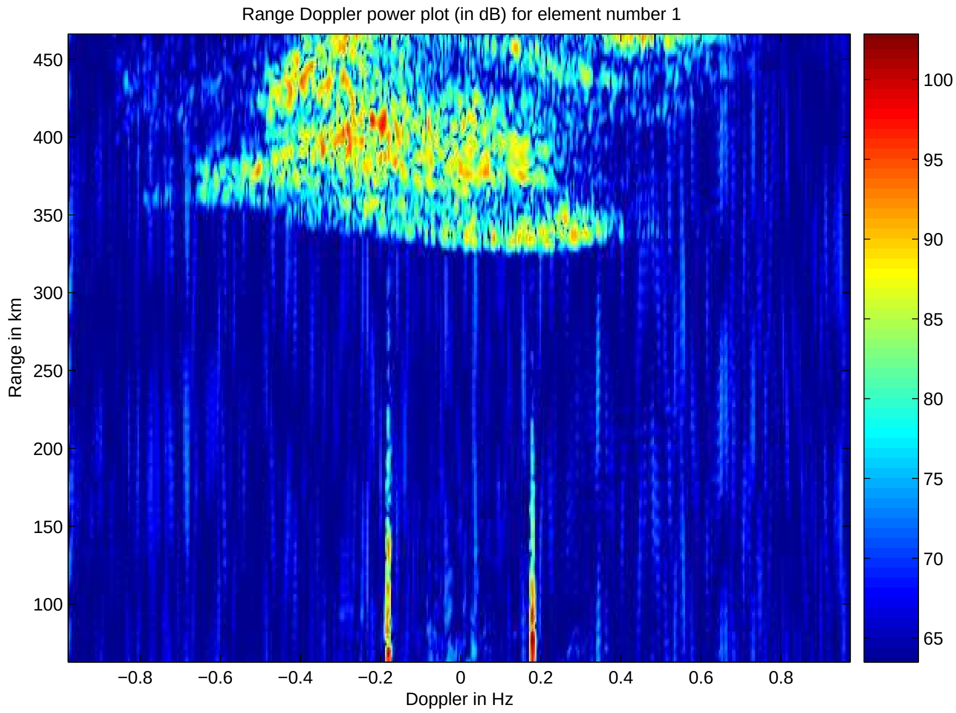

Figure 2.3: Range-Doppler power distribution for element number 1

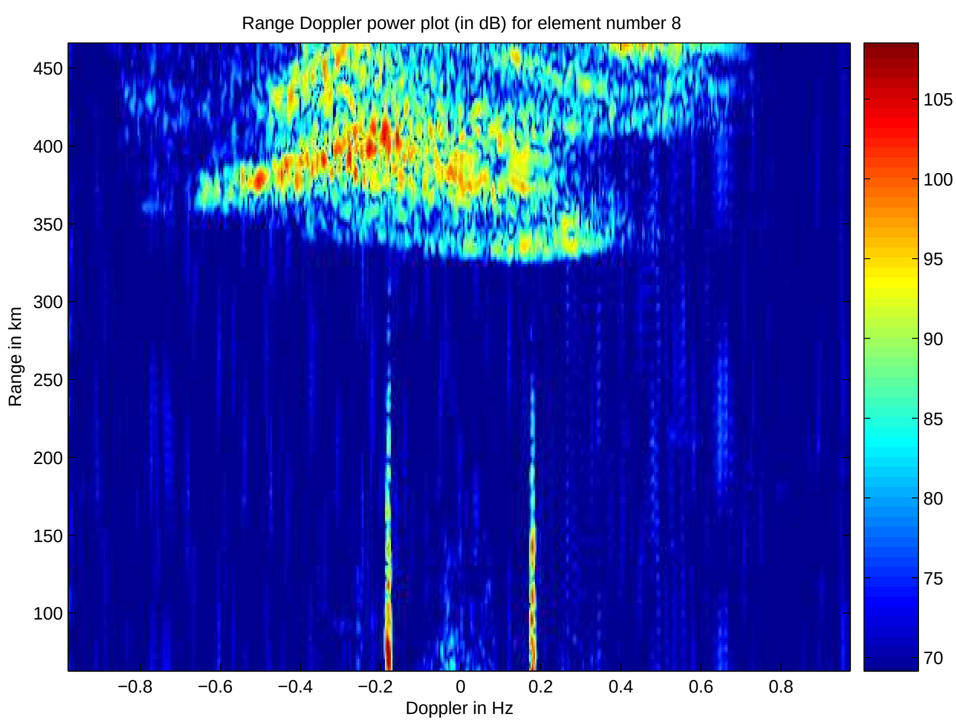

Figure 2.4: Range-Doppler power distribution for element number 8

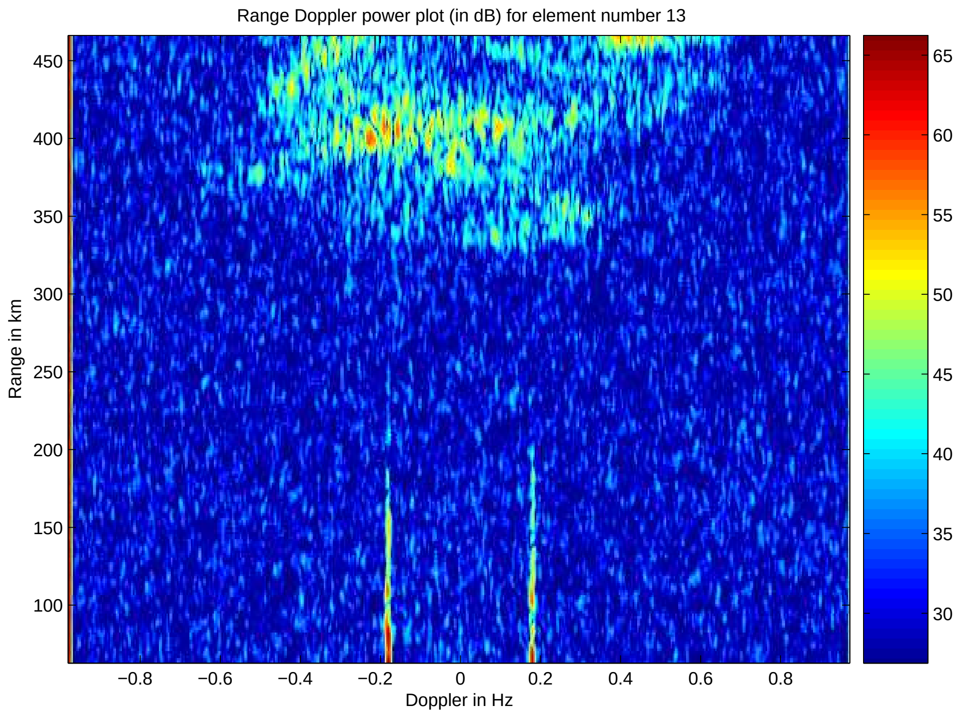

Figure 2.5: Range-Doppler power distribution for element number 13

the present time, for purposes of the adaptive processing scheme given below, we have eliminated this channel from the data. While it is not clear how to use channel 13, we may wish to retain this flexibility in the future.

The range-Doppler plots provide crucial information for the STAP process. A fundamental limitation of STAP is the need for training data to estimate the statistics of the interference with a primary range cell. This training data, clearly, must be statistically homogeneous with respect to the range cell under test. The range-Doppler plots indicate that there is limited training available within each clutter region. This is independent of whether the clutter homogeneous within each of the three clutter regions described above.

2.3.3 Angle Doppler Plots

The final set of non-adaptive processing of the data provided by DRDC are angle-Doppler plots for individual range cells. These plots are useful since they illustrate the power distribution in angle-Doppler space, the two Fourier spaces corresponding to the spatial and temporal domains in which STAP will be implemented. It is well accepted that it is easier to suppress localized interference (localized near a specific Doppler/angle). We will see that the range cells dominated by the Bragg lines and those dominated by the ionospheric clutter appear to have a more coherent structure.

Figures 2.6 and 2.7 plot the angle-Doppler structure for range bins 1 and 50 respectively (ranges of 62.75km and 136.25km respectively). As is clear from Fig. 2.6 the interference in the first range bin has a clear structure - the Bragg lines near zero Doppler are visible across all angles. Also, the interference is localized to a few angles including a relatively strong source at approximately 35^o

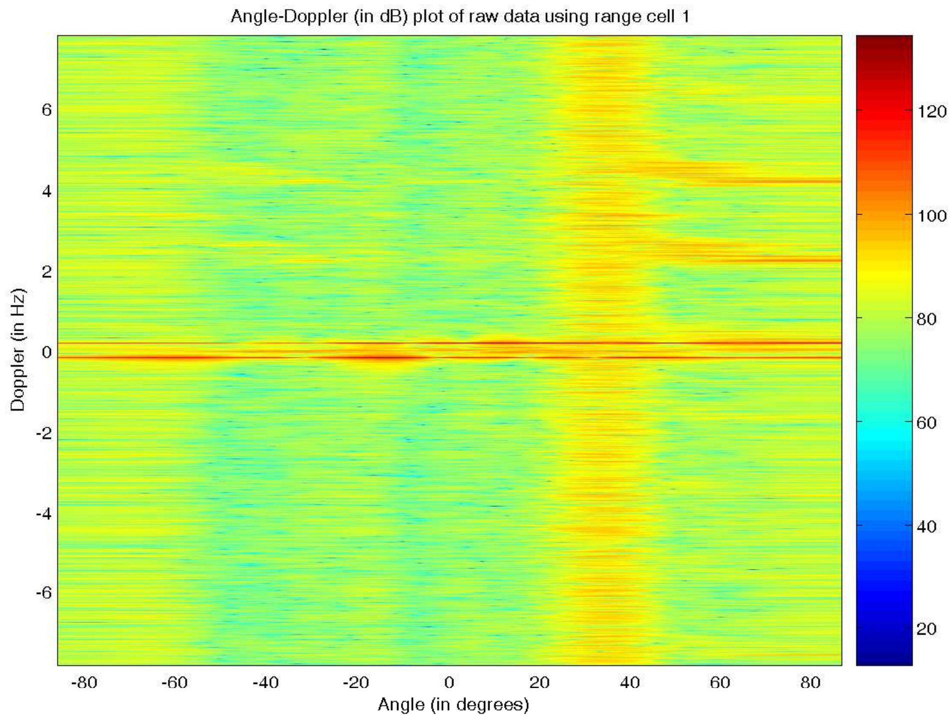

Figure 2.6: Angle-Doppler power distribution for range bin 1

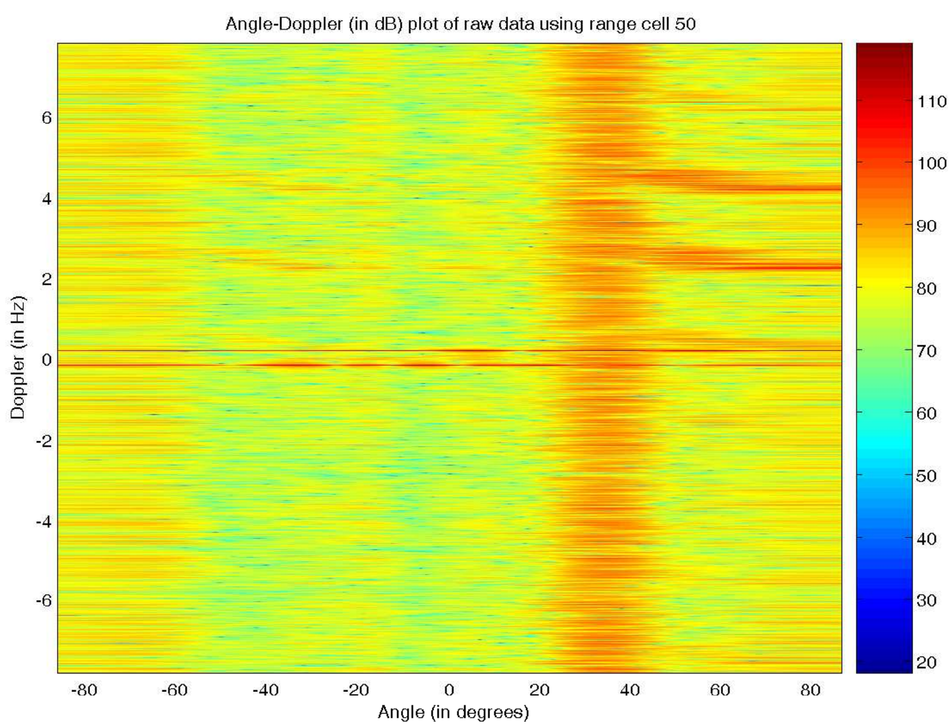

Figure 2.7: Angle-Doppler power distribution for range bin 50

(relative to broadside). As well see, this interference source appears in all range cells [1]. In addition to the Bragg lines, there appear to be two strong sources of interference near end-fire with Doppler frequency of approximately 4Hz. We have not, as of now, identified this source.

Figure 2.7 plots the power distribution in angle and Doppler for range cell 50, at the edge of the first interference region. Comparing this plot to Fig. 2.6 one can see visualize the loss of structure in the interference. The interference here is far more spread out. This effect is further illustrated in Figs. 2.8 and 2.9 corresponding to range bins 100 and 150. In these two figures the lack of structure in the clutter is particularly striking. This has significant implications for the STAP process; with its focus on a localized region in angle-Doppler space, an algorithm such as the joint domain localized (JDL) processing scheme [9, 10] may be useful here.

In the range cells dominated by ionospheric clutter, a structure is again visible in angle-Doppler space. Figures 2.10 and 2.11 illustrates the strong ionospheric interference close to zero-Doppler and the external interference is again clearly visible.

In summary, the angle-Doppler plots suggest both the potential of STAP to suppress interference and also some cautionary tales. As seen before, the data cube appears to have three distinct regions. In the first region, dominated by the Bragg lines, a clear structure is visible and a "traditional" adaptive algorithm such as the sidelobe canceller followed/preceded by Doppler processing may be adequate. In the third region, dominated by ionospheric clutter, KB-STAP is required due to the inherent non-stationarity of the clutter. In the middle region, again dominated by sea clutter, no structure is visible and a JDL-based algorithm would be required. One should mention that JDL may be a good candidate for within the first region as well given the very large number of pulses within a CPI. JDL would allow for true space-time adaptive processing as opposed to Doppler processing followed by/preceded by a sidelobe canceller.

2.4 Adaptive Processing

We present here the results of initial attempts at space-time adaptive processing using the data set provided by Dr. Riddolls. Given the division of the range cells into three regions available, we injected a simulated target into either the Bragg dominated or ionospheric clutter dominated regions. The target amplitude was chosen such that it was not visible using non-adaptive processing (matched filtering as used in the figures presented above).

2.4.1 Data and Processing Model

The target model chosen is the simplest one as suggested by Ward [44]. In a specific range bin, the target range bin, the temporal-spatial data is modified by adding a *point* target:

$$\mathbf{x} = \xi \mathbf{v}(\phi_t, f_t) + \mathbf{c} + \mathbf{n}, \tag{2.2}$$

where $\mathbf{c} + \mathbf{n}$ represent the clutter and noise given within the the data cube and ξ represents the chosen target amplitude. The vector $\mathbf{v}(\phi_t, f_t)$ represents the space-time steering vector of the target

[1] Our discussion with Dr. Riddolls suggests this is external interference.

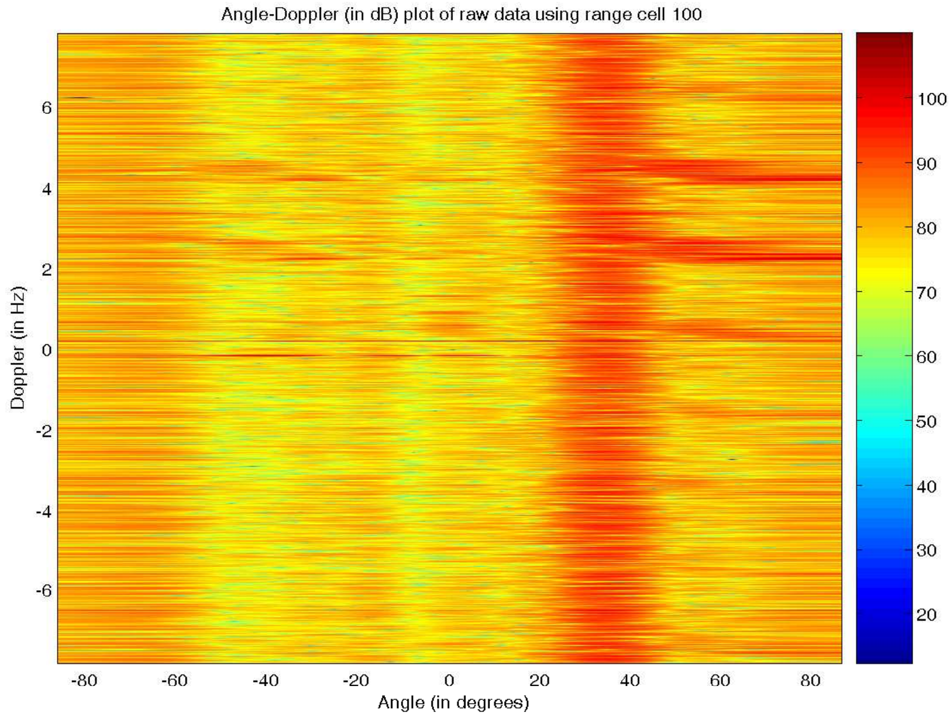

Figure 2.8: Angle-Doppler power distribution for range bin 100

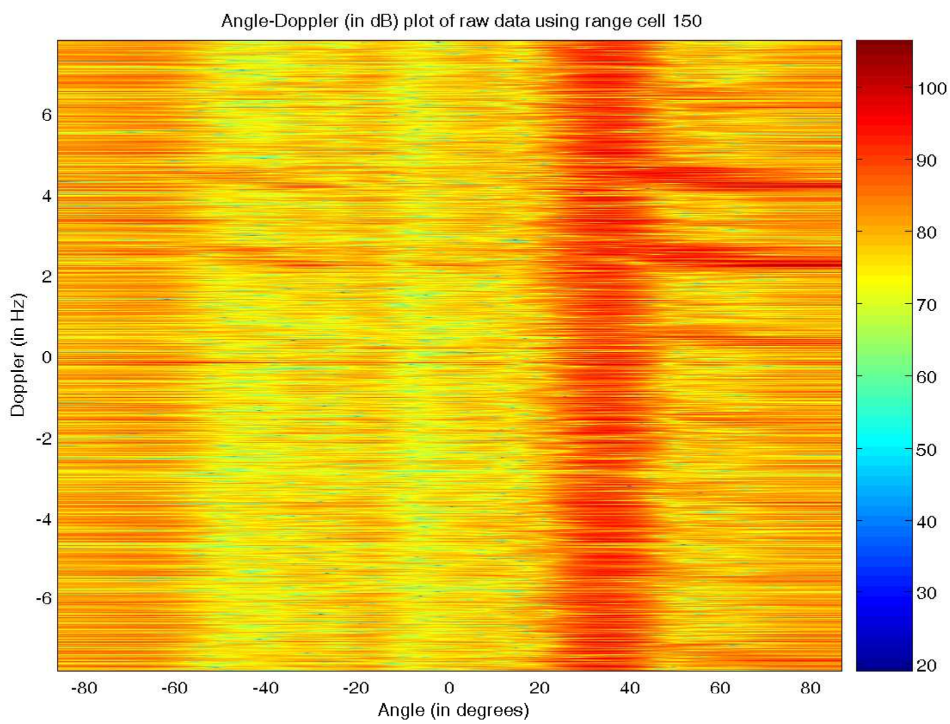

Figure 2.9: Angle-Doppler power distribution for range bin 150

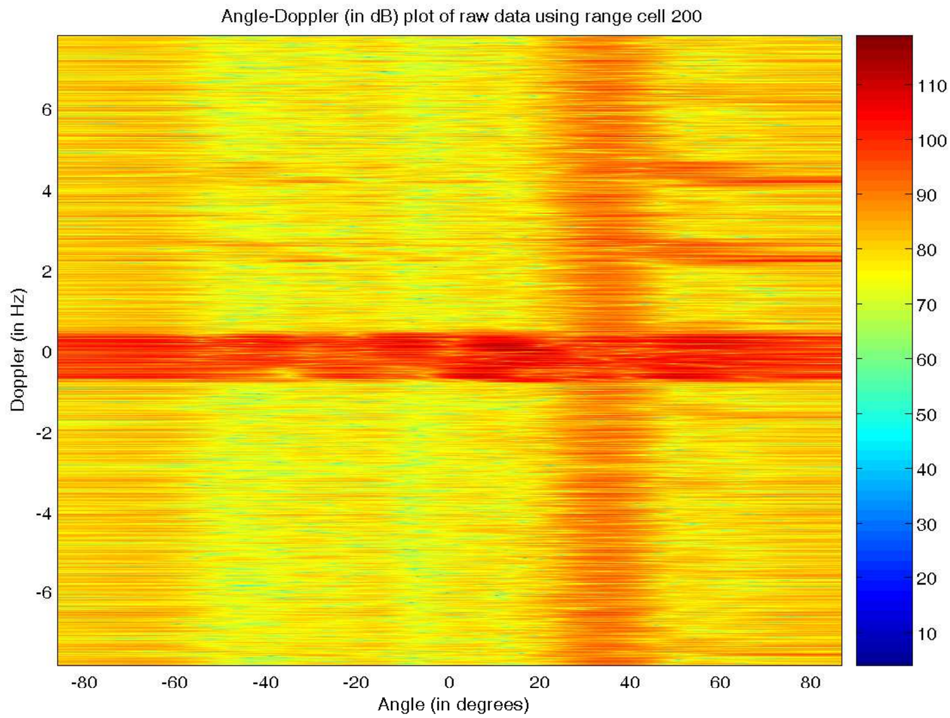

Figure 2.10: Angle-Doppler power distribution for range bin 200

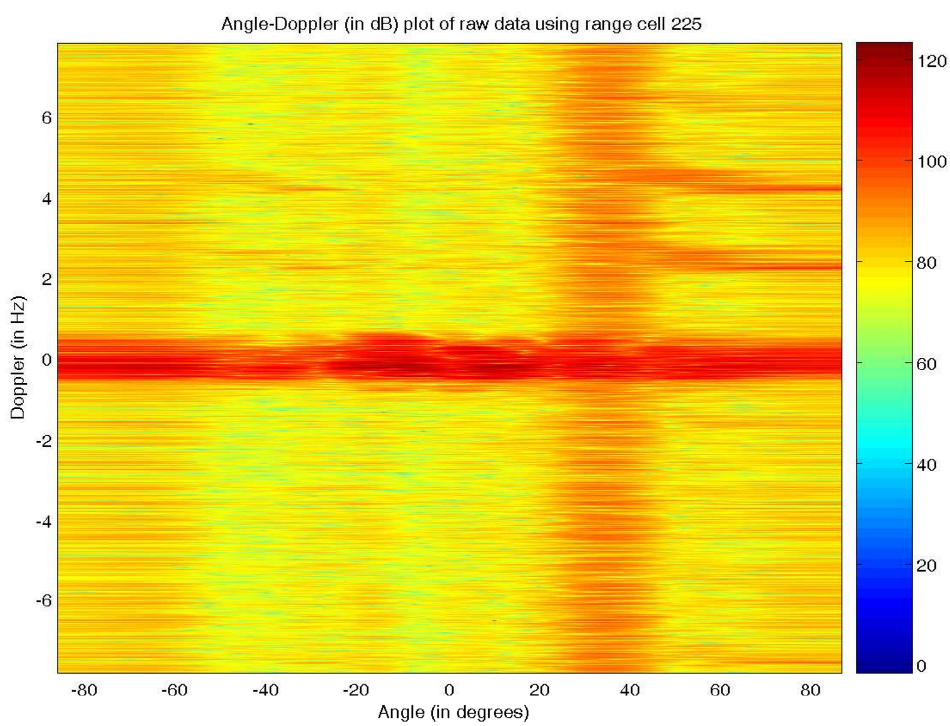

Figure 2.11: Angle-Doppler power distribution for range bin 225

corresponding to a chosen angle ϕ_t and Doppler f_t. This steering vector is given by

$$\begin{aligned}
\mathbf{v}(\phi_t, f_t) &= \mathbf{b}(f_t) \otimes \mathbf{a}(\phi_t), &(2.3)\\
\mathbf{a}(\phi_t) &= \begin{bmatrix} 1 & z_s & z_s^2 & \dots & z_s^{(N-1)} \end{bmatrix}^T, &(2.4)\\
\mathbf{b}(f_t) &= \begin{bmatrix} 1 & z_t & z_t^2 & \dots & z_t^{(M-1)} \end{bmatrix}^T, &(2.5)\\
z_s &= e^{j2\pi f_s} = e^{(j2\pi \frac{d}{\lambda} \sin \phi_t)}, &(2.6)\\
z_t &= e^{j2\pi f_t / f_R}, &(2.7)
\end{aligned}$$

where $\otimes$ represents the Kronecker product of two vectors, f_R the pulse repetition frequency (PRF), and λ the wavelength of operation. Note that this form of the spatial steering vector is valid only for a linear, equispaced array of isotropic sensors, an assumption made in this phase of the project. The fully adaptive processor determines a set of weights $\mathbf{w}$ by solving the matrix equation [45]:

$$\begin{aligned}
\hat{\mathbf{R}}\mathbf{w} &= \mathbf{v}(\phi_t, f_t), &(2.8)\\
\hat{\mathbf{R}} &= \frac{1}{K}\sum_{k=1}^{K} \mathbf{x}_k \mathbf{x}_k^H, &(2.9)
\end{aligned}$$

where $\mathbf{x}_k$ represents one of K secondary, target-free, data samples and ^{H} represents the Hermitian (conjugate transpose) of a matrix. These weights are used to obtain a decision statistic to decide whether a target is present at that range bin or not. This paper uses a constant false alarm rate (CFAR) modified sample matrix inversion (MSMI) statistic [46],

$$\rho_{\text{MSMI}} = \frac{\left|\mathbf{w}^H \mathbf{x}\right|^2}{\mathbf{w}^H \mathbf{v}}. \tag{2.10}$$

Unfortunately, the training available cannot support the fully adaptive processor. As developed in [45] the general rule of thumb is that the training samples required is approximately twice the number of unknowns in the weight vector. In the DRDC data set, we have $M = 4096$ pulses and $N = 16$ elements, i.e., the fully adaptive processor has $NM = 65536$ unknowns. Clearly it will not be possible to estimate such a large covariance matrix.

In this work, we first Doppler process the data (with a length-4096 Blackman window) concatenated with a length-N adaptive processor. In theory, the performance should be the same as the sidelobe canceller. Since $N = 16$ we use $K = 2N = 32$ range cells to estimate the interference covariance matrix. For Doppler bin m, the spatial weight vector is obtained using

$$\begin{aligned}
\mathbf{w}_m &= \hat{\mathbf{R}}_m^{-1} \mathbf{a}(\phi_t), &(2.11)\\
\hat{\mathbf{R}}_m &= \frac{1}{K}\sum_{k=1}^{K} \mathbf{x}_k(m) \mathbf{x}_k^H(m), &(2.12)
\end{aligned}$$

where $\mathbf{x}_k(m)$ is the spatial data in range bin k at Doppler bin m.

2.4.2 Simulation Results

In the set of results presented we set $\xi = 5$, chosen somewhat arbitrarily to ensure that non-adaptive processing cannot detect the target, but adaptive processing can.

Figures 2.12 and 2.13 present the results of non-adaptive and adaptive processing respectively. In this example, the target is injected in range bin number 25 with a Doppler frequency of $f_t = 0.18$ corresponding to the frequency of the Bragg line. The target is at an angle of 35^o, placing it within the external interference source. Comparing the result to Fig. 2.3 the target is within the Bragg line (the two figures look different because of a normalization applied to Fig. 2.12).

The results of adaptive processing are shown in Fig. 2.13. The target is clearly visible at the correct range/Doppler bin. This figure illustrates the potential of applying STAP in the detection of weak targets.

Figures 2.14 presents cuts of these 3D figures at the target Doppler. The target after using adaptive processing is clearly visible while non-adaptive processing does not detect the target. Similarly, Fig. 2.15 makes the same comparison when the target is in the ionospheric clutter region, at range bin 215. The target Doppler and angle remain the same. Again, the target is clearly visible while non-adaptive processing cannot find the target.

One should emphasize that these examples use a simplistic, point, target model, one that is ideal for the application of STAP. In the next phase we will develop more realistic target models.

2.5 KB-STAP

One component of the proposed work in the first phase of this project an identification of the sources of information that can be used in a knowledge based processor. While initially proposed to address the problem of data non-homogeneity, the notion of KB-STAP has evolved to encompass schemes that exploit all available sources of information to maximize separation of the target and clutter subspaces. KB-STAP tailors the choice of adaptive algorithm, the parameters of the algorithm and the choice of training data to suit the interference at hand. There are, therefore, two different aspects of the KB-STAP problem; one deals with algorithm development, the other in the decision making process to choose between algorithms and their parameters.

The practical development of KB-STAP is a long-term project with both algorithm development and fundamental research components. The ionospheric clutter component is a highly non-stationary random process with both spatial and temporal variations. To truly tailor the algorithm to the interference we need a parameter estimation process that determines the parameters of the ionospheric clutter data model. This, in turn, raises the question of a good data model which may itself have to vary from location to location and from application to application.

In the long-term therefore we envision a closed loop system wherein the received signals, possibly over multiple CPIs, are processed to determine, in real time, the parameters of the clutter model. These parameters would include information such as the sections of statistically homogeneous data available for training. In an ideal world, the parameter estimation process would also identify the parameters of the statistical distribution of the clutter as well. Unfortunately, these are all probably unsolved problems.

The goal of this project was somewhat more modest and more realistic given the time involved. We planned to develop space-time adaptive processing schemes, including the JDL scheme of [10] and especially the hybrid algorithm of [7] in the context of sea and ionospheric clutter. In point of fact, our expectations were exceeded with the development of the fast fully adaptive (FFA) algorithm as described in Section 4.6.

We plan to use the range-Doppler plots such as described above to estimate the regions wherein

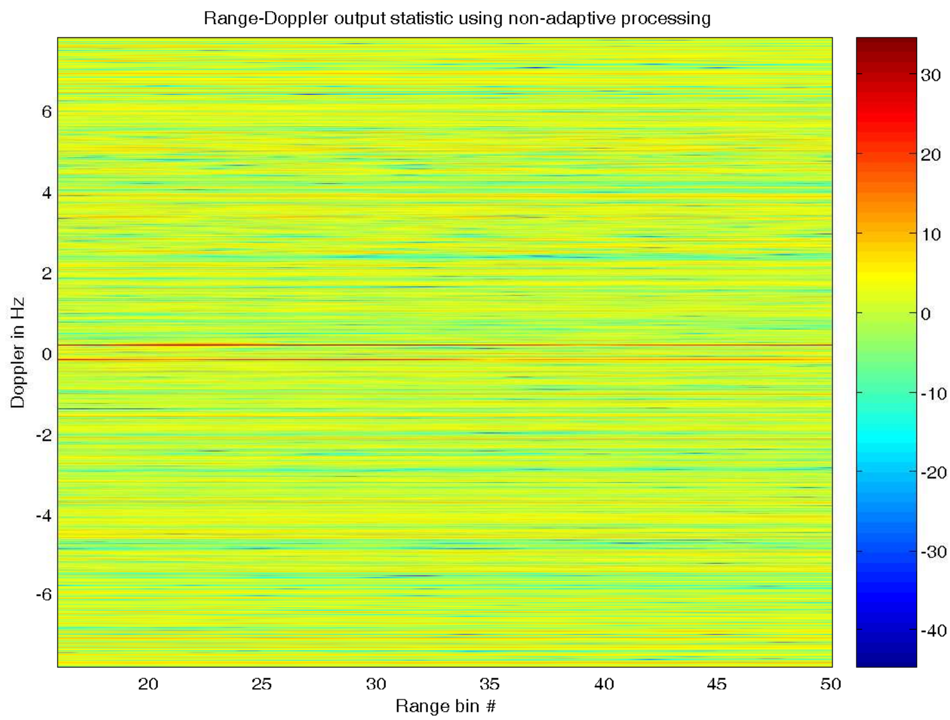

Figure 2.12: Output statistic with non-adaptive processing

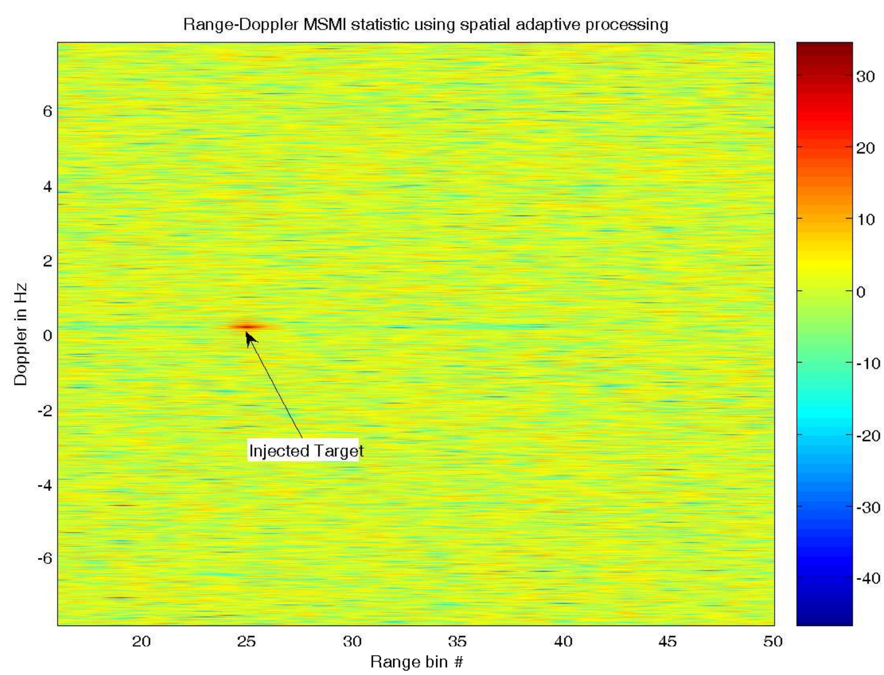

Figure 2.13: MSMI statistic as a function of range and Doppler

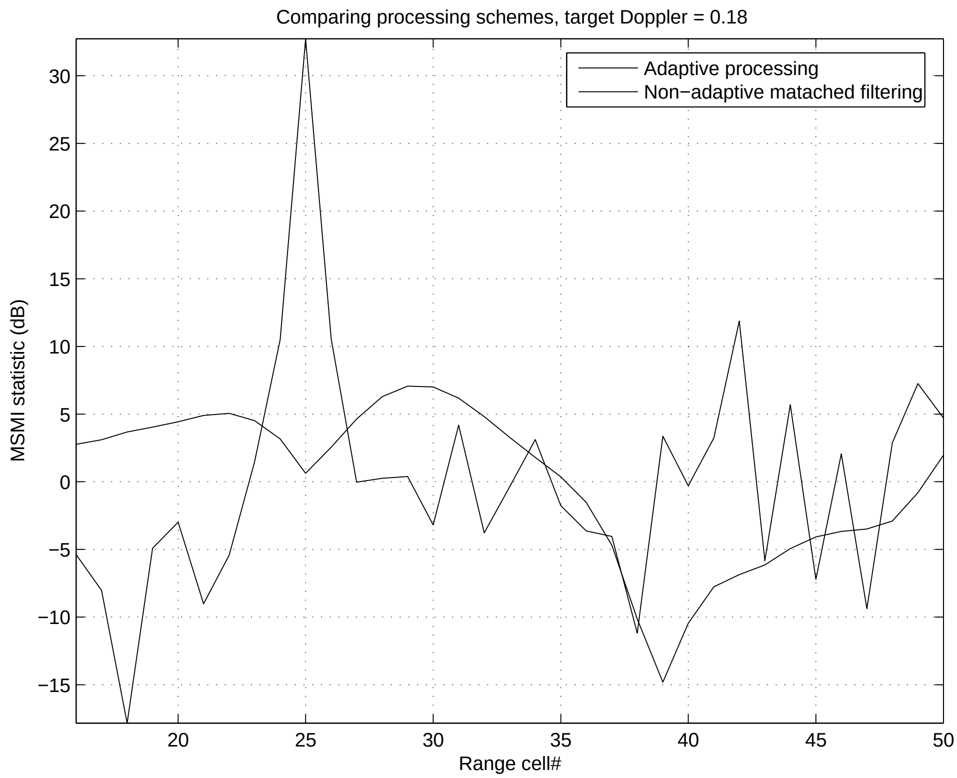

Figure 2.14: Comparing adaptive and non-adaptive processing with target within the Bragg line

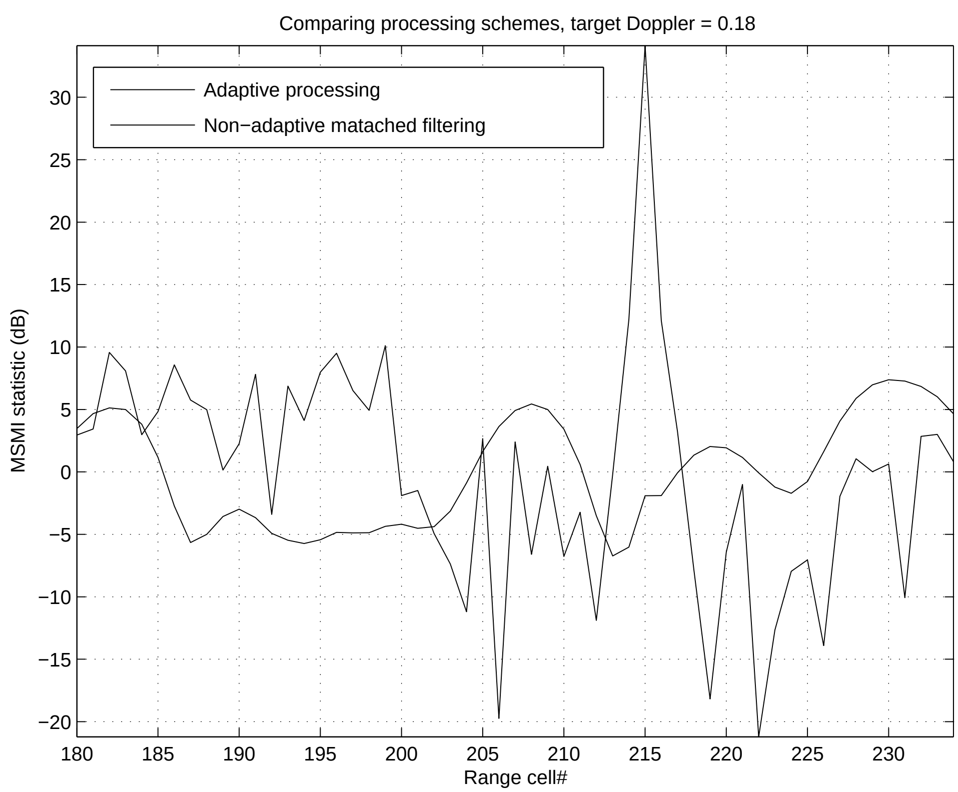

Figure 2.15: Comparing adaptive and non-adaptive processing with target within the ionospheric clutter

different algorithms will be required. Plots such as these will also determine the training available and hence the parameters of the algorithm. The hybrid algorithm is based on the JDL scheme and can be used to detect non-homogeneous range cells. There are other potential sources of knowledge - given the large number of pulses within a CPI, some pulses can be used for estimation of the interference covariance matrix.

Chapter 3

Data Models for Ionospheric Clutter

As described in the previous chapter, the algorithm development undertaken in this effort began with the measured data provided by DRDC. However, it is not possible to truly understand the workings of an algorithm using measured data alone. Both algorithm development and testing require *simulated* data so that a multitude of experiments can be performed in a controlled manner.

In a HFSWR system, interference signals are received by the array after reflection from the ionosphere which is a dynamic and spatially inhomogeneous propagation medium. Despite the vast amount of theoretical research, there are very few experimental studies which have quantitatively analysis the effect of ionospheric propagation on the interference cancellation performance of various adaptive beam-forming algorithms. Moreover it is currently unclear how more effective adaptive beam-forming algorithms should be designed and optimized for different HF interference and noise scenarios. This is partly due to the lack of experimentally verified space-time signal processing models of ionosphere reflection process which can distort the structure HF signal over time intervals equal to CPI of radar. In this project we plan to implement a useful model that has been developed by Fabrizio in his PhD thesis [1] that represents the space-time characteristics of ionospherically-propagated HF signals received by a very wide aperture antenna array. In discussions with the Dr. Riddolls it has been pointed out that the model of Fabrizio is limited and may not model ionospheric clutter accurately. However, from our literature survey, this model is the furthest developed and, therefore, represents our initial attempt at developing a data model for ionospheric clutter.

This chapter is organized as follows. Section 3.1 describes the data model and the results of implementing the data model of Fabrizio [1]. Section 3.2 presents the results of our implementation of the model of Dr. Riddolls [2]. We emphasize that the work in Section 3.2 is one of the key contributions of this project.

3.1 Data Model of Fabrizio [1]

3.1.1 Signal Processing Model

This section develops the space-time data model under consideration. In practice we will have estimate the model parameters from the data provided by DRDC. The model consists of a superposition of different propagation modes which can not be resolved in range. In the stationary statistical model each mode is represented by a distributed signal which is described by an angular and Doppler power density function. The simplest power density functions are analytically defined by a "mean" parameter which indicates the mean angle of arrival (or Doppler shift) of a mode and a "spread" parameter which indicates the level of angular spread (or Doppler spread) induced by ionosphere. We use the method in [1] which jointly estimates the mean and spread density function parameters from a mixture of space-time distributed modes.

Space time distributed HF signal model

The narrowband HF channel model which used to model ionospherically-propagated HF signals received by antenna arrays was developed in [47]. This multi-sensor model represents the composite of a N-dimensional antenna array snapshot $x_k(t)$ recorded at the k^{th} range cell in the t^{th} pulse repetition interval (PRI) and as a superposition of M signal modes propagate from source to receiver along different ionospheric paths and additive background noise. The number of modes can be estimated from the number of peaks in the power-delay profile (range power spectrum).

$$\mathbf{x}_k(t) = \sum_{m=1}^{M} \mathbf{s}_{k,m}(t) + \mathbf{n}_k(t) = \sum_{m=1}^{M} A_m \mathbf{S}(\theta_m)\mathbf{c}_m(t) g_k(t,\tau_m) e^{j2\pi\Delta f_m t} + \mathbf{n}_k(t). \tag{3.1}$$

In this model, the m^{th} signal mode is denoted by $\mathbf{s}_{k,m}(t)$ for $m = 1, 2, \ldots, M$ while the additive noise is represented by $\mathbf{n}_k(t)$. The range and PRI indices are $k = 0, 1, \ldots, K-1$ and $t = 0, 1, , P-1$ respectively for data collected during one coherent processing interval (CPI) comprising P pulses.

The complex-valued scalar function $g_k(t, \tau_m)$ is the received source waveform which arises after the transmitted signal is delayed by the m^{th} mode transit time τ_m, deramped, filtered, digitized and range processed at a reference receiver (first receiver ($n = 0$)). This waveform is normalized, so the root mean square (RMS) amplitude of the m^{th} mode is denoted by A_m and the power of the mode is A_m^2. As the time delay τ_m varies with time due to the ionospheric movements, the value of τ_m is defined as the time delay associated by the signal modes between transmitter and receiver at the beginning of the CPI. The linear component of the time-delay variation of the mode during the CPI is defined by a constant Doppler shift term $e^{j2\pi\Delta f_m t}$ while the variation in the random time-delay is represented by the Doppler spread term $\mathbf{c}_m(t)$.

The terms Δf_m and θ_m in Eqn. (3.1) denote the mean Doppler shift and cone angle of arrival of the $m^t h$ mode respectively. Experimental results show that the term $e^{j2\pi\Delta f_m t}$ can be assumed to be the same in all receivers for a particular mode. The special properties of the m^{th} signal mode are partly modeled by the $N \times N$ diagonal matrix $\mathbf{S}(\theta_m)$ which represents the mean wavefront. For far-field sources and a narrowband uniform linear array, the mean wavefront is modeled as the plane wavefront and this matrix represents the steering vector elements corresponding to θ_m along its main diagonal

$$\mathbf{S}(\theta_m) = \operatorname{diag}\left[1,\, e^{jkd\sin\theta_m},\, \ldots,\, e^{jkd(N-1)\sin\theta_m}\right], \tag{3.2}$$

where d is the inter-element spacing.

The space-time model proposed by [47] adopts an order-I multi-variate scalar type auto-regressive (AR) process to generate the random vector $\mathbf{c}_m(t)$

$$\mathbf{c}_m(t) = \sum_{i=1}^{I} \alpha_{m,i} \mathbf{c}_m(t - i\Delta t) + \mu_m \xi_m(t), \tag{3.3}$$

where the scalar coefficients $\alpha_{m,i}$ and the normalizing constant, μ_m, define the Doppler spectrum characteristics of the m^{th} mode for a sampling interval of $\Delta t/f_p$ seconds.

In the case that the pulse repetition frequency, f_p, is much greater than the Doppler bandwidth, $\alpha_{m,1}(t) \simeq 1$ and $\alpha_{m,i}(t) \simeq 0, i > 1$. Also, $\mu_m = \sqrt{1 - \alpha_{m,1}(\Delta t)}$ [47]. Similarly, the spatial fluctuations of the channel causing angular spread may be described by a first order AR process:

$$\xi_m^{[n]}(t) = \beta_m(d)\xi_m^{[n-1]}(t) + \nu_m \gamma_{m,n}(t), \tag{3.4}$$

where $\xi_m^{[n]}(t)$ denotes the n^{th} element of the vector $\boldsymbol{\xi}_m(t)$, $\nu_m = \sqrt{1 - \beta_m(d)^2}$ is a scaling term with $\beta_m(d) = e^{-B(m)|1-\sin\theta_m|d}$ where $B(m)$ is the angular bandwidth of the m^{th} mode and $\gamma_{m,n}(t)$ is the driving noise term which is zero mean, complex Gaussian, process with independent identical distribution. The additive noise is assumed to be uncorrelated with the received mode waveforms $g_k(t, \tau_m)$ and have complex Gaussian distribution.

Space-time second order statistics

From Eqn. (3.1) the space-time autocorrelation series (ACS), $r_k(i\Delta t, j\Delta t)$, can be written as:

$$r_k(i\Delta t, j\Delta t) = \sum_{m=1}^{M} E\left\{ s_{k,m}^{[n]}(t) s_{k,m}^{[n]}(t-i) \right\} + \sigma_n^2 \delta(i)\delta(j), \tag{3.5}$$

where $\delta(\cdot)$ represents the Dirac delta function. Since different signal modes, $s_{k,m}^{[n]}(t)$ are statistically independent and the uncorrelated additive noise is both spatially and temporally white, the space-time ACS of the received data can be represented by the following analytical model

$$r_k(i\Delta t, j\Delta t) = \sum_{m=1}^{M} E\left\{ g_k(t, \tau_m) g_k(t, \tau_m) \right\} A_m^2 z_m^i w_m^j, \tag{3.6}$$

where $z_m = \alpha(\Delta t) e^{j2\pi\Delta f_m}$ is the temporal pole incorporating the regular component of the Doppler shift and $w_m = \beta(d) e^{j2\pi kd \sin\theta_m}$ is the spatial pole incorporating the mean DOA θ_m.

3.1.2 Parameter Estimation

This section briefly explains spectral and parametric methods for estimating the modal pairs (z_m, w_m) with the associated residues h_m from the sample space-time ACS. When synchronized FMCW signals are used to probe the particular HF channel, such estimates provide valuable information regarding to the level of Doppler spread and angular spread imposed by different ionospheric layers on the corresponding signal modes. In this case

$$g_k(t, \tau_m) = W\left(f_p \left[k - \tau_m f_b \right] \right), \tag{3.7}$$

where $W(f)$ is the normalized Fourier transform of the range processing window function, f_b is the FMCW signal bandwidth.

Subspace Method for Parameter Estimation

To describe the two-dimensional (space-time) parameter estimation technique an $(L_s - P_s + 1) \times P_s$ matrix $\mathbf{C}(i)$ and the related $(L_t - P_t + 1)(L_s - P_s + 1) \times P_t P_s$ block matrix $\mathbf{D}$ are defined as

$$\mathbf{C}(i) = \begin{bmatrix} \overline{r}(i, P_s - 1) & \dots & \overline{r}(i, 1) & \overline{r}(i, 0) \\ \overline{r}(i, P_s) & \dots & \overline{r}(i, 2) & \overline{r}(i, 1) \\ \vdots & \vdots & \ddots & \vdots \\ \overline{r}(i, L_s - 1) & \dots & 0 & 0 \end{bmatrix} \tag{3.8}$$

$$\mathbf{D}=\left[\begin{array}{cccc}\mathbf{C}(P_t-1) & \dots & \mathbf{C}(1) & \mathbf{C}(0)\\ \mathbf{C}(P_t) & \dots & \mathbf{C}(2) & \mathbf{C}(1)\\ \vdots & \vdots & \ddots & \vdots\\ \mathbf{C}(L_t-1) & \dots & 0 & 0\end{array}\right] \tag{3.9}$$

where $M < P_t < L_t$ and $M < P_s < L_s$. The sample ACS, $\overline{r}(i\Delta t, jd)$, is calculated by averaging $\hat{r}(i\Delta t, jd)$, defined below, over different CPI

$$\hat{r}(i\Delta t, jd)=\frac{1}{N_s N_t}\sum_{t=1}^{N_t}\sum_{d=}^{N_s}\mathbf{X}_k^{[d]}(t)\mathbf{X}_k^{[d+j]*}(t+i) \qquad \begin{cases} i=0,1,\dots,L_t-1\\ j=0,1,\dots,L_s-1\end{cases} \tag{3.10}$$

where $N_t = P - i + 1$ and $N_s = N - j + 1$.

In the absence of estimation errors and additive noise $\overline{r}(j\Delta t, jd) = \sum_{m=1}^{M} h_m z_m^i w_m^j$ under the assumed model. In the presence of the estimation errors and additive noise, the above value for $\overline{r}(j\Delta t, jd)$ is not exactly true but it tends to be approximately true and the accuracy of this description depends on the number of statistically independent data points used for estimation and signal to noise ratio in the available data.

To estimate the parameter pair (z_m, w_m) the matrix $\mathbf{D}^H\mathbf{D}$ is decomposed into signal and noise subspaces using its eigen-decomposition

$$\mathbf{D}^H\mathbf{D}=\mathbf{Q}_s\mathbf{\Lambda}_s\mathbf{Q}_s^H+\mathbf{Q}_n\mathbf{\Lambda}_n\mathbf{Q}_n^H, \tag{3.11}$$

where ^{H} represents the Hermitian of a matrix, $\mathbf{Q}_s$ and $\mathbf{Q}_n$ represent the eigenvectors corresponding to the signal and noise sub-spaces respectively. The required parameters can then be obtained using a MUSIC-like approach [1,3].

In an alternative approach, define an $L_t \times L_s$matrix $\mathbf{T}$ based on the measured data such that its $(i,j)^{\text{th}}$ element equals $\hat{r}(i\Delta t, j\Delta d)$

$$\mathbf{T}=\left[\begin{array}{cccc}\hat{r}(0,0) & \hat{r}(0,1) & \cdots & \hat{r}(0,L_s-1)\\ \hat{r}(1,0) & \hat{r}(1,1) & \cdots & \hat{r}(1,L_s-1)\\ \vdots & \vdots & \ddots & \vdots\\ \hat{r}(L_t-1,0) & \hat{r}(L_t-1,1) & & \hat{r}(L_t-1,L_s-1)\end{array}\right]. \tag{3.12}$$

It is possible to factorize this matrix $\mathbf{T}$ as

$$\mathbf{T}=\sum_{m=1}^{M} h_m \mathbf{z}_m \mathbf{w}_m^H. \tag{3.13}$$

The model parameters, h_m, $\mathbf{z_m}$, and $\mathbf{w_m}$ are estimated as those which provide the best least squares fit to $\mathbf{T}$. This multidimensional optimization is separable and we can calculate matrices $\mathbf{Z}$ (the matrix of all M vectors $\mathbf{z_m}$)and $\mathbf{W}$ (defined similarly) individually. After calculating these parameters, the vector of residues $\mathbf{h} = [h_1, h_2, \dots, h_M]$, $\mathbf{T}$ is estimated such that it minimizes the difference between the model and sample ACS in the least square sense.

$$\hat{h} = \arg\min \|\hat{r} - \mathbf{V}\mathbf{h}\| \tag{3.14}$$

Knowing the parameters $(\mathbf{z_m}, \mathbf{w_m})$ one can calculate the parameter vector ϕ using the equations $z_m = \alpha(\Delta t)e^{j2\pi\,\Delta f_m}$ and $w_m = \beta(\Delta d)e^{j2\pi\,\frac{\Delta d}{\lambda}\sin\theta_m}$ for each mode.

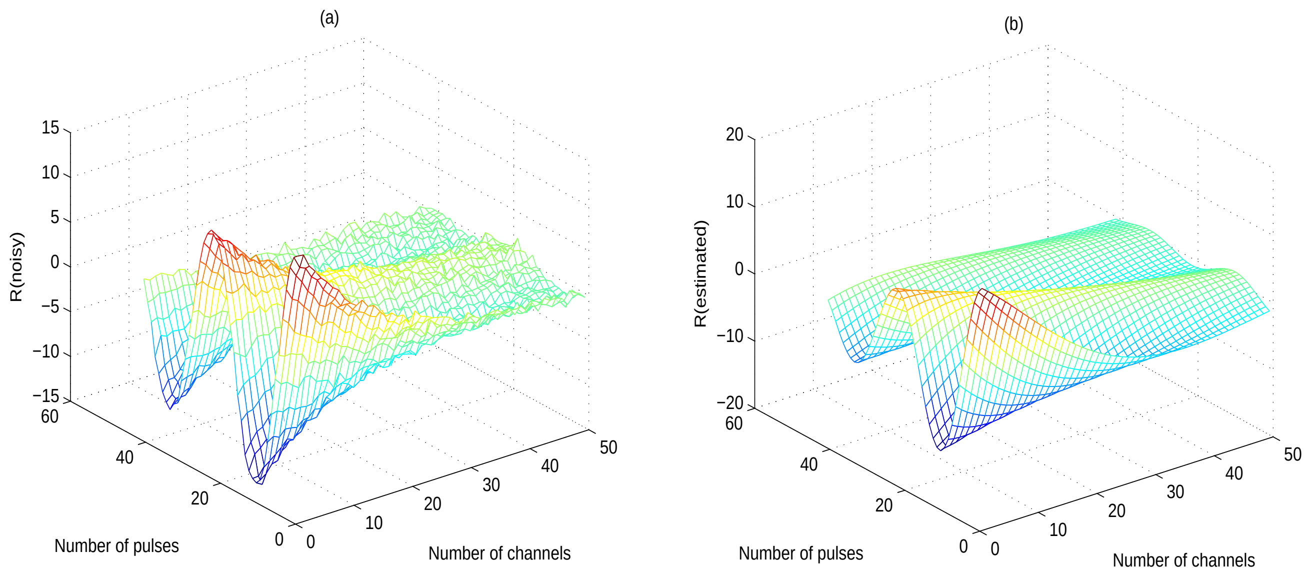

Figure 3.1: Real part of (a) noisy and (b) estimated autocorrelation function.

Results

A simulation and a measurement result are presented here to evaluate the model. In the first result, we consider $M = 2$ with the parameters of the two modes chosen to be:

$$\begin{aligned} \alpha &= [.998\ .997], \\ \beta &= [.92\ .963], \\ \theta &= [22.2\ 21.7], \ , \\ \Delta f &= [.46\ .39], \\ h &= [9.46\ 5.23] \end{aligned}$$

and calculate the simulated autocorrelation function as:

$$r(i\Delta t, j\Delta d) = \sum_{m=1}^{M} h_m z_m^i w_m^i$$

and then we add measured white Gaussian noise with signal to noise ratio (SNR) of 20dB to the calculated autocorrelation and estimate the parameters using the least squares method. The estimated parameters are:

$$\begin{aligned} \alpha &= [0.9839 \quad 0.9756] \\ \beta &= [0.9562 \quad 0.9562] \\ \theta &= [\ 20.8594 \quad 20.8594] \\ \Delta f &= [0.4605 \quad 0.3855] \\ h &= [8.8437 \quad 6.7261] \end{aligned}$$

Fig. 3.1shows the real part of noisy and estimated autocorrelation function. As the results show there is some error in estimation of autocorrelation function due to the noise.

To assess the model using the measured signals, we choose some ranges of a 3D (270 ranges $\times$ 4096 pulses $\times$ 15 channels) measured signal which contain ionospheric clutter and use Eqn. (3.10) to calculate their autocorrelation function. Figures 3.2, 3.3 and 3.4 show the autocorrelation function

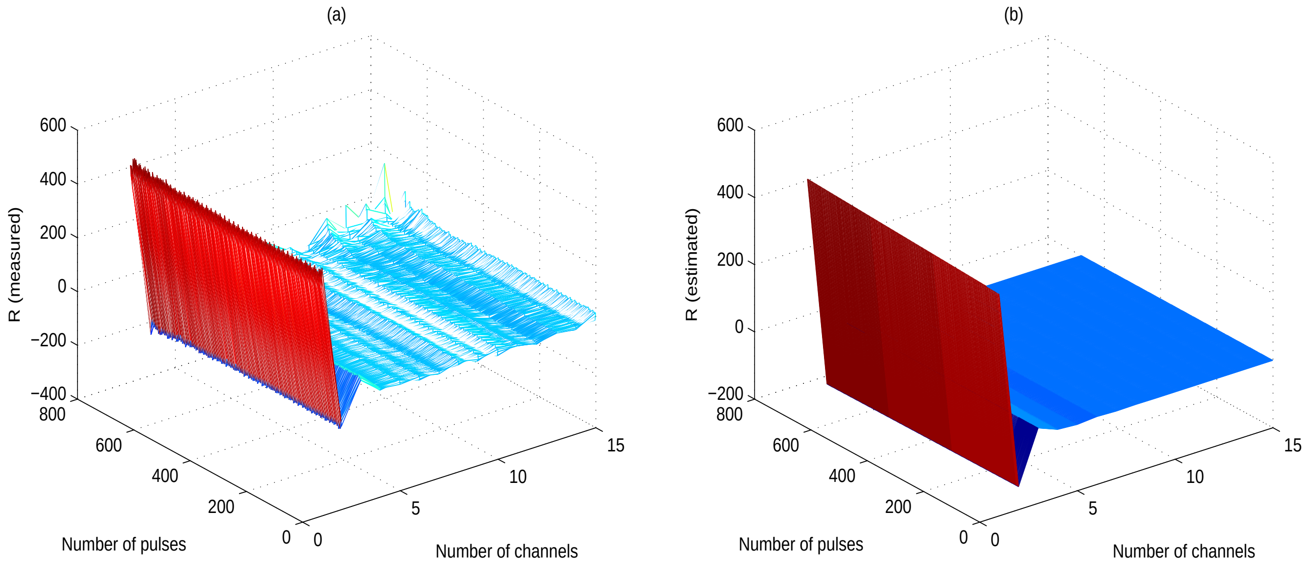

Figure 3.2: Real part of (a) measured and (b) estimated autocorrelation function for range bin 220.

of the signal when $\Delta t = 6$ and$\Delta d = 1$, so the numbers of pulses are 682. Table 3.1 shows the estimated parameters for these figures using the measured autocorrelation. To evaluate the angle of arrival for the measured signal, we calculate the mean angular power spectrum of the signal as follows:

Table 3.1: Distributed signal model parameters estimated from the sampled autocorrelation function.

Figure	α	β	$\Delta\theta$	Δf	h
Fig.2	1.0	0.3341	65.32	-8.96e-5	460.16
Fig.3	0.9934	0.9741	5.82	0.2609	711.20
Fig.4	.9713	.94386	-36.55	0.4406	-0.8024

$$P_x(k,\theta) = \frac{S^H(\theta)R_x(k)S(\theta)}{N^2} \; , S(\theta) = [1 \, e^{j2\pi\Delta d \sin\theta/\lambda} ... \, e^{j2\pi(N-1)\Delta d \sin\theta/\lambda}]^T \tag{3.15}$$

where

$$R_x(k) = \frac{1}{P}\sum_{t=1}^{P} x_k(t)\, x_k^H(t) \tag{3.16}$$

is the unbiased sample spatial covariance matrix estimated for the k^{th}range cell in a particular coherent processing time. The maximum value of P_x shows the angle of arrival of the signal.

Also,to evaluate the Doppler frequency, we calculate the mean Doppler spectrum $(P_y(k,\Delta f))$. To determine $P_y(k,\Delta f)$ let the D-dimensional complex vector $y_k(n,t,\Delta t)$contain the slow time samples recorded in the n^{th}receiver and the k^{th} range starting at the t^{th} PRI with consecutive samples being spaced by Δt PRI. This vector can be written as:

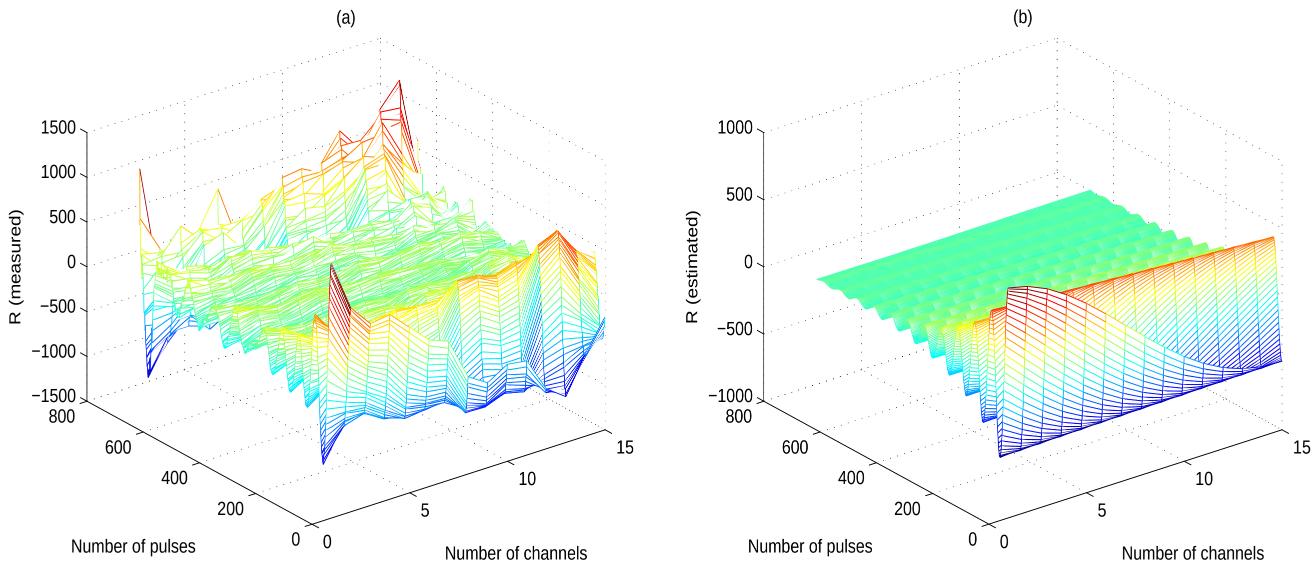

Figure 3.3: real part of (a) measured and (b) estimated autocorrelation function for range bin 140.

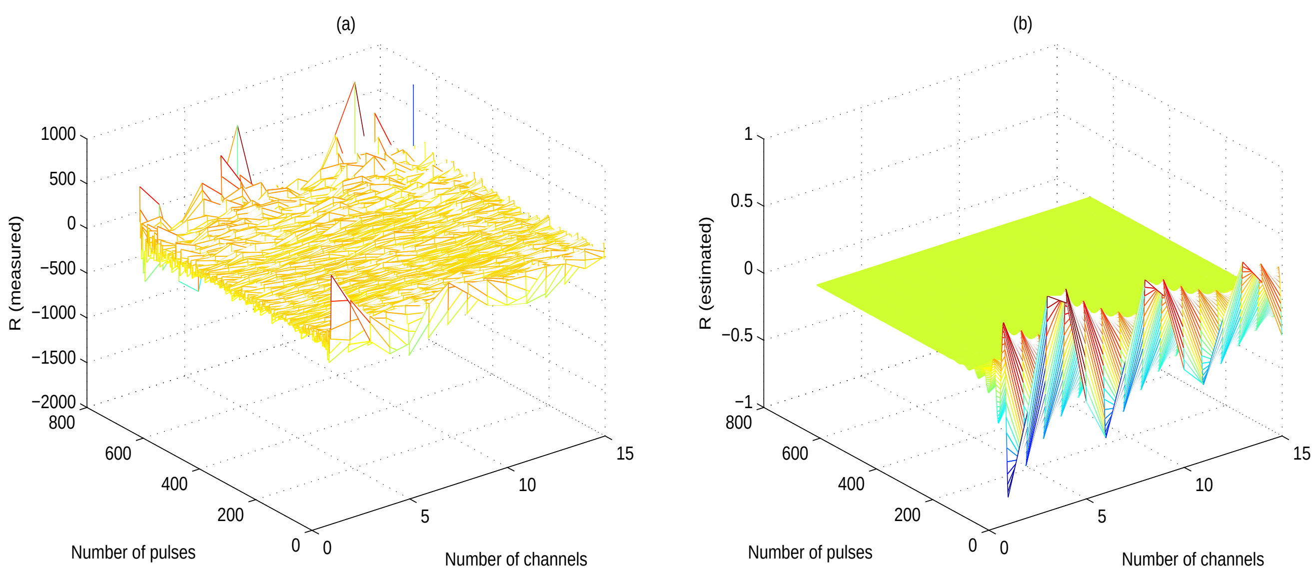

Figure 3.4: real part of (a) measured and (b) estimated autocorrelation function for range bin 180.

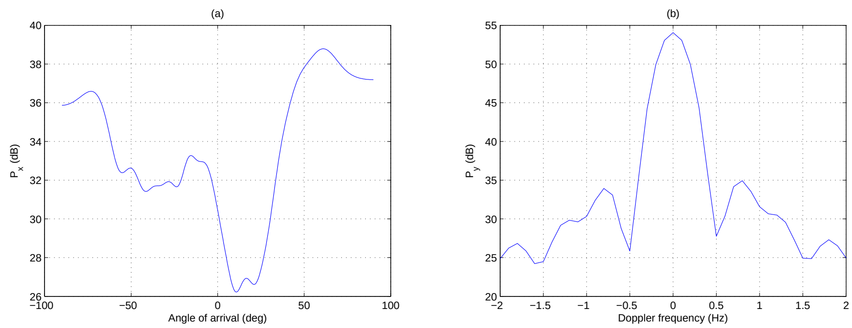

Figure 3.5: (a)Angle of arrival and (b) Doppler frequency spectrum for range bin 220.

$$y_k(n,t,\Delta t) = [x_k^{[n]}(t)\, x_k^{[n]}(t+\Delta t) \ldots x_k^{[n]}(t+(D-1)\Delta t)]^T \tag{3.17}$$

where $x_k^{[n]}(t)$ is the output of the n^{th} receiver at the k^{th} range starting at the t^{th} PRI. The temporal sample covariance matrix estimated for the k^{th} range cell in the particular dwell is denoted by :

$$\mathbf{R}_y(k) = \frac{1}{N(P-D\Delta t+1)} \sum_{n=1}^{N} \sum_{t=1}^{P-D\Delta t+1} \mathbf{y}_k(n,t,\Delta t)\mathbf{y}_k^H(n,t,\Delta t) \tag{3.18}$$

The matrices are averaged over different dwells to form the mean sample temporal covariance matrix $\bar{\mathbf{R}}_y(k)$ which is used to evaluate the mean Doppler power spectrum $P_y(k,\Delta f)$ as:

$$P_y(k,\Delta f) = \frac{\mathbf{v}^H(\Delta f)\,\bar{\mathbf{R}}_y(k)\;\mathbf{v}(\Delta f)}{D^2} \tag{3.19}$$

$$\mathbf{v}(\Delta f) = [1\; e^{j2\pi\Delta f/f_p'} \ldots e^{j2\pi(D-1)\Delta f/f_p'}]^H \tag{3.20}$$

where the D-dimensional vector $v(\Delta f)$ is the complex frequency phasor corresponding to a Doppler shift of Δf Hz observed with an effective PRF of $f_p' = f_p/\Delta t$ Hz. The maximum value of P_y shows the Doppler frequency of the signal.

Figures 3.5, 3.6 and 3.7 show the value of P_x versus angle of arrival and the value of P_y versus Doppler frequency for different ranges. As the figures show the maximum of the P_x are at $\theta = 61^o$, $\theta = 6.5^o$ and $\theta = -38.5^o$ and the maximum value of P_y are at $\Delta f = 0$ Hz, $\Delta f = -0.1$ Hz and $\Delta f = 0.1$ Hz for ranges of 220,149 and 180 respectively. Here because the measured autocorrelation function has approximately an exponential shape, in Figures 3.2 and 3.3, the estimated autocorrelation follows the measured autocorrelation with an acceptable accuracy. But as seen in Figure 3.4, the measured autocorrelation does not have an exponential shape and so we cannot estimate parameters correctly with this model.

In conclusion to this section, our implementation and analysis of the model of [1, 47] suggests that while the model is analytically appealing, it does not model the measured ionospheric data acquired by the DRDC HFSWR.

3.2 Data Model of Riddolls [2]

In this part of the project, we implement and examine a radio wave propagation approach to model ionospheric clutter. The method, which was recently developed by Dr. Riddolls of Defense

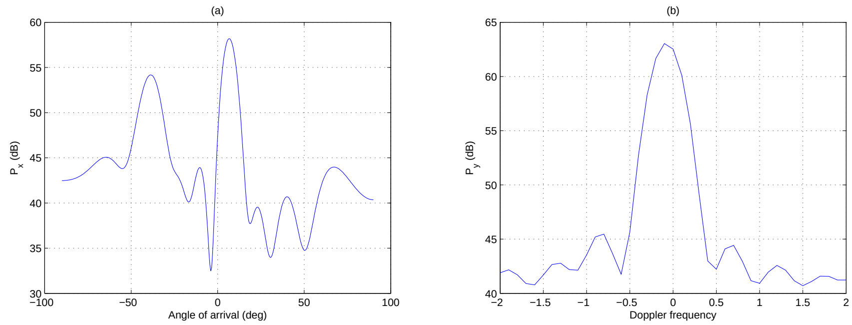

Figure 3.6: (a)Angle of arrival and (b) Doppler frequency spectrum for range bin 140.

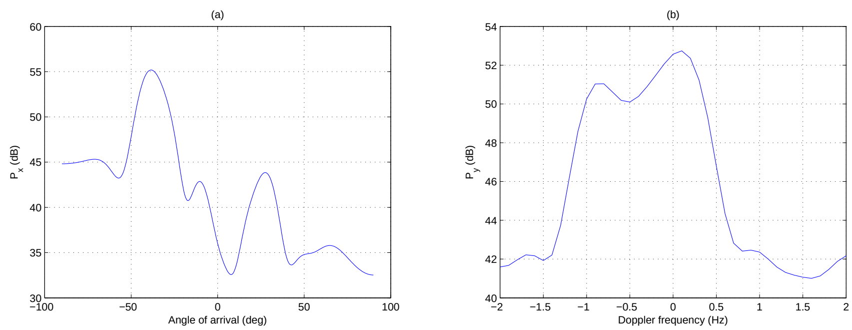

Figure 3.7: (a)Angle of arrival and (b) Doppler frequency spectrum for range bin 180.

Research and Development Canada (DRDC) [2], uses a ray tracing model and treats irregularities as perturbations of a "quiescent" path solution without irregularities. In this report we briefly describe this method and compare simulation results based on this method to measured data.

The model of [2] develops a theory of High-Frequency (HF) radio wave propagation in the earth's ionosphere that accounts for the effects of ionospheric plasma density irregularities. The model assumes an anisotropic ionospheric plasma that is inhomogeneous in the vertical direction. The effects of the irregularities are modeled as small perturbations to the quiescent solution. The perturbations are evaluated for the case of random plasma density irregularities with a power-law wave number spectrum, which leads to the predicted phase power spectra of the signal properties as a function of wave number and frequency.

3.2.1 Path integral formulation of wave packet properties

The model used here is developed in some detail in [2] and we describe it briefly here. The plasma dispersion relation is written as an implicit function $G(r,t,k,\omega) = 0$ (where $\mathbf{k}$ is the wave number and ω is the angular frequency) [1] that accounts for slow spatial-temporal variations in $\omega_{ps} = q_s^2 N_s/\varepsilon_0 m_s$ (plasma frequency of species s (oxygen ions or electrons)) and $\omega_{cs} = |q_s|\,B_0/m_s$ (cyclotron frequency of species s), where m_s is the mass of the species, N_s is the species density and $B_0 = B_0\hat{z}$ is the magnetic flux density which is assumed to be in the $\hat{z}$ direction. As the wave propagates through the plasma, it must always satisfy the plasma dispersion relation such that $G = 0$ along the entire wave trajectory in (r,t,k,ω)-space. If τ is a variable parameterizing this trajectory, and G is always identically zero along this trajectory, then $dG/d\tau = 0$:

$$\frac{d}{d\tau}G(r,t,k,\omega) = \frac{\partial G}{\partial r}\frac{dr}{d\tau} + \frac{\partial G}{\partial t}\frac{dt}{d\tau} + \frac{\partial G}{\partial k}\frac{dk}{d\tau} + \frac{\partial G}{\partial \omega}\frac{d\omega}{d\tau} = 0. \tag{3.21}$$

The radar pulse is considered as a wave packet in the form

$$E(r,t) = \frac{1}{(2\pi)^2}\int\iiint E(k,\omega)e^{i(k.r-\omega t)}dkd\omega. \tag{3.22}$$

If the spatial variation of $E(k,\omega)$ is slow compared to $2\pi/|k|$, and the temporal variation is slow compared to $2\pi/\omega$, then constructive interference occurs when the integrand phase is a constant. Differentiating this phase with respect to t and $\mathbf{k}$,and equating to zero, yields:

$$\frac{dr}{dt} = \frac{\partial \omega}{\partial k} = -\frac{\partial G/\partial k}{\partial G/\partial \omega} = \frac{dr/d\tau}{dt/d\tau}. \tag{3.23}$$

So we have

$$\frac{dr}{d\tau} = \frac{\partial G}{\partial k}. \tag{3.24}$$

If the arbitrary parameter τ is defined such that

$$\frac{dt}{d\tau} = -\frac{\partial G}{\partial \omega}, \tag{3.25}$$

then from Eqn. (3.23) we have

$$\frac{dk}{d\tau} = -\frac{\partial G}{\partial r}, \tag{3.26}$$

$$\frac{d\omega}{d\tau} = -\frac{\partial G}{\partial t}. \tag{3.27}$$

A more explicit description can be achieved by assuming that the medium is plane-stratified, such that ω_{ps} and ω_{cs} vary only with altitude. The wave packet properties can be written as path integrals of Eqns. (3.24)–(3.27), namely the skip distance,

$$\Delta r = -\int \frac{\partial k_z}{\partial k}dz, \tag{3.28}$$

the group delay

$$\Delta t = -\int \frac{\partial k_z}{\partial \omega}dz, \tag{3.29}$$

the direction of arrival (DOA),

$$\Delta k = -\int \frac{\partial k_z}{\partial r}dz, \tag{3.30}$$

and the Doppler shift

$$\Delta \omega = -\int \frac{\partial k_z}{\partial t}dz. \tag{3.31}$$

The background plasma density is denoted as N_0 where the irregularity density is denoted as N_1, such that the total plasma density is $N= N_0+N_1$, and N_1 has zero mean. The perturbed wave number is given by:

$$k_z(N) = k_z(N_0) + N_1\frac{\partial k_z}{\partial N_1}|_{N_0} \equiv k_{z0} + k_{z1}. \tag{3.32}$$

Using Eqn. (3.32) the wave packet properties can be approximated by

$$\Delta r_1 = -\int N_1 \frac{\partial^2 k_z}{\partial N\, \partial k} dz, \tag{3.33}$$

$$\Delta t_1 = \int N_1 \frac{\partial^2 k_z}{\partial N\, \partial \omega} dz, \tag{3.34}$$

$$\Delta k_1 = \int N_1 \frac{\partial N_1}{\partial r} \frac{\partial k_z}{\partial N} .dz, \tag{3.35}$$

$$\Delta \omega_1 = -\int \frac{\partial N_1}{\partial t} \frac{\partial k_z}{\partial N} dz. \tag{3.36}$$

We take the quantities N_1, $\frac{\partial N_1}{\partial r}$ and $\frac{\partial N_1}{\partial t}$ to be zero-mean random variables, and thus the means of Δr_1, Δt_1, Δk_1 and $\Delta\omega_1$ are also zero.

3.2.2 Second-order statistics

We can write Eqns. (3.32)–(3.33) in the form

$$h(x, y, z, t) = \int_0^z g(x, y, z', t)\, f(z')\, dz', \tag{3.37}$$

where f is deterministic and g is random. Using Eqn. (3.37) we can write the power spectrum of h as:

$$S_h(k_x, k_y, k_z, \omega, z) = 2\pi\delta(k_z) \int_0^z f^2(z') S_g(k_x, k_y, 0, \omega, z')\, dz'. \tag{3.38}$$

By assuming that the magnetic field lies in the y-z plane, the form is of the spectrum model for $k_{iz} = 0$ becomes:

$$S_{N_1} = \frac{4\sqrt{2\alpha_i}\pi^2 E[N_1^2(z)] k_0^{-3}}{1 + k_0^{-4}[k_{ix}^2 + (l_z^2 + \alpha_i l_y^2) k_{iy}^2]^2} \delta[|\omega_i| - (k_{ix}^2 + l_z^2 k_{iy}^2)^{1/2} v_d] \tag{3.39}$$

where v_d is the plasma diamagnetic drift velocity,k_0 is a scalar length parameter, α_i is an anisotropy parameter, k_i is the irregularity wave number, $E[N_1^2(z)]$ is the variance of the density fluctuations which is assumed to be a function of altitude z and $\hat{l} = (l_x, l_y, l_z)$ is a unit vector. We suppose that the magnetic field of the earth follows this unit vector.

We consider only the first-order phase perturbation due to irregularities in the ionosphere, which is related to the wave number perturbations by

$$\Delta k_{x1} = \frac{\partial \phi_1}{\partial x}, \tag{3.40}$$

$$\Delta k_{y1} = \frac{\partial \phi_1}{\partial y}. \tag{3.41}$$

Hence, the wave number spectra are related to the phase spectrum by

$$S_{\Delta kx1} = k_x^2 S_{\phi 1}, \tag{3.42}$$

$$S_{\Delta ky1} = k_y^2 S_{\phi 1}. \tag{3.43}$$

So the phase spectrum is given by

$$S_{\phi 1} = b\,(z)\,\frac{\delta(k_z)\delta([|\omega| - (k_x^2 + l_z^2 k_y^2)^{1/2} v_d]}{1 + k_0^{-4}[k_x^2 + (l_z^2 + \alpha_i l_y^2)k_y^2]^2}, \tag{3.44}$$

where

$$b(z) = a \int_0^z E[N_1^2(z')] \left(\frac{\partial k_z}{\partial N}\right)^2 dz' = \frac{E(\varphi^2)[16\pi^2 \sqrt{(l_z^2 + \alpha_i l_y^2)}]}{k_0^2}. \tag{3.45}$$

This phase spectrum is four-dimensional (k_x, k_y, k_z, ω). However, an HFSWR with a linear array can only resolve two of these dimensions, which are the k_x and ω dimensions for the case of an East-West receive array. By integrating out the k_y and k_z dimensions in the East-West receive array case, we have

$$S_{\phi_1} = \frac{2b\,(z)\;|\omega|}{(l_z\, v_d^2)\sqrt{(\omega^2/v_d^2 - k_x^2)}(1 + k_0^{-4}[k_x^2 + (l_z^2 + \alpha_i l_y^2)(\omega^2/v_d^2 - k_x^2)/l_z^2]^2)}. \tag{3.46}$$

This spectrum is nonzero in the region $|\omega| > k_x\, v_d$.

In the case of HFSWR, the clutter of interest involves near-vertical signal ray paths. This means that the quantity $b(z)$ in Eqn. (3.45), which is essentially the strength of the phase scintillation, does not depend on the azimuth angle and can therefore be viewed as a constant. The amplitude spectrum is also in the form of Eqn. (3.46) with a different constant value of $b(z)$ named $b^{'}(z)$.

$$S_{A_1} = \frac{2b^{'}\,(z)\;|\omega|}{(l_z\, v_d^2)\sqrt{(\omega^2/v_d^2 - k_x^2)}(1 + k_0^{-4}[k_x^2 + (l_z^2 + \alpha_i l_y^2)(\omega^2/v_d^2 - k_x^2)/l_z^2]^2)}, \tag{3.47}$$

$$b^{'}(z) = \frac{E(A_1^2/A_0^2)[16\pi^2 \sqrt{(l_z^2 + \alpha_i l_y^2)}]}{k_0^2}. \tag{3.48}$$

where A_0 is the constant part of the signal amplitude and A_1 is the fluctuating part of the signal amplitude.

3.2.3 Modeling the Space-Time-Range Data Cube

The data cube represents the composite of N-dimensional antenna array snapshot $x_k(t, n)$ $(n = 0, 1, ..., N)$ recorded at the k^{th} range cell in the t^{th} Pulse Repetition Interval (PRI). To generate the data cube with this phase and amplitude power spectrum, we consider a range bound in the z direction which begins from the distance to the first ionospheric range bin z_0 and calculate the value of $b(z)$ for each range as

$$b(z) = b(z_0) + \beta(z - z_0). \tag{3.49}$$

where β is a constant coefficient which must be chosen properly to have an accurate result. Also because the value of plasma drift velocity, v_d, changes slightly in different ranges, we consider v_d as $v_d = v_{d0} \pm dv$ where dv is a random variable. By using the values of $b(z)$ and v_d for each range bin, we create the phase and amplitude of a two dimensional (array element-pulse) signal for each range bin by filtering the white noise through a 2-dimensional LTI filter whose impulse response is found by taking the square root of the amplitude of the phase and amplitude spectrum described in Eqns. (3.46) and (3.47), inverse Fourier transforming, and tapering with a rectangular window function respectively. Here, to mimic the DRDC data sets, we consider Frank code with eight segments as the transmitted signal waveform that minimizes the effect of high range sidelobes and multiple-time round clutter. The actual code sequences used are:

1. $\{0, 0, 0, 0, 0, 0, 0, 0\}$
2. $\{-\pi/4, -\pi/2, -3\pi/4, \pi, 3\pi/4, \pi/2, \pi/4, 0\}$
3. $\{-\pi/2, \pi, \pi/2, 0, -\pi/2, \pi, \pi/2, 0\}$
4. $\{-3\pi/4, \pi/2, -\pi/4, \pi, \pi/4, -\pi/2, 3\pi/4, 0\}$
5. $\{\pi, 0, \pi, 0, \pi, 0, \pi, 0\}$
6. $\{3\pi/4, -\pi/2, \pi/4, \pi, -\pi/4, \pi/2, -3\pi/4, 0\}$
7. $\{\pi/2, \pi, -\pi/2, 0, \pi/2, \pi, -\pi/2, 0\}$
8. $\{\pi/4, \pi/2, 3\pi/4, \pi, -3\pi/4, -\pi/2, -\pi/4, 0\}$

and the radar transmitted signal at complex baseband for the i^{th} code segment is represented by:

$$P_i(\tau) = A(\tau)[cos(\phi_i(\tau)) + jsin(\phi_i(\tau))] \;\; i = 1, 2, ..., 8. \tag{3.50}$$

for $0 < \tau \leq T$, and $P_i(\tau) = 0$ for $\tau > T$, where T is the segment length. In this phase coding, the segment length, T, is divided in to eight subintervals. In each subinterval the phase, $\phi_i(\tau)$, is assumed as one of the elements of the i^{th} segment. These eight codes are transmitted sequentially. The matched filter response is obtained by processing the returns of the eight waveforms with their replicas and coherently summing the results.

To consider the effect of transmitted signal, we first calculate the ambiguity function of transmitted signal as:

$$S(\zeta) = \int_{-\infty}^{\infty} Q(\tau).Q^*(\zeta - \tau)d\tau, \;\; Q = \sum_{i=1}^{8} matched\, filter(P_i). \tag{3.51}$$

and then convolve the resulting signals of different range bins with this ambiguity function to create a data cube. To simulate the random bias, $\triangle f$, in Doppler frequency seen in the measured data cube, we then multiply the 2D pulse-range signal for all antenna elements by $e^{j2\pi\triangle ft}$ in the time domain.

3.2.4 Simulation Results

To simulate the data cube, we consider the following values for the parameters in Eqns. (3.46) and (3.47):
$E(\varphi^2) = 10^2 - 10^3$.
$E(A_1^2/A_0^2) = 10^{-4} * E(\varphi^2)$.
$l_z = \sqrt{3}/2$.
$l_y = 1/2$.
$\alpha_i \approx 3000$.
$v_d = 7 \pm dv$ m/s where dv is a random variable between -2 and 2.
$k_0 = 10^{-4}$/m.

Figure 3.8 shows the shape of S_{ϕ_1} and the corresponding autocorrelation when $v_d = 5$. S_{A_1} has the same shape as S_{ϕ_1} with a different amplitude. The transmitted signal pulse consists of eight phase code segments, each of these segments in turn consists of eight elements, where each element is $55\mu s$ long, and thus each segment is $440\mu s$ long. The pulses are emitted every $8ms$, thus the complete code is emitted every $64ms$ and the PRF of the data set is $1/64ms = 15.625Hz$. There are 4096 of these pulses, so the data set is 262.1444 seconds long. The antenna array contains 16 antenna elements that are separated by $33.33m$ from each other. The distance to the first range bin (z_0 in Eqn.(3.49)) is considered $62.75km$ and the space between range bins (range resolution) is $1.5km$. The value of β in Eqn.(3.49) is equal to 10^3 and the parameter $\triangle f$, which shows the random bias in doppler frequency, is considered as a random variable between -0.4 and 0.4. Also, the amplitude of the simulated signal is multiplied by 5×10^6 to have the same scale as the measured signal.

Figures 3.9 and 3.10 show the real and imaginary part of the simulated signal for the range bins 34 and 12 when $E(\varphi^2)$ is a random variable in the range of $1 \sim 2 \times 10^2$ and $2 \sim 3 \times 10^2$ respectively. The corresponding angle-doppler plot of these signals are shown in Fig. 3.11. Figures 3.12, 3.13 and 3.14 shows the same results for measured signals. By comparing these results, one can see that the simulated signals follow the measured signals with remarkable accuracy. Figures 3.15 and 3.16 show the Doppler-range plot of the simulated and measured signals respectively. As the figures show, the power of measured signal in frequency domain goes to zero faster than the simulated signal. This condition is shown clearly in Fig. 3.17 where the results are shown for a specific range bin.

3.2.5 Summary

This section presented a core contribution of the work undertaken in this project. A new model of radio wave propagation in ionosphere plasma density irregularities has been developed. This model assumes an anisotropic ionospheric plasma that is inhomogeneous in the vertical direction. In this model we consider only the first-order phase and amplitude perturbation due to irregularities in the ionosphere to model the phase and amplitude power spectrum of the signal. The two dimensional (array element-pulse) signal for each range bin is then created by filtering the white noise through a 2-dimensional LTI filter whose impulse response is found by taking the square root of the amplitude of the phase and amplitude spectrum, inverse fourier transforming and tapering with a rectangular window function respectively. To consider the effect of the transmitted signal, the ambiguity function of the transmitted signal is convolved with the resulting signals of different range bins to make a data cube. To show the accuracy of this method, some simulation results has been demonstrated in this report. Comparing these simulated results with measured signals shows that the simulation results follow the measured signals with remarkable accuracy. The only problem in these results is that the power of the measured signal in frequency domain goes to zero faster than its simulated counterpart; this issue must must be solved as a future work. In addition, clearly this model is has been tested with data from only a single radar. The general applicability of this approach to other ionospheric scenarios is an open question.

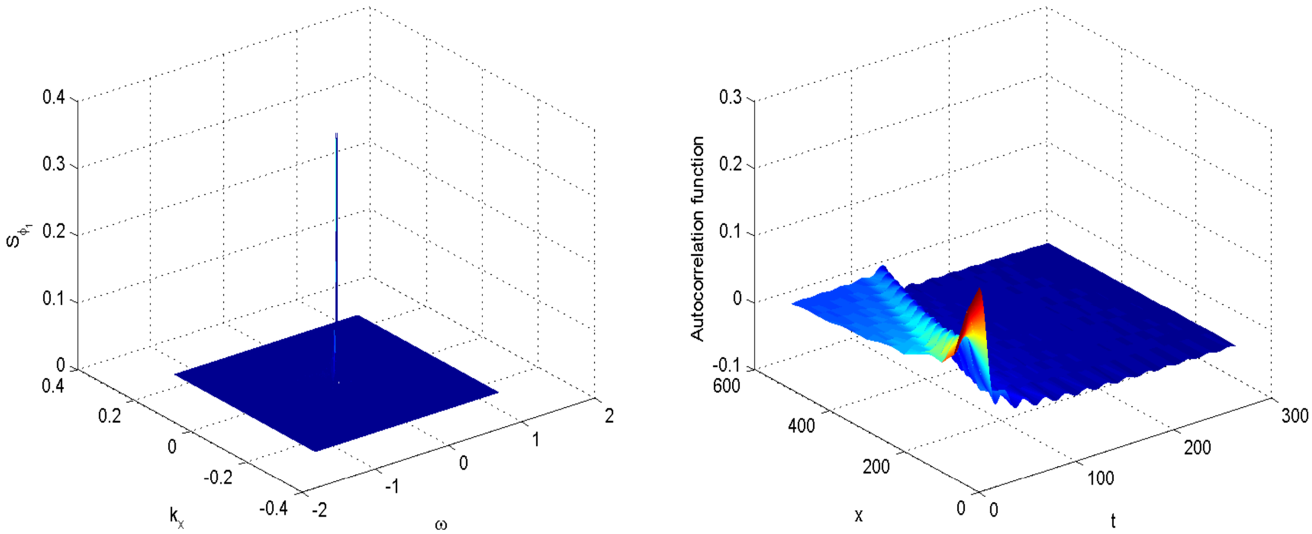

Figure 3.8: (a) Phase power spectrum and (b) autocorrelation function of the signal.

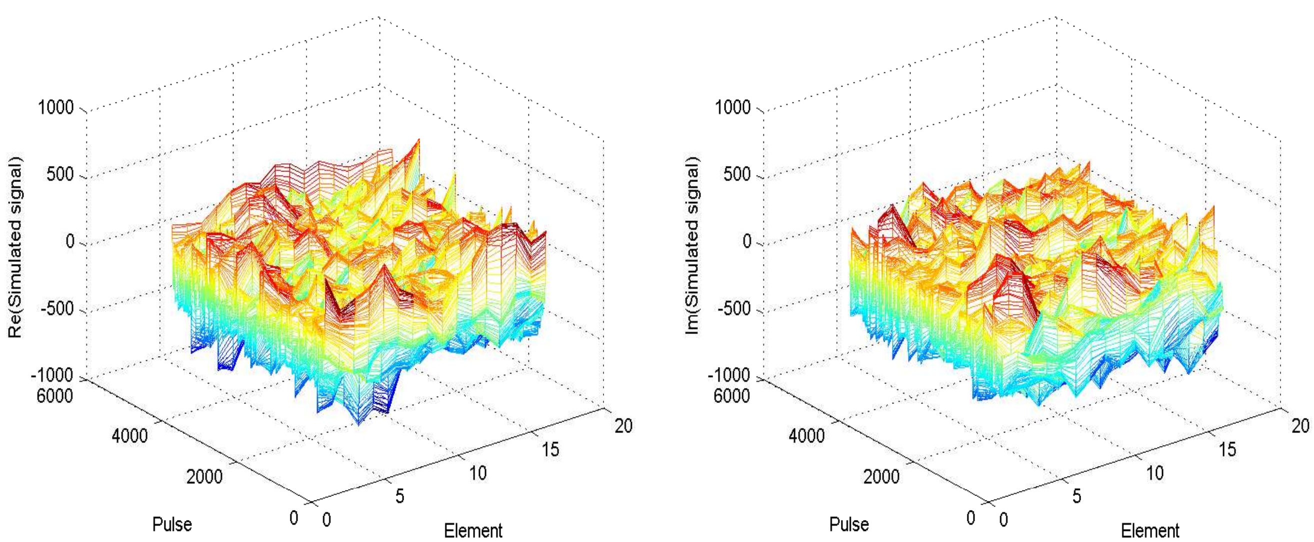

Figure 3.9: (a) Real and (b) imaginary part of the simulated signal for the range bin 34 when $E(\varphi^2)$ is a random value between 1×10^2 and 2×10^2 .

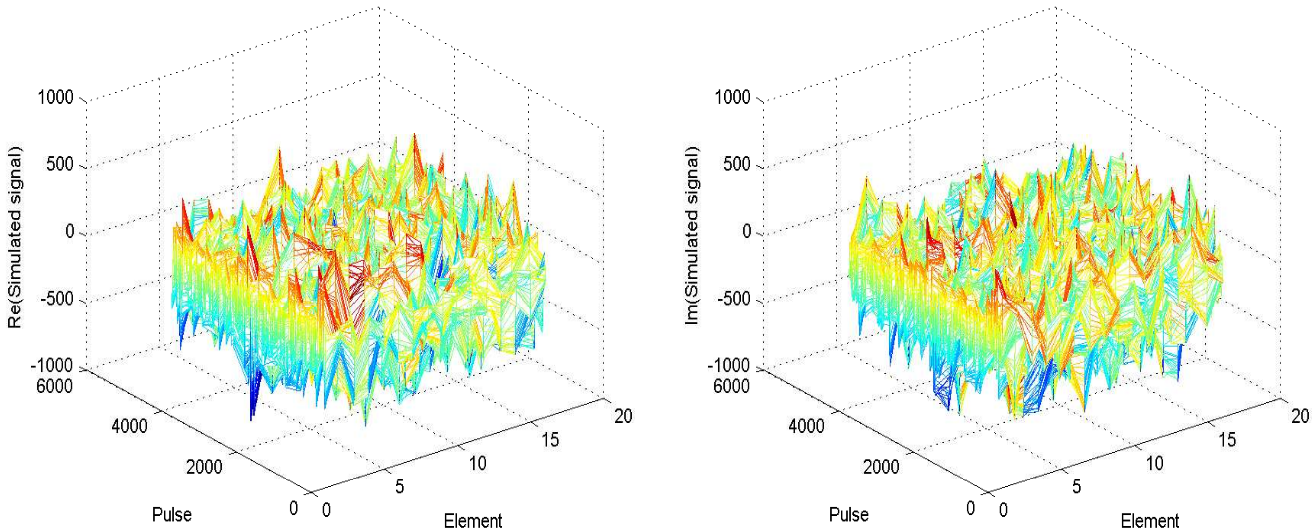

Figure 3.10: (a) Real and (b) imaginary part of simulated signal for the range bin 12 when $E(\varphi^2)$ is a random value between 2×10^2 and 3×10^2
.

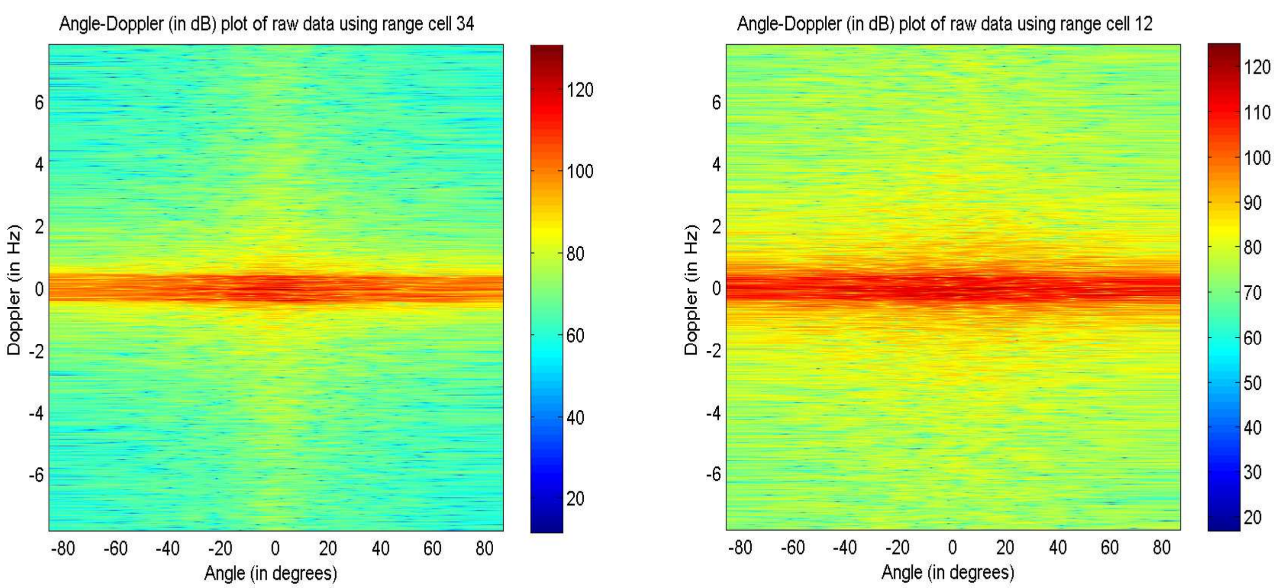

Figure 3.11: Angle-doppler plot of the simulated signal (a) for the range bins 34 and (b) 12.

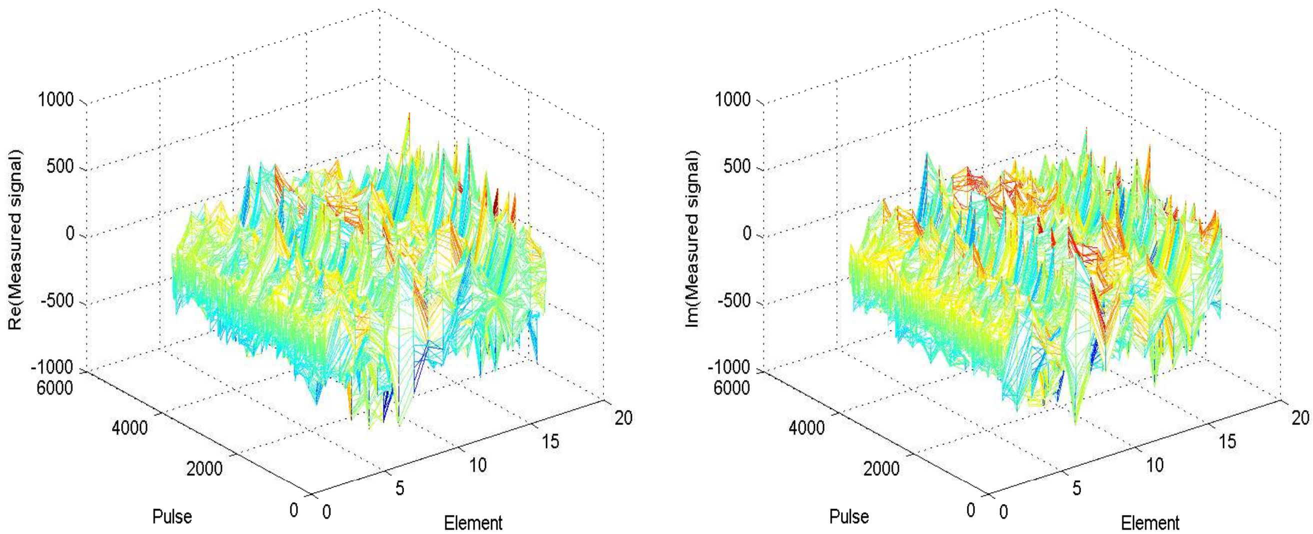

Figure 3.12: (a) Real and (b) imaginary part of measured signal for the range bin 230.

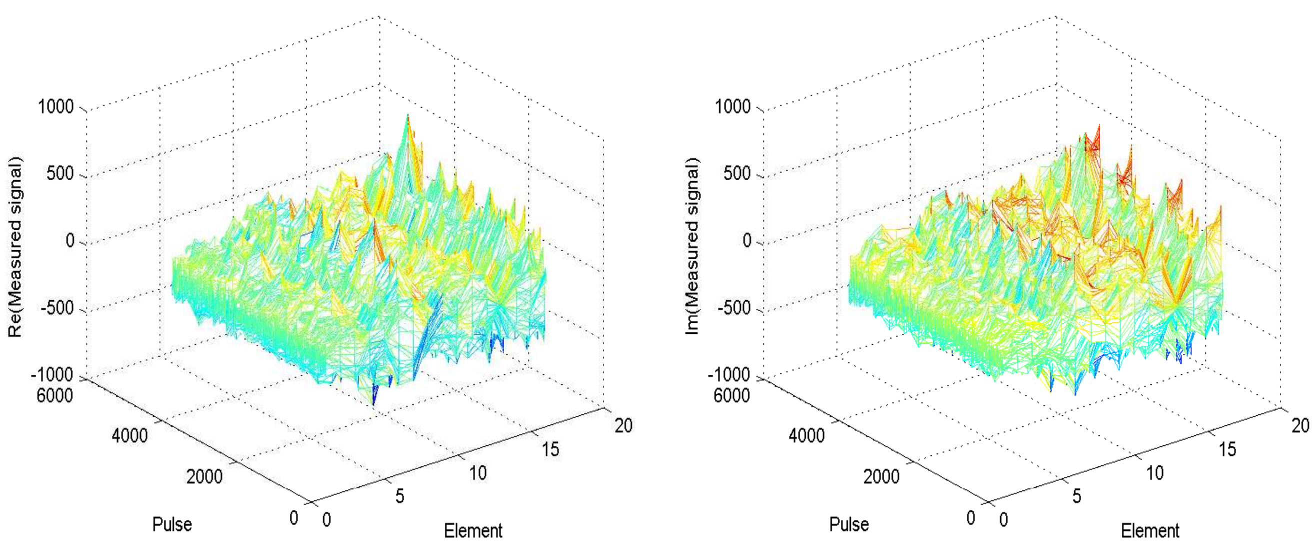

Figure 3.13: (a) Real and (b) imaginary part of measured signal for the range bin 260.

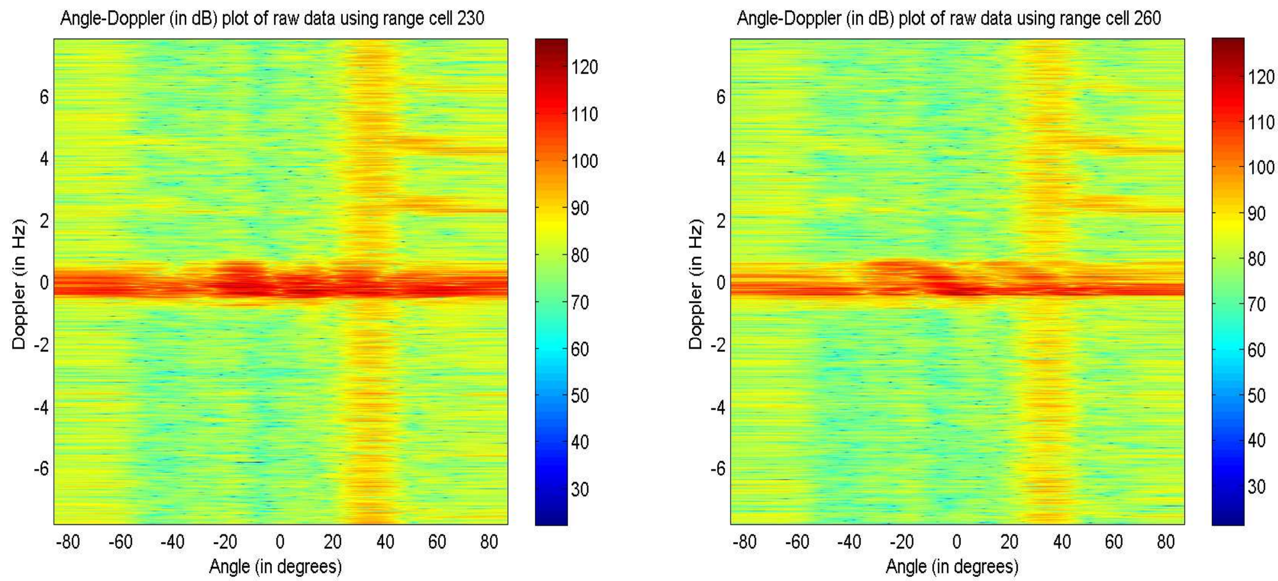

Figure 3.14: Angle-doppler plot of the measured signal (a) for the range bins 230 and (b) 260.

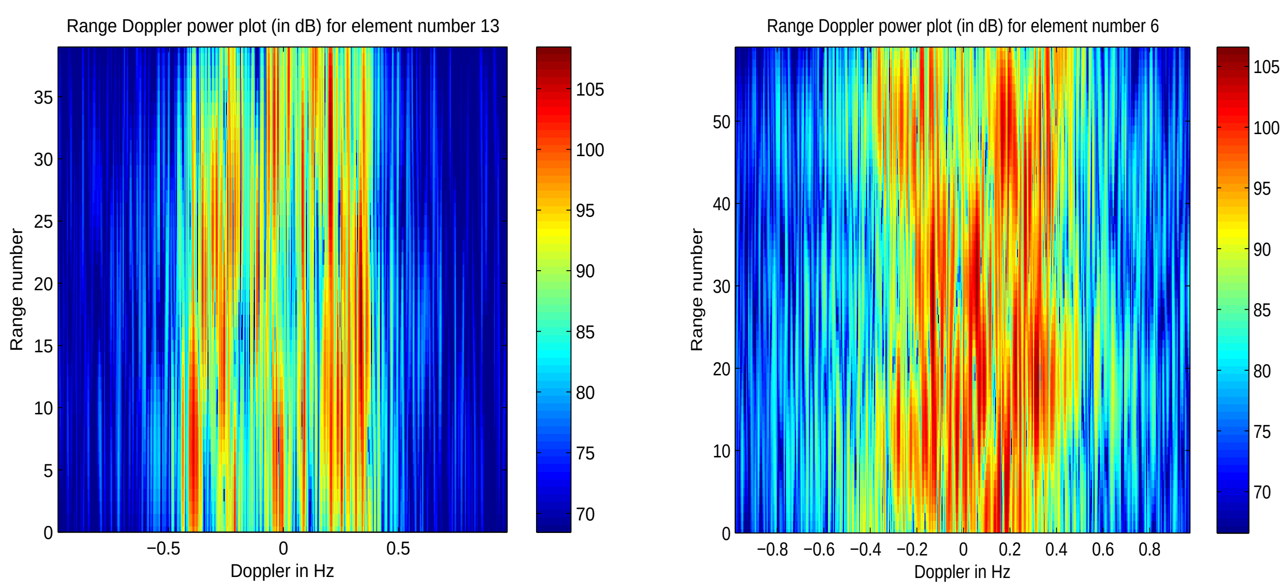

Figure 3.15: Doppler-range plot of the simulated signal (a) for antenna element 13 when $E(\varphi^2)$ is in the range of $(1 \sim 2) \times 10^2$ and (b) for antenna element 6 when $E(\varphi^2)$ is in the range of $(2 \sim 3) \times 10^2$.

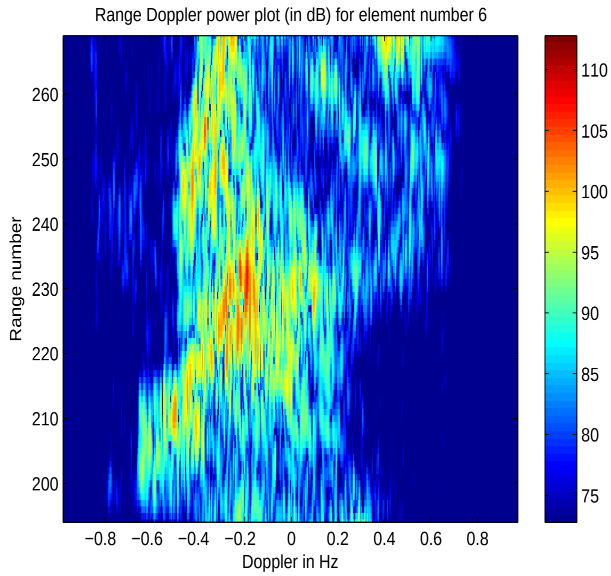

Figure 3.16: Doppler-range plot of the measured signal (a) for antenna element 6.

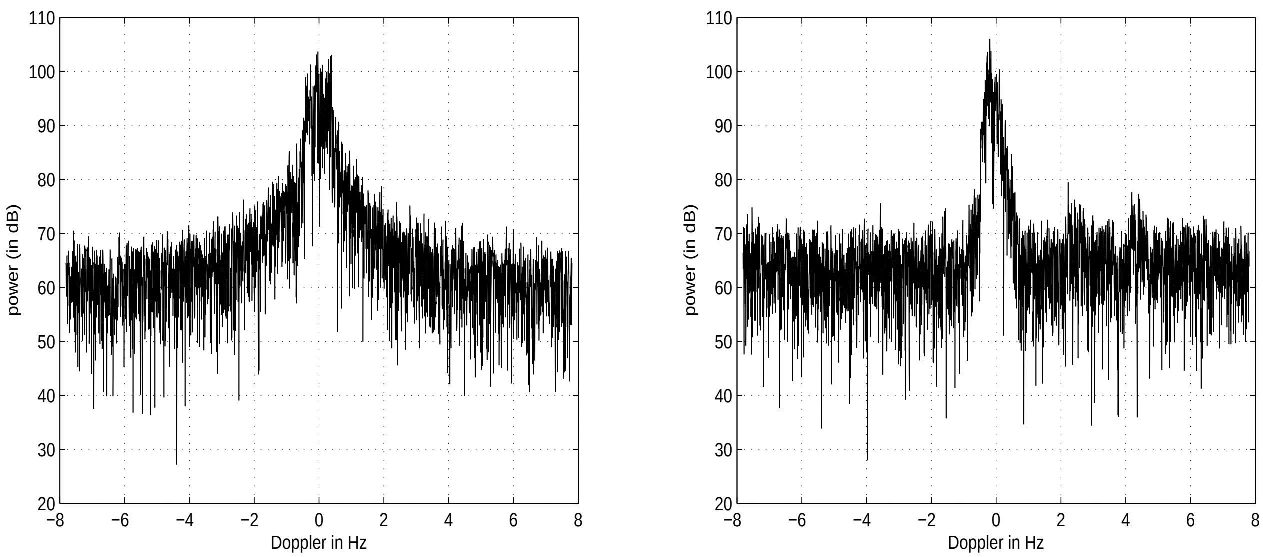

Figure 3.17: Doppler plot of the (a) simulated signal of range bin 12 and antenna element 6 and (b) measured signal of range bin 230 and antenna element 6 .

Chapter 4

Space-Time Adaptive Processing of Ionospheric Clutter

The central goal of this project is the development of practical space-time adaptive processing schemes for HFSWR radar systems. In a Chapter 2 we had reported on preliminary results of using spatial adaptive processing in conjunction with the data set provided by DRDC so far. In that report it was suggested that the most important issue with the available data is (a) the non-stationarity of the clutter and (b) the lack of secondary data to estimate the space-time covariance matrix. In this regard, of special interest are adaptive schemes that address clutter non-homogeneity and algorithms with fewer degrees of freedom. Examples of such algorithms are the Joint Domain Localized (JDL) algorithm [10], the direct data domain (D3) algorithm [48] and the combination of the two into the hybrid algorithm [7]. Other algorithms of interest are the parametric adaptive matched filter (PAMF) [49]. The hybrid and PAMF algorithms were designed specifically for non-homogeneous clutter. One should emphasize that this list is a starting point for our efforts in developing adaptive processing for HFSWR.

In this section we present the results of our preliminary work in applying the JDL algorithm to the HFSWR data set. However, we first revisit the results provided in Chapter 2 where the issue of oversampling was ignored. It was brought to our attention that the sampling rate used in the data set is $4\times$ the bandwidth of the transmitted signal, i.e., the data from one sample to the next is highly correlated. Here we present the results having accounted for this oversampling, but only using every fourth available range sample to estimate the required interference covariance matrices. As we will see, and as expected, this has a significant impact on the achievable performance.

Having reviewed algorithms already available in the literature, we present here the Fast Fully Adaptive (FFA) algorithm tailored for the specific characteristics of the Cape Race data set provided by DRDC. This data set is characterized by an extremely large number of degrees of freedom (4096 pulses, 16 channels) coupled with extremely limited training data (only approximately 80 range bins with ionospheric clutter). This algorithm is a *significant advance over previously available schemes* and represents the second major contribution of this project.

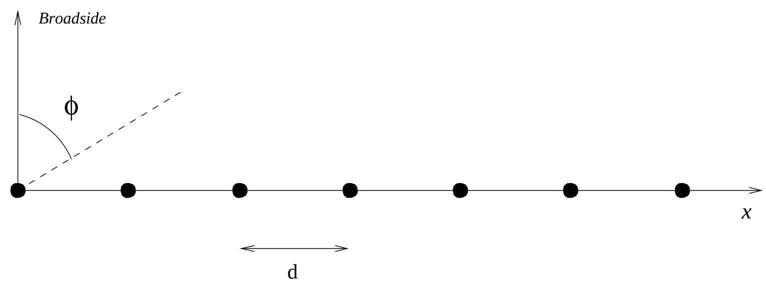

Figure 4.1: A linear array of point sensors .

4.1 Joint Domain Localized Processing

Consider an equispaced linear array of N isotropic, point sensors receiving an incident plane wave, as shown in Figure 4.1. Each channel receives M data samples corresponding to the M pulses in a CPI. Therefore, for each range bin, the received data is a length MN vector $\mathbf{x}$ whose entries numbered mN to $[(m+1)N-1]$ correspond to the returns at the N elements from pulse number $m, m = 0, 1, \ldots, M-1$. The data vector is a sum of the contributions from the external interference sources, the thermal noise and possibly a target, i.e.

$$\mathbf{x} = \xi\mathbf{s} + \mathbf{c} + \mathbf{n}, \tag{4.1}$$

where $\mathbf{s}$ represents the signal, $\mathbf{c}$ the vector of interference sources and $\mathbf{n}$ the thermal noise. ξ is the target amplitude and is zero in range cells without a target.

The term $\mathbf{s}$ in Eqn. (4.1) is the space-time steering vector corresponding to a target at angle ϕ_t and Doppler frequency f_t. This steering vector can be written in terms of a spatial steering vector $\mathbf{a}(\phi_t)$ and a temporal steering vector $\mathbf{b}(f_t)$ [44].

$$\begin{aligned}
\mathbf{s} &= \mathbf{b}(f_t) \otimes \mathbf{a}(\phi_t), && (4.2)\\
\mathbf{a}(\phi_t) &= \begin{bmatrix} 1 & e^{j2\pi f_s} & e^{j(2)2\pi f_s} & \ldots & e^{j(N-1)2\pi f_s} \end{bmatrix}^T, && (4.3)\\
\mathbf{b}(f_t) &= \begin{bmatrix} 1 & e^{j2\pi f_t/f_R} & e^{j(2)2\pi f_t/f_R} & \ldots & e^{j(M-1)2\pi f_t/f_R} \end{bmatrix}^T, && (4.4)\\
f_s &= \frac{d}{\lambda}\sin\phi_t, && (4.5)
\end{aligned}$$

where $\otimes$ represents the Kronecker product of two vectors, f_s the normalized spatial frequency, λ the wavelength of operation and f_R represents the pulse repetition frequency (PRF).

The spatial steering vector $\mathbf{a}(\phi)$ is the magnitude and phase taper *received* at the N elements of the array due to a calibrated far field source at angle ϕ. Due to electromagnetic reciprocity, to *transmit* in the direction ϕ the elements of the array must be excited with the conjugates of the steering vector, i.e. the conjugates of the steering vector *maximize the response in the direction* ϕ. Transformation of spatial data to the angle domain, at angle ϕ, therefore requires an inner product with the corresponding spatial steering vector. Similarly, the temporal steering $\mathbf{b}(f)$ vector corresponding to a Doppler frequency f is the magnitude and phase taper measured at an individual element for the M pulses in a CPI. An inner product with the corresponding temporal steering vector transforms time domain data to the Doppler domain. The angle-Doppler response of the data vector $\mathbf{x}$ at angle ϕ and Doppler f is therefore given by

$$\tilde{x}(\phi, f) = [\mathbf{b}(f) \otimes \mathbf{a}(\phi)]^H \mathbf{x}, \tag{4.6}$$

where the tilde ($\tilde{}$) above the scalar x signifies the transform domain. Choosing a set of spatial and temporal steering vectors generates a corresponding vector of angle-Doppler domain data.

Equations (4.2)-(4.4) show that the spatial and temporal steering vectors are identical to the Fourier coefficients. Based on this observation, the transformation to the angle-Doppler domain can be simplified under two conditions.

1. If a set of angles are chosen such that $(\frac{d}{\lambda}\sin\phi)$ is spaced by $1/N$ *and* a set of Doppler frequencies are chosen such that (f/f_R) is spaced by $1/M$, the transformation to the angle-Doppler domain is equivalent to the 2D DFT.

2. If the look angle ϕ_t corresponds to one these angles *and* the look Doppler f_t corresponds to one of these Dopplers, the 2-D DFT transforms the target data to a single point in the angle-Doppler domain, i.e. the signal is localized.

The second condition is based on the orthogonality of the DFT. This simplification is possible *only* in the case of the ideal array of Fig. 4.1.

The JDL algorithm as developed in [9] assumes both these conditions are met. A Local Processing Region (LPR), as shown in Fig. 4.2, is formed about the signal point and interference is suppressed in this region only. The LPR covers η_a angle bins and η_d Doppler bins. The choice of η_a and η_d is independent of N and M, i.e. the transformation to the angle-Doppler domain decouples the number of adaptive degrees of freedom from the size of the data cube. The covariance matrix corresponding to this LPR is estimated using secondary data from neighboring range cells. The adaptive weights are calculated by

$$\tilde{\mathbf{w}} = \tilde{\mathbf{R}}^{-1}\tilde{\mathbf{s}}, \tag{4.7}$$

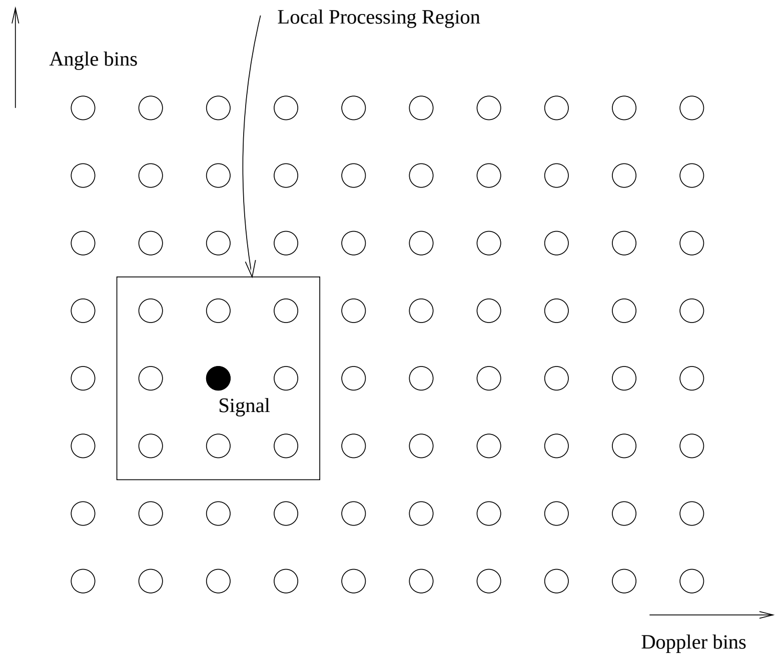

Figure 4.2: Localized processing regions in Joint Domain Localized processing.

where $\tilde{\mathbf{R}}$ is the estimated covariance matrix corresponding to the LPR of interest. The number of adaptive unknowns is equal to $\eta_a\eta_d$. Because of the fewer unknowns involved, the covariance matrix can be accurately estimated from a limited number of secondary data samples. $\tilde{\mathbf{s}}$ is the steering vector for the adaptive process. This vector must not be confused with either the spatial steering vector ($\mathbf{a}$) or the temporal steering vector ($\mathbf{b}$) of Eqns. (2.4)-(2.5). $\tilde{\mathbf{s}}$ is the space-time vector of equation (4.2) transformed to the angle-Doppler domain and is given by the length $\eta_a\eta_d$ vector

$$\tilde{\mathbf{s}} = [0,\ 0, \cdots,\ 0,\ 1,\ 0, \cdots,\ 0,\ 0]^T. \tag{4.8}$$

It must be emphasized that this simple form of the steering vector is valid only because it is the space-time steering vector transformed to the angle-Doppler domain using the *same transformation as used for the data*. The adaptive weights are used to find a statistic, such as the MSMI statistic, for detection by hypothesis testing.

The JDL algorithm described above can be generalized as follows: Fig. 4.2 shows that data from the LPR of interest is used for the adaptation process. Eqn. (4.6) indicates that the transformation from the space-time domain to the angle-Doppler domain is, in effect, an inner product with a space-time steering vector. This argument holds true for ideal linear arrays *and* physical arrays. Mathematically, the relevant transformation is therefore a pre-multiplication with a transformation matrix. For example, if the LPR covers 3 angle bins ($\phi_{-1}, \phi_0, \phi_1; \eta_a = 3$) and 3 Doppler bins

$(f_{-1}, f_0, f_1; \eta_d = 3)$ the transformation process is

$$\tilde{\mathbf{x}}_{\mathrm{LPR}} = \mathbf{T}^H \mathbf{x}. \tag{4.9}$$

Based on Eqn. (4.6), the transformation matrix $\mathbf{T}$ is the $(NM \times \eta_a \eta_d)$ matrix

$$\begin{aligned}\mathbf{T} \;=\; & [\mathbf{b}(f_{-1}) \otimes \mathbf{a}(\phi_{-1}); \;\; \mathbf{b}(f_0) \otimes \mathbf{a}(\phi_{-1}); \;\; \mathbf{b}(f_1) \otimes \mathbf{a}(\phi_{-1}); \\ & \mathbf{b}(f_{-1}) \otimes \mathbf{a}(\phi_0); \;\; \mathbf{b}(f_0) \otimes \mathbf{a}(\phi_0); \;\; \mathbf{b}(f_1) \otimes \mathbf{a}(\phi_0); \\ & \mathbf{b}(f_{-1}) \otimes \mathbf{a}(\phi_1); \;\; \mathbf{b}(f_0) \otimes \mathbf{a}(\phi_1); \;\; \mathbf{b}(f_1) \otimes \mathbf{a}(\phi_1)]\,, \end{aligned} \tag{4.10}$$

$$= [\mathbf{b}(f_{-1}); \;\; \mathbf{b}(f_0); \;\; \mathbf{b}(f_1)] \otimes [\mathbf{a}(\phi_{-1}); \;\; \mathbf{a}(\phi_0); \;\; \mathbf{a}(\phi_1)] \tag{4.11}$$

where the semi-colon (;) separates the columns of the matrix. The angle-Doppler steering vector used to solve for the adaptive weights in Eqn. (4.7) is the space-time steering vector $\mathbf{s}$ transformed to the angle-Doppler domain via the same transformation matrix $\mathbf{T}$, i.e.

$$\tilde{\mathbf{s}} = \mathbf{T}^H \mathbf{s}. \tag{4.12}$$

Note that the transformation matrix defined in Eqn. (4.11) is defined for the chosen frequencies and angles without any restrictions on their values. Further, no assumption is made as to the form of the spatial and temporal steering vectors.

4.1.1 Simulation Results

The preliminary analysis of the previous report indicated the presence of three distinct regions, a Bragg region (range cells 1-13 after removing range redundancy), a sea clutter region (ranges 14-44) and a region dominated by ionospheric clutter (ranges 45-63). Clearly these ranges are not exact and only chosen qualitatively. The first (dominated by Bragg-lines) and third (dominated by Ionospheric clutter) regions naturally lend themselves to the use of JDL, with limited sample support as the STAP algorithm of choice. To evaluate the performance of JDL in detecting weak (and ideal) targets injected into the regions dominated by Bragg-lines and Ionospheric clutter respectively, we used the same simulation setup as described in Chapter 2, where the targets shown in Table 4.1 were manually injected into the sample data-cube (after removing the redundant range samples).

As mentioned before, the data in the original set is oversampled by a factor of 4, i.e., a redundancy in range of a factor of 4. After removing this redundancy, we are left with only 68 range

Table 4.1: Target Characteristics

Target Number	Amplitude	Range Number	Angle	Doppler
1	5	7 (within Bragg region)	35^o	0.18Hz
2	5	54 (within Ionospheric clutter region)	35^o	0.18Hz

cells. For the region dominated by the Bragg-line we have, for each look range, only 11 range cells that correctly reflect the interference statistics in the Bragg line region and can be used as secondary range cells in estimating the covariance matrix. Similarly in the ionospheric clutter region only 17 independent ranges are available to estimate the clutter covariance matrix. Hence, in our results instead of selecting $\eta_a \eta_d$ ranges on either side of a specific look range as secondary range samples, we calculated the interference covariance matrix using all the ranges belonging to the region of interest (Bragg-line or Ionospheric region) except for the corresponding look range which was excluded from the covariance estimation procedure. Note that we did not use any spatial or temporal tapers for the purposes of this simulation, although the incorporation of such tapers into the transformation matrix could lead to improved performance.

Given the constraints on the available secondary data samples, one can only have 6 degrees of freedom ($\eta_a \eta_d < 6$) in the region dominated by Bragg lines; similarly we can have only 9 DOF in the ionospheric clutter region $(\eta_a \eta_d < 9)$. However, given the availability of redundant data, in our simulations we chose $(\eta_a \eta_d) =$ (3,3) , (3,5) ,and (3,7) for the Bragg-line dominated region , and $(\eta_a \eta_d) =$ (3,3) ,(3,5), and (3,7) for the Ionospheric clutter dominated region. Even though several of the selected $(\eta_a \eta_d)$ pairs do not theoretically lead to acceptable results (since their product is greater than the number of available independent training ranges), we chose them so as to verify this using simulation.

Angle Doppler Spacing

The work of [10] removed the spacing constraint between angle and Doppler bins that had been placed by the original JDL work of [9]. However, there is no available theory to determine an optimal spacing between angle or Doppler bins. The only recourse we have is to use simulations (another reason to implement a data model). The first set of results we present estimate the performance of the JDL algorithm as a function of angle and Doppler spacing.

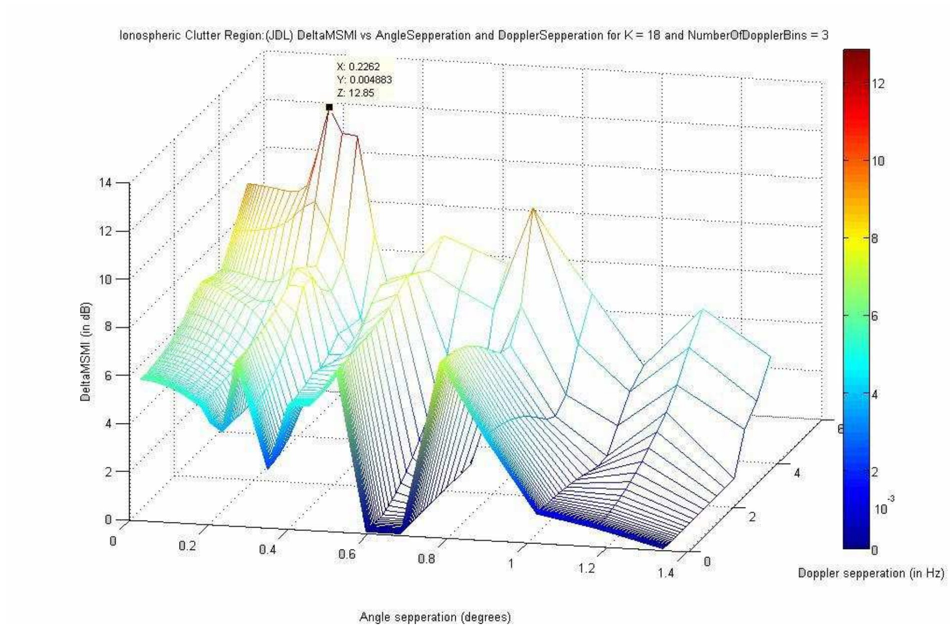

Figure 4.3: ΔMSMI versus angle and Doppler spacing ($\eta_a = \eta_d = 3$). Ionospheric clutter region.

Figure 4.3 plots (ΔMSMI), the difference between the MSMI statistic at the target range cell and the next largest MSMI statistic (i.e., the largest false alarm statistic), as a function of angle and Doppler spacing, for $\eta_a = 3$ and $\eta_d = 3$. ΔMSMI, therefore, measures how easy it is to distinguish the target from the background clutter. The figure illustrates that the JDL algorithm is fairly sensitive to angle and Doppler spacing with the difference in statistic varying by as much as $15dB$. There are some regions where the ΔMSMI is set to zero since its true value is negative, i.e., the target is buried in clutter. However, the majority of the choices of spacing provide a ΔMSMI larger than $6dB$. As we will see, when the target is in the Bragg region, the JDL algorithm appears to fail for most choices of angle and Doppler spacings.

Figure 4.4 recreates Figure 4.3 for the case where the target is within the Bragg lines. As can be seen, the target is almost never detected and the JDL method fails. Furthermore, the ΔMSMI is positive for only a few choices of angle and Doppler spacing.

Figure 4.5 and Figure 4.6 show that similar comments can be made for the case of $\eta_a = 3$ and $\eta_d = 5$. Interestingly, in this case the spacing that gives the greatest target discrimination is significantly smaller than in the case of $\eta_a = 3$ and $\eta_d = 3$. Obtaining an optimum spacing is one that will require many more data sets and simulation before a rule of thumb can be obtained.

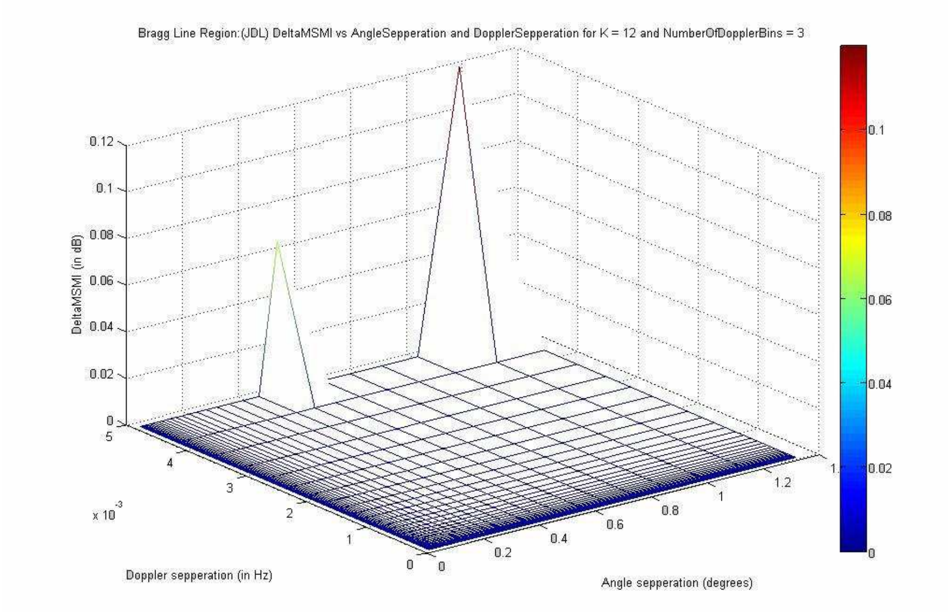

Figure 4.4: ΔMSMI versus angle and Doppler spacing ($\eta_a = \eta_d = 3$). Bragg region.

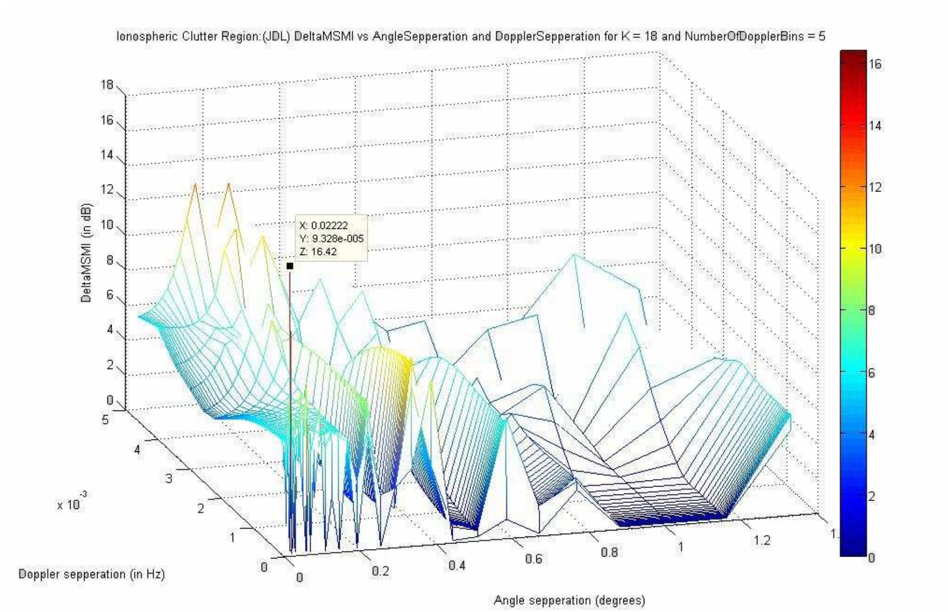

Figure 4.5: ΔMSMI versus angle and Doppler spacing ($\eta_a = 3, \eta_d = 5$). Ionospheric clutter region.

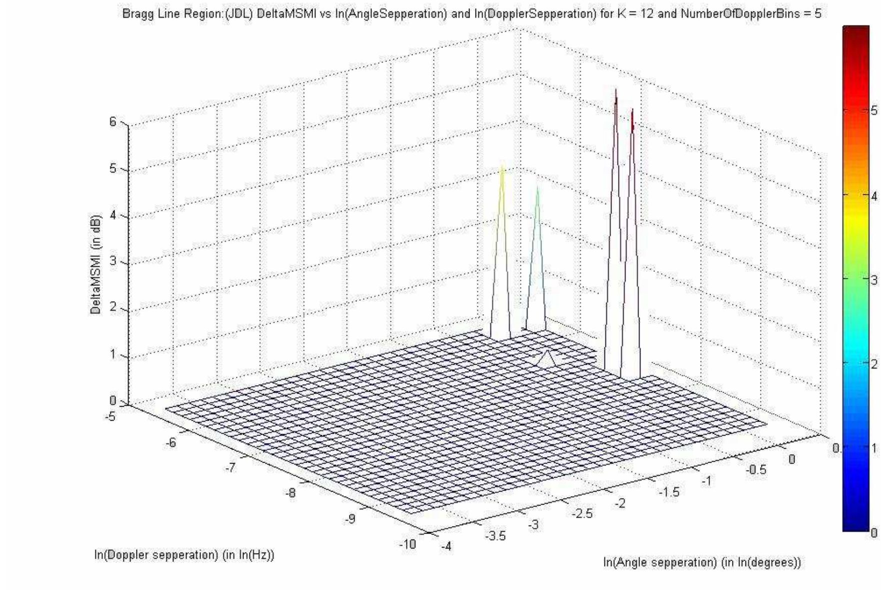

Figure 4.6: ΔMSMI versus angle and Doppler spacing ($\eta_a = 3, \eta_d = 5$). Bragg region.

Target Detection Using JDL

Figure 4.7 and Figure 4.8 plot the MSMI statistic versus range cell number for the optimal spacings found in the previous plots for the case of ($\eta_a = \eta_d = 3$). In the ionospheric clutter region, this configuration is adequate to clearly isolate the target from the surrounding clutter. For the amplitude given in Table 1, the MSMI statistic provides a discrimination of $13 + dB$.

Figure 4.8 plots the MSMI statistic when the same target is placed in the region dominated by the Bragg lines. In this case, the target cannot be identified with minimal discrimination between target and clutter. This is because only 12 range cells are available to estimate the 9×9 covariance matrix resulting in an extremely poor covariance estimate.

Figure 4.9 plots the MSMI statistic versus range with $\eta_a = 3$, $\eta_d = 7$ in the region dominated by the ionospheric clutter. The improved detection over Figure 4.7 is clearly visible. Note that in this example we used only 17 range cells to estimate the interference covariance matrix. The covariance matrix is therefore singular. However, here the matrix inverse is replaced by the min-norm solution to the under-determined system of equations available. The min-norm solution finds, in the family of possible solutions, the vector with minimum norm. *Note that this indicates that the rank of the interference is low and increasing the number of degrees of freedom improves target discrimination.* However, one should be cautious because the target is an ideal target and the adaptive process

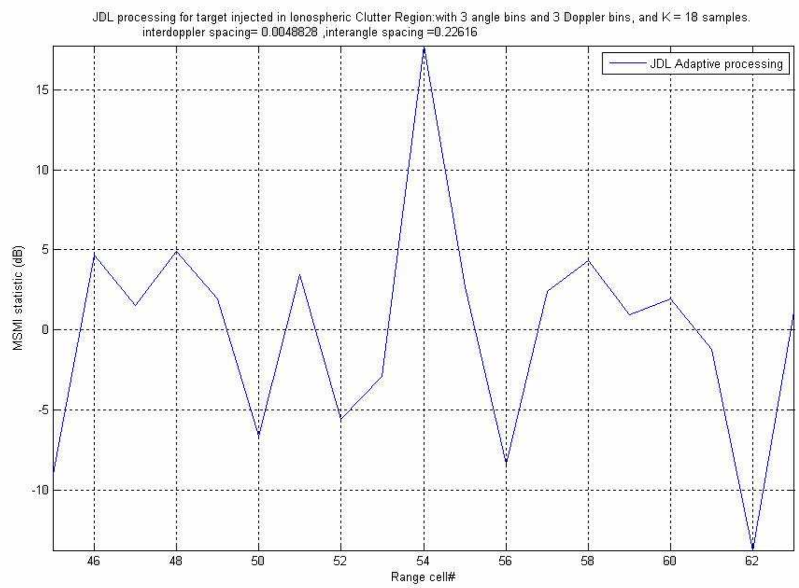

Figure 4.7: MSMI statistic (in dB) versus the range cell number for ($\eta_a = \eta_d = 3$). Ionospheric clutter region.

does not include any target mis-match.

Figure 4.10 plots the MSMI statistic versus range for the case of $\eta_a = 3$, $\eta_d = 7$, i.e., with 21 degrees of freedom, when the target is in the region dominated by the Bragg lines. Again the covariance matrix is singular and requires the min-norm solution. The low rank of the interference again allows for significant interference suppression with larger numbers of DOF. The target is clearly seen. This figure illustrates the potential of using JDL in the Bragg region as well.

We should mention that we have attempted to obtain MSMI results for the case where we use all available data without removing the redundancy. As with the earlier report, these plots provide highly optimistic results and are a matter of further investigation. For example, with $\eta_a = 3$ and $\eta_d = 7$ in the ionospheric region, when using all range cells we get the results as shown in Figure 4.11. The target discrimination is beyond our expectations. This may be due to,

1. the fact by using both spatial and Doppler degrees of freedom we are exploiting the very large number of coherent pulse intervals in addition to the 7 Doppler DOF (unlike when using adaptive processing in the spatial dimension only),

2. the large number of range cells ($17 \times 4 = 68$) used to estimate the 21×21 covariance matrix. The data, therefore, though correlated appears to have sufficient independence to provide

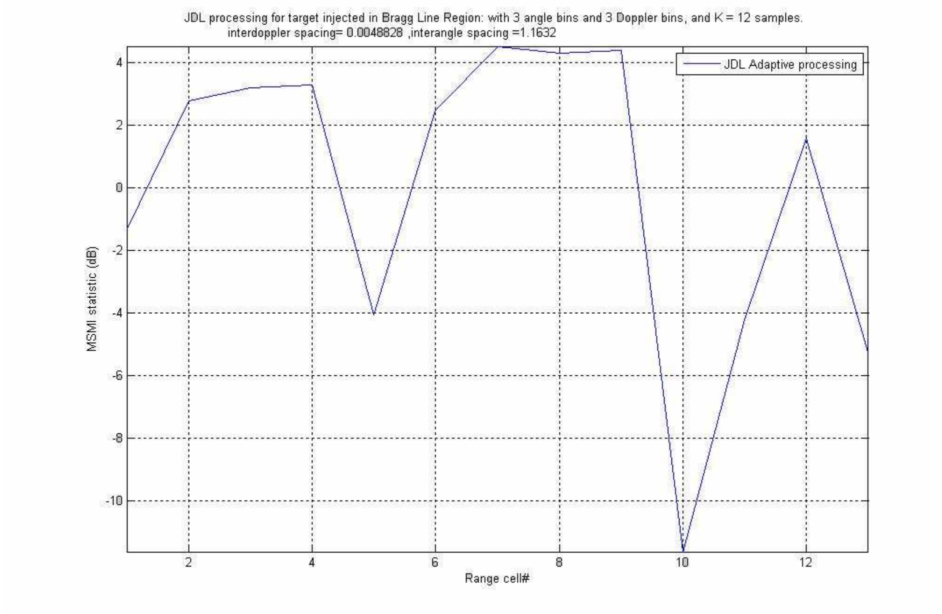

Figure 4.8: MSMI statistic (in dB) versus the range cell number for ($\eta_a = \eta_d = 3$). Bragg region.

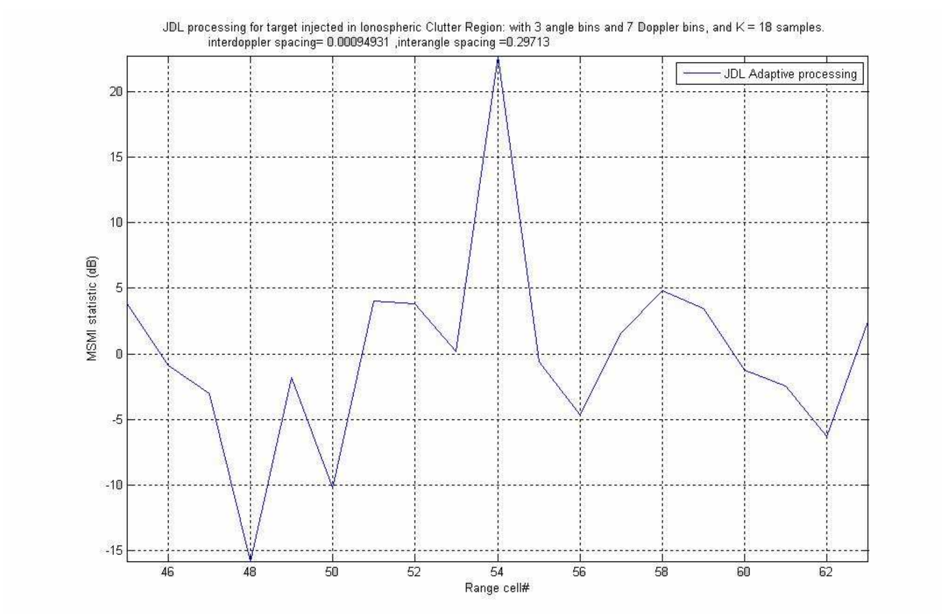

Figure 4.9: MSMI statistic (in dB) versus the range cell number for ($\eta_a = 3, \eta_d = 7$). Ionospheric clutter region.

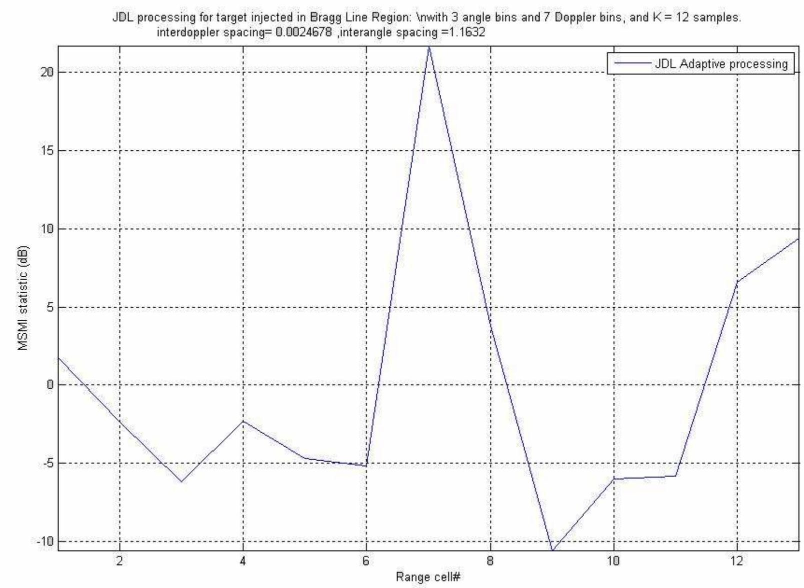

Figure 4.10: MSMI statistic (in dB) versus the range cell number for ($\eta_a = 3, \eta_d = 7$). Bragg region.

improved estimates of the angle-Doppler covariance matrix.

4.1.2 Discussion

When using ideal targets, the JDL algorithm provides excellent results in identifying targets that could not be identified by non-adaptive processing. In fact, JDL processing appears to perform better than the spatial-only case presented earlier. One essential drawback of JDL, though, is its heavy reliance on the homogeneity of the data used to estimate the interference covariance matrix. Unfortunately in practice it is seldom the case that the secondary data is homogeneous. The presence of discrete interferers for example can compromise the homogeneity of the secondary data and as a result lead to an inaccurate estimate of the interference covariance matrix, leading to a large degradation in the performance of JDL.

One must therefore use non-homogeneity detectors (NHD) to filter non-homogeneous range cells [6]. Alternatively, methods that do not rely on the computation of an estimate of the interference covariance matrix can be used to avoid the problem of inhomogeneous secondary data samples, altogether. Such methods include the direct data domain (D^3) [48] and the hybrid approach [7] which focus exclusive (the D^3 algorithm) or predominantly on the range cell of interest (the hy-

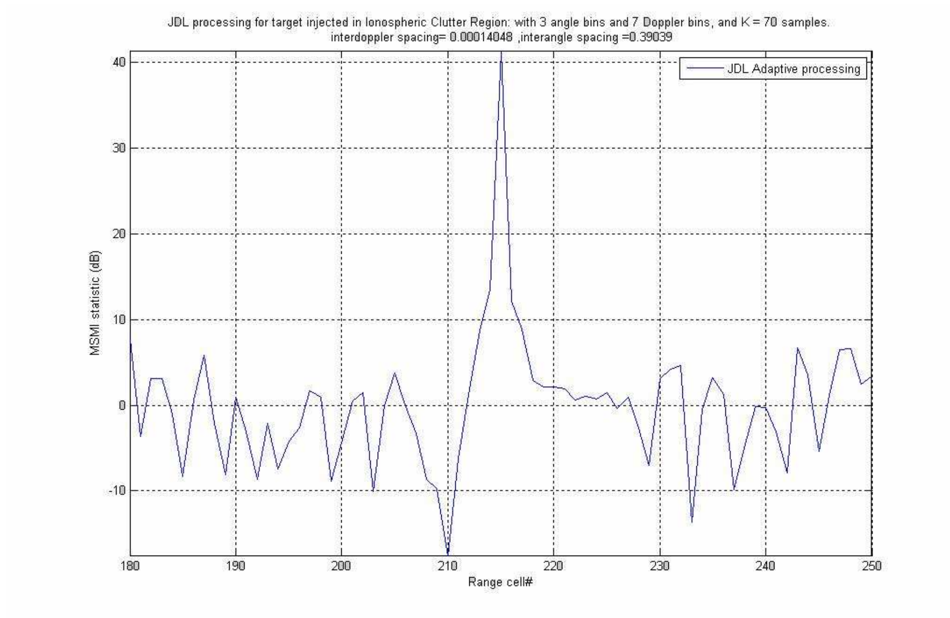

Figure 4.11: MSMI statistic (in dB) versus (in dB) versus the range cell number for ($\eta_a = 3, \eta_d = 7$). Using all range cells in ionospheric clutter region.

brid approach). In the next sections we investigate both these algorithms. It is also interesting to mention that JDL is not the only member of the low computation load family of STAP algorithms. Several other low computation methods have also been developed and address the issue of computation load in innovative and diverse methods. Some of the most popular low computation algorithms, other than JDL, include the parametric adaptive matched filter (PAMF) [49], and the multistage Weiner filter (MWF) [50]. In the next section we will investigate the relevance of the PAMF algorithm to our work.

Our results so far lead to a fundamental question: *how do we measure success effectively in an adaptive process, i.e., how do we compare algorithms?* There are two traditional approaches to estimating performance, (i) using the gain of the adapted pattern with the assumption that an array with higher gain has better performance and (ii) injecting targets and then measuring target discrimination as we have done above. This second approach is particularly popular when using measured data as we are doing in this project. However, there are serious issues with both these approaches.

The use of an adapted pattern to measure performance is valid only in homogeneous scenarios with relatively little structured interference. This is because without knowing a priori where the interference is located a pattern with lower array gain might be better in terms of interference suppression. A related concept, of measuring the output signal-to-interference-plus-noise ratio (SINR) is valid in homogeneous scenarios only. The output SINR is defined as

$$\mathrm{SINR} = \frac{\left|\mathbf{w}^H \mathbf{s}\right|^2}{\mathbf{w}^H \mathbf{R} \mathbf{w}}, \tag{4.13}$$

where $\mathbf{w}$ is the weight vector, $\mathbf{R}$ is the interference covariance matrix and $\mathbf{v}$ is the target space-time steering vector. Furthermore, the weight vector $\mathbf{w} = \mathbf{R}^{-1}\mathbf{v}$. However, the fundamental assumption is that the covariance matrix $\mathbf{R}$ is representative of the interference in the range cell under test. In STAP, this covariance matrix is obtained using secondary data, i.e., we are assuming the secondary data is representative of the statistics of the interference in the range cell under test. The other approach is to inject a target and determine the discrimination between the output statistic at the target range cell versus surrounding range cells. This is the approach taken above and has been taken in most of the research into the Multi-Channel Airborne Radar Measurements (MCARM) data set - see [10] for one example. However, this approach is only as useful as the model for a target is valid. In this report we have used a straightforward target model, but have ignored such issues as the redundancy in the data sampling process and hence the spread of the target as a function of range.

In summary, the JDL algorithm adaptive processes *angle-Doppler* data, i.e., after transformation from the space-time to the angle-Doppler domain. Adaptive processing focuses on a small localized processing region (LPR) within the angle-Doppler domain; specifically, the JDL algorithm adaptively processes η_a angle bins and η_d Doppler bins, i.e., only $\eta_a\eta_d$ adaptive weights are used. Considering that the usual values of η_a and η_d are between 3 and 5, the resulting computation load reduces from the solution of a $NM \times NM$ matrix to that of a $\eta_a\eta_d \times \eta_a\eta_d$ matrix.

The main drawback of using JDL is its inherent dependance on the homogeneity of the secondary data. Unfortunately the highly nonhomogeneous and non-stationary nature of the ionospheric clutter as well as the limited availability of secondary data are all factors that are capable of seriously degrading the performance of JDL in the ionospheric clutter region.

In the following sections, we use the hybrid algorithm to achieve suppression of both nonhomogeneous and homogeneous components of the clutter. The hybrid algorithm builds on the JDL algorithm using an *adaptive* transform from the space-time to the angle-Doppler domain. Specifically, the adaptive transform uses direct data domain (D^3) processing; adaptive processing without requiring secondary data. D^3 processing was first developed in [48] for the spatial-only case and then extended to space-time processing in [7]. The latest work in this area [51] develops an alternative approach that is significantly more stable computationally.

The D^3 algorithm processes each range cell individually and is thus immune to any uncorrelated interference present at a certain range cell. However, since the D^3 algorithm completely ignores any statistical information that might be derived from the secondary data about the correlated part of the interference present in the target range, it is not as effective as the JDL algorithm in suppressing correlated interference. This deficiency is accounted for in the *hybrid* algorithm [7] which combines the advantages of both the D^3 and JDL algorithms to suppress both coherent and incoherent interference present in the target range. We will describe the hybrid algorithm in a subsequent section.

The hybrid algorithm has some significant advantages in that it can address both homogeneous and non-homogeneous components of clutter. However, it does have some drawbacks. First, the hybrid algorithm is fairly computationally expensive. Also, in the context of ionospheric clutter, the clutter non-homogeneities are not localized which is the ideal scenario for the D^3 algorithm.

Another powerful algorithm that was designed to show both improved computational speed and high accuracy as well as a certain degree of robustness towards non-homogeneous data, is the parametric adaptive matched filter (PAMF) algorithm [49]. The PAMF approach uses linear filter theory to estimate the inverse of the covariance matrix in a computationally efficient manner and significantly reduced required sample support to obtain the output statistic. The only drawback of the PAMF approach is that there is no clear way to integrate D^3 processing for non-homogeneous clutter.

The second problem in the previous report is one of modeling the target. In the previous work, the JDL algorithm was used to detect a single *point* target injected into a single range bin. This is clearly a idealized situation; in the real world, a target is distributed over range bins. In this report we present results of using a real (measured) target signal extracted from a noise-limited data set provided by DRDC.

In the next sections, after describing the D^3, hybrid, and PAMF algorithms, we will present the simulation results of applying these algorithms to both ideal and real targets int the Bragg and ionospheric clutter region. We will also follow up on JDL by presenting simulation results using JDL on real targets.

4.2 The Direct Data Domain Algorithm

The D^3 algorithm, developed in [7] and improved upon in [51], is a purely non-statistical algorithm which does all its processing using only the current look range without relying on the neighboring ranges to extract an estimate of the error covariance matrix. As a result the D^3 algorithm is immune to both clutter non-homogeneities in the secondary data and target-like, discrete, interference sources within the primary range cell. The discrete interference may be occupy multiple angle and Doppler bins. This scenario is more relevant to us since the ionospheric clutter, with its highly nonhomogeneous nature, may be characterized as a source of high power discrete interference spread over numerous range cells leading to a contamination of the homogeneity of the secondary data.

We begin with a brief description of how the improved D^3 algorithm of [51] works. Assuming the usual N element, M pulse scenario we form the $N \times M$ data matrix $\mathbf{X}$ at range cell r:

$$\mathbf{X} = \xi\mathbf{V} + \mathbf{C} + \mathbf{N}, \tag{4.14}$$

$$\mathbf{V} = \mathbf{a}(\varphi_t) \otimes \mathbf{b}^T(f_t), \tag{4.15}$$

$$\mathbf{a}(\varphi_t) = \begin{bmatrix} 1 & z_s & \cdots & z_s^{(N-1)} \end{bmatrix}^T, \tag{4.16}$$

$$\mathbf{b}(f_t) = \begin{bmatrix} 1 & z_t & \cdots & z_t^{(M-1)} \end{bmatrix}^T, \tag{4.17}$$

$$z_s = e^{i2\pi(d/\lambda)\sin(\varphi_t)}, \tag{4.18}$$

$$z_t = e^{i2\pi(f_t/f_R)}, \tag{4.19}$$

where ξ is the target amplitude, $\mathbf{a}(\varphi_t)$ and $\mathbf{b}(f_t)$ are the target spatial and temporal steering vectors respectively, at azimuth φ_t and Doppler f_t , and $\mathbf{C}$ and $\mathbf{N}$ are the clutter and noise space-time matrices respectively.

Next we form the temporal residual matrix A_t as follows,

$$\mathbf{A}_t = \mathbf{X}(0 : M-2, 0 : N-1) - z_t^{-1}\mathbf{X}(1 : M-1, 0 : N-1) \tag{4.20}$$

where we used MATLAB® notation to specify the two submatrices used in the above matrix difference. We can therefore write the $(i,j)_{th}$ term of the matrix $\mathbf{A}_t$ as,

$$\mathbf{A}_t(i,j) = \mathbf{X}(i,j) - z_t^{-1}\mathbf{X}(i,j+1), \qquad i = 0,..,N-1 \; j = 1,...,M-2 \tag{4.21}$$

If $\mathbf{X}$ were to contain a target, then the above procedure yields a residual matrix $\mathbf{A}$ free from any target terms.Ideally the entries of matrix $\mathbf{A}_t$ carry interference only terms, but due to possible beam mis-match, some negligibly small residual target information may still be present in the entries of $\mathbf{A}_t$.

We will next make use of the following scalar terms in an attempt to null the discrete interference,

$$G_{wt} = \left|\mathbf{b}^H_{(0:M-2)}\mathbf{w}_t\right|^2 \tag{4.22}$$

$$I_{wt} = \|\mathbf{A}^*_t w_t\|^2 \tag{4.23}$$

$$\mathrm{SINR}_{residual} \propto \frac{G_{wt}}{I_{wt}} = \frac{\mathbf{w}^H_t\mathbf{b}_{(0:M-2)}\mathbf{b}^H_{(0:M-2)}\mathbf{w}_t}{w^H_t\mathbf{A}^T_t\mathbf{A}^*_t w_t} \tag{4.24}$$

where G_{wt} represents the target signal power after temporal filtering with the weight vector $\mathbf{w}_t$, and I_{wt} represents the residual interference power after temporal filtering. As a result the residual SINR can be defined as the ratio of these two terms, and our task is to select an optimal temporal filter $\mathbf{w}_t$ that maximizes the above SINR.

$$\mathbf{w}_{t_{opt}} = \arg\max_{\{\mathbf{w}_t\}}(\mathrm{SINR}_{residual}) \tag{4.25}$$

The solution to the above optimization problem can be shown to be,

$$\mathbf{w}_{t_{opt}} = \left(\mathbf{A}^T_t\mathbf{A}^*_t\right)^{-1}\mathbf{b}_{(0:M-2)} \tag{4.26}$$

if $\left(\mathbf{A}^T_t\mathbf{A}^*_t\right)^{-1}$ exists. If this matrix inverse does not exist, the solution is the eigenvector corresponding to the large generalized eigenvalue of the matrix pair $\left(\mathbf{A}^T_t\mathbf{A}^*_t, \mathbf{b}_{(0:M-2)}\mathbf{b}^H_{(0:M-2)}\right)$.

Optimal D^3 spatial weights can be obtained in a similar manner. Define $\mathbf{A}_s$ as the residual spatial interference matrix,

$$\mathbf{A}_s = \left(\mathbf{X}(0:M-1, 0:N-2) - z_t^{-1}\mathbf{X}(0:M-1, 1:N-1)\right)^T \tag{4.27}$$

whose $(i,j)_{th}$ term is given by,

$$\mathbf{A}_s(i,j) = \mathbf{X}(j,i) - z_t^{-1}\mathbf{X}(j+1,i) \tag{4.28}$$

Next define the target signal power, residual interference power, and SINR after spatial filtering as,

$$G_{ws} = \left|\mathbf{a}^H_{(0:N-2)}\mathbf{w}_s\right|^2 \tag{4.29}$$

$$I_{ws} = \|\mathbf{A}^*_s\mathbf{w}_s\|^2 \tag{4.30}$$

$$SINR_{residual} \propto \frac{G_{ws}}{I_{ws}} = \frac{\mathbf{w}^H_s\mathbf{a}_{(0:N-2)}\mathbf{a}^H_{(0:N-2)}\mathbf{w}_s}{\mathbf{w}^H_s\mathbf{A}^T_s\mathbf{A}^*_s\mathbf{w}_s} \tag{4.31}$$

We can therefore obtain the optimal spatial weights by maximizing the above SINR which yields,

$$\mathbf{w}_{s_{opt}} = \left(\mathbf{A}^T_s\mathbf{A}^*_s\right)^{-1}\mathbf{a}_{(0:N-2)}. \tag{4.32}$$

We then obtain the optimal spatio-temporal set of weights, $\mathbf{w}$, as

$$\mathbf{w} = \begin{bmatrix} \mathbf{w}_{t_{opt}} \\ 0 \end{bmatrix} \otimes \begin{bmatrix} \mathbf{w}_{s_{opt}} \\ 0 \end{bmatrix}. \tag{4.33}$$

The 0 terms represent the lost spatial and lost temporal degrees of freedom.

Because the algorithm does not require any secondary data, the D^3 is capable of suppressing any uncorrelated interference present in the target range. However since D^3 is a nonstatistical algorithm it suffers from poor performance when correlated (homogeneous) interference is present in the target's range. One other disadvantage of the D^3 algorithm is that it requires the computation of the inverse of an $(M-1) \times (M-1)$ matrix which can be quite a daunting task for large number of pulses. In the DRDC data sets, $M = 4096$, making the matrix in question singular. Even finding the generalized eigenvalues becomes difficult since the algorithms involved become unstable.

In the following section we will describe the hybrid algorithm which uses D^3 as a first stage to eliminate (null out) discrete interference sources contaminating the target range, then uses the JDL algorithm on this 'purified' data to suppress the correlated interference.

4.3 The Hybrid Algorithm

The hybrid algorithm was developed in [7] for airborne radar applications. It is a two stage algorithm whose building blocks are the D^3 and JDL algorithms. The hybrid algorithm can be summarized in the following steps:

1. Form a Localized Processing Region (LPR) by choosing a set of η_a angle bins centered at the look angle, and η_d Doppler bins centered at the look Doppler.

2. For each angle-Doppler bin,(ϕ_{-i}, f_{-j}) within the LPR form the corresponding space-time steering vector and use the D^3 algorithm to obtain the adaptive weight vector $w(\phi_{-i}, f_{-j})$ that transforms the look range from the space-time domain to the angle-Doppler.

3. After looping over all the LPR bins form the adaptive transformation matrix $\mathbf{T}_{D^3}$. For example, for 3 angle and 3 Doppler bins $\mathbf{T}_{D^3}$ is given by,

$$\begin{aligned}\mathbf{T}_{D^3} = [\mathbf{w}(\phi_{-1}, f_{-1}) \quad & \mathbf{w}(\phi_0, f_{-1}) \quad \mathbf{w}(\phi_1, f_{-1}) \\ \mathbf{w}(\phi_{-1}, f_0) \quad & \mathbf{w}(\phi_0, f_0) \quad \mathbf{w}(\phi_1, f_0) \\ \mathbf{w}(\phi_{-1}, f_1) \quad & \mathbf{w}(\phi_0, f_1) \quad \mathbf{w}(\phi_1, f_1)]\end{aligned} \tag{4.34}$$

4. Transform the target range space-time vector and all the secondary ranges to the angle-Doppler domain via the transformation matrix $\mathbf{T}_{D^3}$.

5. Apply the JDL algorithm to the transformed domain to obtain the optimal weight vector given by,

$$\mathbf{w}_{hybrid} = \widehat{\mathbf{R}}^{-1}\widehat{\mathbf{v}} \tag{4.35}$$

6. Compute the CFAR MSMI test statistic as follows,

$$MSMI = \frac{\left|\mathbf{w}_{hybrid}^{H}\overset{\wedge}{\mathbf{x}}\right|^2}{\mathbf{w}_{hybrid}^{H}\overset{\wedge}{\mathbf{v}}} \tag{4.36}$$

Thus the hybrid algorithm suppresses any discrete interference that might be present at the target range in its first, D^3 stage, effectively transforming the datacube to the angle-Doppler domain. It then nulls the correlated interference by computing a weight vector derived from the estimate of the error covariance matrix in the transformed domain. The main drawback of the hybrid algorithm is its large computational time, since it has to apply the D^3 algorithm for each of the $\eta_a\eta_d$ angle-Doppler bins of the LPR.

4.4 The Parametric Adaptive Matched Filtering Algorithm

The PAMF algorithm was developed in [49]. The primary idea behind this algorithm is the use of linear estimation theory to obtain an estimate of the inverse of the error covariance matrix which can be computed much more rapidly than in the conventional AMF method. PAMF is based on the block-LDL decomposition of the covariance matrix, $\mathbf{R}$, where the non-zero block elements of the lower triangular block matrix, $\mathbf{L}$, resulting from the decomposition, corresponding to each block row p, are the coefficients of a multichannel autoregressive process of order p, whose error covariance matrix is the p-th block matrix of the block diagonal matrix $\mathbf{D}$ resulting from the LDL decomposition of $\mathbf{R}$. Since $\mathbf{R}$ is not known *a priori* the coefficients of $\mathbf{L}$ and $\mathbf{D}$ must be approximated by assuming a p-th order multichannel AR process to be the underlying process and using an appropriate parameter estimation algorithm to estimate the coefficients of this multichannel AR(P) process. An excellent discussion of multichannel AR processes and several corresponding parameter estimation algorithms are readily available in [52].

We will now present a brief description of the main concepts behind the PAMF method. Let the localized target steering vector at azimuth α_t and Doppler f_t be given by the $NM \times 1$ space-time steering vector $\mathbf{v}$, and the space-time snapshot of the datacube returns at the target range be given by the $NM \times 1$ vector $\mathbf{x}$. Adopting the same setup as previously described, the adaptive matched filter solution leads to the evaluation of the following MSMI CFAR statistic,

$$\frac{\left|\mathbf{v}^H\widetilde{\mathbf{R}}^{-1}\mathbf{x}\right|^2}{\mathbf{v}^H\widetilde{\mathbf{R}}^{-1}\mathbf{v}} \tag{4.37}$$

The computation of the estimate $\widetilde{\mathbf{R}}$ of the error covariance matrix, and its inversion, requires large sample support as well as an impractical computational load. To overcome this the PAMF attempts to estimate this inverse using a multichannel AR process of an appropriate order. Since $\widetilde{\mathbf{R}}$ is block Hermitian then there exists a unique LDL block decomposition of this matrix given by

$$\widetilde{\mathbf{R}} = \mathbf{A}\mathbf{D}\mathbf{A}^H \tag{4.38}$$

where $\mathbf{A}$ is a lower triangular block matrix and $\mathbf{D}$ is a block diagonal matrix. Assuming $\widetilde{\mathbf{R}}$ to be invertible, we can take the inverse of both sides of the above equation to yield,

$$\widetilde{\mathbf{R}}^{-1} = \left(\mathbf{A}^H\right)^{-1}\mathbf{D}^{-1}\mathbf{A}^{-1} \tag{4.39}$$

where the matrices $\mathbf{A}^{-1}$ and $\mathbf{D}$ can be written as,

$$\mathbf{A}^{-1} = \begin{bmatrix} \mathbf{I}_N & \mathbf{0}_N & \mathbf{0}_N & \cdots & \mathbf{0}_N & \mathbf{0}_N \\ \mathbf{A}_1^H(1) & \mathbf{I}_N & \mathbf{0}_N & \cdots & \mathbf{0}_N & \mathbf{0}_N \\ \mathbf{A}_2^H(2) & \mathbf{A}_2^H(1) & \mathbf{I}_N & \cdots & \mathbf{0}_N & \mathbf{0}_N \\ \vdots & \vdots & \vdots & \ddots & \vdots & \vdots \\ \mathbf{A}_{M-2}^H(M-2) & \mathbf{A}_{M-2}^H(M-3) & \mathbf{A}_{M-2}^H(M-4) & \cdots & \mathbf{I}_N & \mathbf{0}_N \\ \mathbf{A}_{M-1}^H(M-1) & \mathbf{A}_{M-1}^H(M-2) & \mathbf{A}_{M-1}^H(M-3) & \cdots & \mathbf{A}_{M-1}^H(1) & \mathbf{I}_N \end{bmatrix}, \tag{4.40}$$

$$\mathbf{D} = \begin{bmatrix} \mathbf{D}_0 & \mathbf{0} & \cdots & \mathbf{0} \\ \mathbf{0} & \mathbf{D}_1 & \cdots & \vdots \\ \vdots & \ddots & \ddots & \mathbf{0} \\ \mathbf{0} & \cdots & \mathbf{0} & \mathbf{D}_(M-1) \end{bmatrix}, \tag{4.41}$$

where the $N \times N$ submatrix $\mathbf{A}_i^H(j)$ is the i'th row and (j-i)'th column block elements of matrix $\mathbf{A}$ $(i, j = 0, \cdots, M-1)$, and are not characterized by any particular structure. Note that the block diagonal matrices $\mathbf{A}_i^H(0)$ are equal to the $N \times N$ identity matrix. Also the $N \times N$ submatrices $\mathbf{D}_i$, $i = 0, \cdots, M-1$), are the block diagonal elements of the matrix $\mathbf{D}$. It was shown in [49] that the set of matrices $\{\mathbf{A}_m^H(m), \mathbf{A}_m^H(m-1), \cdots, \mathbf{A}_m^H(1)\}$ for $m = 0, \cdots, M-1$, are the matrix coefficients of a m-th order multichannel forward linear predictor for a vector process $\{\mathbf{x}(m)\}$ whose covariance matrix of the m-th order prediction error vector is given by the m-th block diagonal element $\mathbf{D}_i$. This can be written as,

$$\begin{aligned}
&\hat{\mathbf{x}}_m(m) = -\sum_{k=1}^{m} \mathbf{A}_m^H(k)\mathbf{x}(m-k) \qquad \{m = 0, \cdots, M-1\} \\
&\varepsilon_m(m) = \mathbf{x}(m) - \widehat{\mathbf{x}_m}(m) = \sum_{k=0}^{m} \mathbf{A}_m^H(k)\mathbf{x}(m-k) \\
&E[\varepsilon_m(m)] = \mathbf{D}_m \\
&\{\mathbf{x}(m)\} = \begin{bmatrix} \ldots & \mathbf{x}(0) & \mathbf{x}(1) & \ldots & \mathbf{x}(m) & \cdots & \mathbf{x}(M-1) & \ldots \end{bmatrix}
\end{aligned} \tag{4.42}$$

In the above equation the vector term ϵ is the error vector of the AR(m) process. As can be seen from the above equation this error vector is the output of the m-th order multichannel moving average process (MA(m)) whose coefficients are the matrix coefficients of the corresponding multichannel AR(m) process, and whose input is the vector process $\{\mathbf{x}(m)\}$.

So far our entire discussion is general and applies to any invertible, block hermitian, matrix $\mathbf{R}$. The reason we chose $\mathbf{x}$ to denote the vector process will be clear after we plug in the LDL representation of $\widetilde{\mathbf{R}}$ into the expression for the MSMI statistic.

$$\begin{aligned}
\Lambda_{MF} &= \frac{\left|(\mathbf{D}^{-1/2}\mathbf{A}^{-1}\mathbf{v})^H(\mathbf{D}^{-1/2}\mathbf{A}^{-1}\mathbf{x})\right|^2}{(\mathbf{D}^{-1/2}\mathbf{A}^{-1}\mathbf{v})^H(\mathbf{D}^{-1/2}\mathbf{A}^{-1}\mathbf{v})} \\
&= \frac{\left|(\mathbf{D}^{-1/2}\mathbf{u})^H(\mathbf{D}^{-1/2}\varepsilon)\right|^2}{(\mathbf{D}^{-1/2}\mathbf{u})^H(\mathbf{D}^{-1/2}\mathbf{u})} = \frac{\left|\mathbf{s}^H\mathbf{r}\right|^2}{\mathbf{s}^H\mathbf{s}}
\end{aligned} \tag{4.43}$$

$$\mathbf{u} = \mathbf{A}^{-1}\mathbf{v} \tag{4.44}$$

$$\varepsilon = \mathbf{A}^{-1}\mathbf{x} \tag{4.45}$$

$$\mathbf{s} = \mathbf{D}^{-1/2}\mathbf{u} \tag{4.46}$$

$$\mathbf{r} = \mathbf{D}^{-1/2}\varepsilon \tag{4.47}$$

We can write the vectors $\mathbf{x}$ and ϵ as,

$$\mathbf{x}_{MN\times 1} = \begin{bmatrix} \mathbf{x}^T(0) & \mathbf{x}^T(1) & \cdots & \mathbf{x}^T(M-1) \end{bmatrix}^T \tag{4.48}$$

$$\varepsilon_{MN\times 1} = \begin{bmatrix} \varepsilon^T(0) & \varepsilon^T(1) & \cdots & \varepsilon^T(M-1) \end{bmatrix}^T \tag{4.49}$$

where $\mathbf{x}(m)$ is the $N\times 1$ spatial steering vector at the m-th pulse. As a result we can use Eqn. (4.43) and Eqn. (4.49) to write $\varepsilon(m)$ as,

$$\varepsilon_{N\times 1}(m) = \sum_{k=0}^{m} \mathbf{A}_m^H(k)\mathbf{x}(m-k) \qquad \{m = 0, \cdots, M-1\} \tag{4.50}$$

This justifies why we chose $\mathbf{x}$ to denote the vector process in our general formulation. Equation (4.50) describes a multichannel MA(m) process with output error vector $\epsilon(m)$ and input vector sequence $\mathbf{x}(m)$ with coefficients $\{\mathbf{A}_m^H(m), \mathbf{A}_m^H(m-1), \cdots, \mathbf{A}_m^H(1)\}$ for $m = 0, \cdots, M-1$. Since the coefficients of this MA(m) process are the block elements of the m-th row of the inverse of the triangular block matrix $\mathbf{A}$ resulting from the LDL decomposition of $\mathbf{R}$, then it follows from our previous discussion that the covariance of the m-th order prediction error vector, associated with the m-th set of matrix coefficients, has a covariance given by the m-th diagonal matrix block ,$\mathbf{D}_m$. Also since this is a MA process, the error vectors $\varepsilon(m) m = 0, \cdots, M-1$ are uncorrelated in pairs [52]. This can be written as,

$$E\left[\varepsilon(m)\varepsilon^H(m)\right] = \mathbf{D}_m \qquad \{m = 0, \cdots, M-1\} \tag{4.51}$$

$$E\left[\varepsilon(m)\varepsilon^H(n)\right] = \mathbf{0}_m \qquad \{m \neq n\} \tag{4.52}$$

$$\Rightarrow E\left[\varepsilon\varepsilon^H\right] = \mathbf{D} \tag{4.53}$$

Thus we can see that the outputs of the $M-1$ MA processes are temporally white. This fact is useful when we attempt to compute the covariance of the m-th block vector, $\mathbf{r}(m)$, of the vector $\mathbf{r}$. Therefore we have,

$$\begin{aligned} \mathbf{r}(m) &= \mathbf{D}_m^{-1/2}\varepsilon(m) \\ &= \mathbf{D}_m^{-1/2}\sum_{k=0}^{m} \mathbf{A}_m^H(k)\mathbf{x}(m-k) \qquad \{m = 0, \cdots, M-1\} \end{aligned} \tag{4.54}$$

and,

$$E\left[\mathbf{r}(m)\mathbf{r}^H(m)\right] = \mathbf{D}_m^{-1/2}\mathbf{D}_m\mathbf{D}_m^{-1/2} = \mathbf{I}_M \tag{4.55}$$

$$E\left[\mathbf{r}(m)\mathbf{r}^H(n)\right] = \mathbf{D}_m^{-1/2}E\left[\varepsilon(m)\varepsilon^H(n)\right]\mathbf{D}_n^{-1/2} = \mathbf{0}_M \tag{4.56}$$

$$\Rightarrow E\left[\mathbf{r}\mathbf{r}^H\right] = \mathbf{I}_{MN} \tag{4.57}$$

Thus the vectors $\mathbf{r}(m)$ are both temporally and spatially white. Thus the coefficient matrix $\mathbf{A}$ acts as a temporal whitening filter which is followed by a spatial whitening filter embodied in the matrix D. The same expressions can be obtained for the vectors $\mathbf{u}$ and $\mathbf{s}$.

In order to bypass the computation of the inverse of an estimate of $\mathbf{R}$ it suffices to estimate the coefficient matrix $\mathbf{A}^{-1}$ and residual covariance matrix $\mathbf{D}$, and use them in (Eqn. (4.43)) to directly compute the MSMI criterion. The first step to achieving this is to select an appropriate AR order that accurately portrays the underlying statistics. After the order, P, has been selected we can rewrite the PAMF detection statistic as,

$$\begin{aligned}
\Lambda_{PAMF} &= \frac{\left|\sum\limits_{m=0}^{M-P-1} \mathbf{s}^H(m)\mathbf{r}(m)\right|^2}{\sum\limits_{m=0}^{M-P-1} \mathbf{s}^H(m)s(m)} \\
\varepsilon_{N\times 1}(m) &= \sum_{k=0}^{P} \mathbf{A}^H(k)\mathbf{x}(m-k+P) \qquad \{m = 0, \cdots, M-P-1\} \\
r(m) &= \mathbf{D}_P^{-1/2} \sum_{k=0}^{P} \mathbf{A}^H(k)\mathbf{x}(m-k+P) \qquad \{m = 0, \cdots, M-P-1\}
\end{aligned} \tag{4.58}$$

where the following modifications were administered to the definitions of ϵ and $\mathbf{r}$ in order to obtain this new estimate of the AMF MSMI criterion:

1. retain only the vector sequences for a MA filter of order $P \leq M-1$.

2. Let the MA filtering step be a moving window instead of a block window.

Since $\mathbf{A}$ and $\mathbf{D}_p$ are unknown they must be estimated via an appropriate multichannel parameter estimation method. It was shown through theory in [52] and through simulation in [49] that the best parameter estimation method for STAP is the Least Squares method (also known as the covariance method). Simulation results in [49] suggest that an order $P = 3$ ($<<< MN$) multichannel AR process is sufficient to accurately model the underlying process for airborne radar and as a result the computational cost associated with the least squares multichannel parameter estimation method(which forms the main block of the PAMF algorithm) is significantly lower than the $O((MN)^3)$ load associated with the inversion of estimate of $\mathbf{R}$ in the AMF method. The least squares problem can be expressed as follows,

$$\begin{aligned}
&\underline{\mathbf{X}}_r^H \underline{\mathbf{X}}_r \mathbf{A}' = \underline{\mathbf{X}}_r^H \underline{\mathbf{x}}_r \\
&\underset{L\times N}{\underline{\mathbf{x}}_r} = \begin{bmatrix} \mathbf{x}_r^T(M-1) & \mathbf{x}_r^T(M-2) & \cdots & \mathbf{x}_r^T(M-L) \end{bmatrix}^T \\
&\underline{\mathbf{X}}_r(t)_{L\times NP} = \begin{bmatrix} \underline{\mathbf{x}}_r(t) & \underline{\mathbf{x}}_r(t-1) & \cdots & \underline{\mathbf{x}}_r(t-P) \end{bmatrix} \\
&\underset{NP\times NP}{\mathbf{A}'} = \begin{bmatrix} \mathbf{A}^H(1) & \mathbf{A}^H(2) & \cdots & \mathbf{A}^H(P) \end{bmatrix}
\end{aligned} \tag{4.59}$$

where the subscript r denotes the range cell of interest, and L denotes the number of pulses used in the least square solution. A necessary but insufficient condition for $\underline{\mathbf{X}}_r^H \underline{\mathbf{X}}_r$ to be nonsingular is $P \leq L/2$. We will set $L = \lfloor 2M/3 \rfloor$ in our simulations. Therefore for a nonsingular $\underline{\mathbf{X}}_r^H \underline{\mathbf{X}}_r$ the solution to the least square problem is,

$$\widehat{\mathbf{A}'} = \left(\underline{\mathbf{X}}_r^H \underline{\mathbf{X}}_r\right)^{-1} \underline{\mathbf{X}}_r^H \underline{\mathbf{x}}_r \tag{4.60}$$

The PAMF method also shows robustness to the presence of discrete interference in the secondary data [49] and has performance that rivals that of the MF even in the case of limited sample support. Unfortunately the PAMF method is not CFAR, however simulation results suggest that for certain PAMF configurations CFAR like behavior does occur [49].

In our simulations we use the least squares parameter estimation method as well as two different methods for the estimation of the spatial whitening block filter (i.e., the block diagonal elements of D) namely the residual sample covariance matrix,

$$\widehat{\mathbf{D}_p}(m) = \frac{1}{K}\sum_{k=1}^{K} \varepsilon(n, k/H_0)\varepsilon^H(n, k/H_0) \qquad \{m = 0, \cdots, M-P-1\} \tag{4.61}$$

and time average sample covariance matrix methods,

$$\widehat{\mathbf{D}_p} = \frac{1}{(M-P-1)} \sum_{m=0}^{M-P-1} \widehat{\mathbf{D}_p}(m) \tag{4.62}$$

In the residual covariance matrix method the average is taken over range cells that do not contain target residues (thus the H_0 conditional hypothesis). In compliance with the Brennan rule it is assumed that $K \geq 2N$. The first method has the advantage of yielding a more CFAR like behavior while the second method has the advantage of larger detection probability [49]. In the results section we will provide simulation results of applying the PAMF to detect ideal and real targets injected in the datacube.

4.5 Realistic Target Model

Assuming a point target model has several advantages such as simplicity, localization to a single range bin, and the eliminating the need to incorporate the ambiguity function into the target model. Unfortunately ideal targets do not exist in the real world and we must therefore choose a realistic target model that more accurately portrays what is really happening. So far we have conducted simulations using ideal point targets localized to exactly one range cell. This resulted in some rather optimistic results for JDL that were perhaps not totally reflecting of its true performance in a practical scenario where the ideal target would be replaced by a realistic target spread over multiple ranges. To account for the spread of real targets in range we used obvious realistic targets directly extracted from a sample data-square (since only one spatial channel was used) provided to us by Dr. Riddolls. Figure 4.12 shows a range-Doppler plot of this data-square where the targets are indicated by arrows. Figure 4.13 shows several superposed cross-sections of the range-Doppler

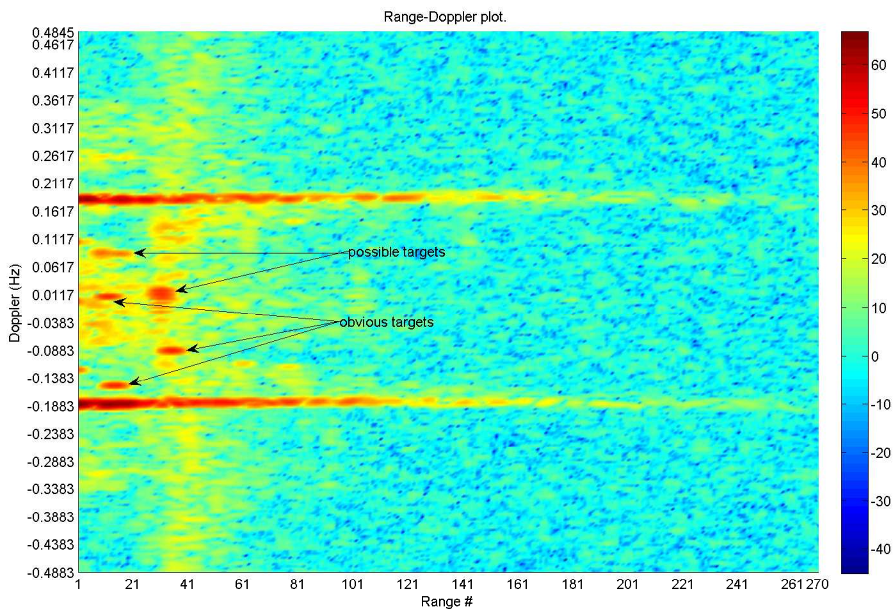

Figure 4.12: A range-Doppler plot of the data-square containing obvious targets. The targets are spread over up to 15 ranges and are at Doppler bin numbers 89, 106, 131, and 151 respectively.

plot at the Doppler bins corresponding to some of the identified targets present in the data-square. It should be noted that the range span of the data-square places it in the region dominated by Bragg lines and thus little to no ionospheric clutter masks the targets.

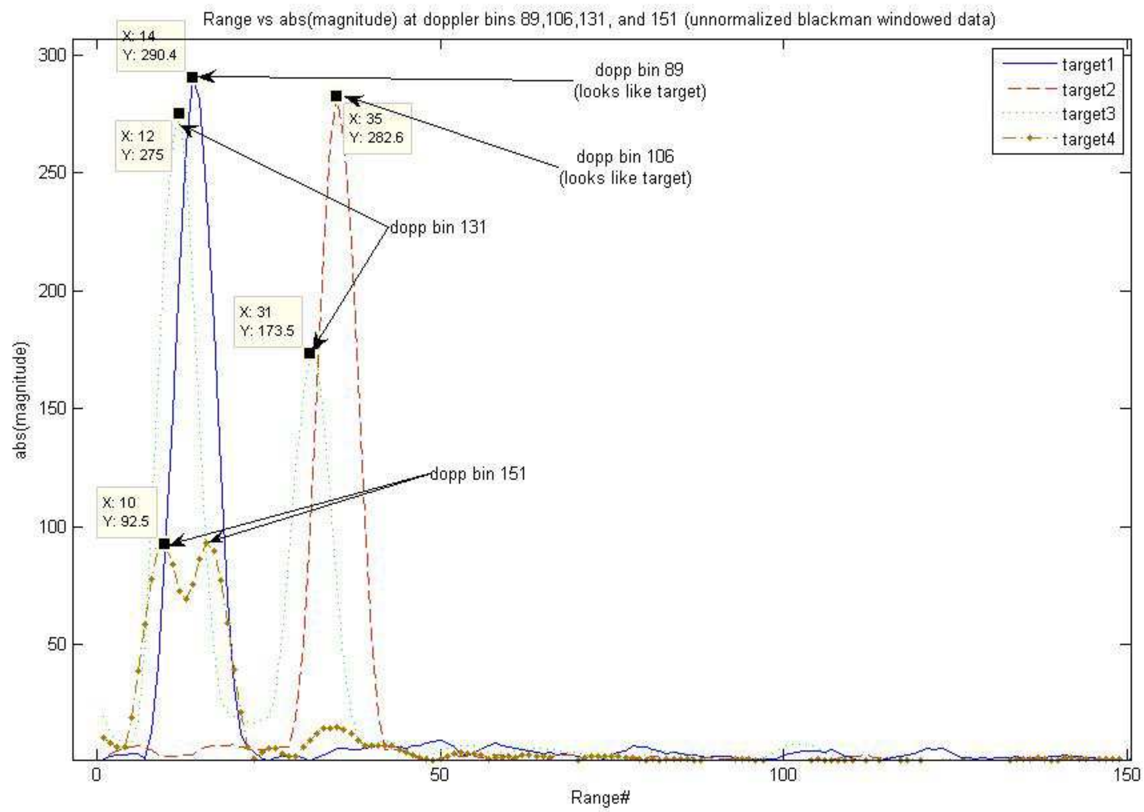

Figure 4.13: A power profile plot of the identified targets at Doppler bin numbers 89, 106, 131, and 151 respectively.

As can be seen from the plots in Figure 4.13 the realistic targets exhibit a range-power profile that extends over several range bins with the peak power located at the center of the target's range span. In our simulations we will particularly focus on the targets located at Doppler $-0.1526Hz$ and $-0.087Hz$ respectively. It should be noted that we first normalized the targets by dividing by the magnitude of the peak target amplitude, and then dividing by the magnitude of the corresponding steering vector, before actually injecting the target at the desired angle and Doppler locations.

Another thing worth mentioning about our previous simulation results for JDL is that we defined the amplitude of an ideal target, given by, $\xi(\mathbf{b}_t \otimes \mathbf{a}_t)$ as ξ. In the previous simulations we had set this amplitude to $\xi = 5$. In this definition the magnitude of the space-time steering vector is being ignored. In this report we will take this into account by normalizing by the magnitude of the steering vector. Therefore using this new definition of target amplitude and the fact that the norm of the space-time steering vector is $\sqrt{MN}$, the absolute target magnitude used in the

Table 4.2: Target Characteristics

Target Parameters	Ideal Target	Real Target
Range(s) number	215	212-218
Amplitude(dB)	35	57
Azimuth(degrees)	35	35
Doppler(Hz)	0.18	0.18

previous JDL simulations is $20 \log \left(\xi \sqrt{MN} \right) = 20 \log \left(5\sqrt{4096 \times 16} \right) = 62.14dB$. Note that this magnitude is an absolute magnitude and *not a SNR*.

Results

We begin this section by presenting some updated results of using JDL to identify both ideal and realistic targets injected into the region dominated by Ionospheric clutter. It should be mentioned that we conducted all our simulation results using the data-cube located in `hfswrdata25mar2002030257`. The characteristics of the injected ideal and real targets are summarized in Table 4.2 To assess the performance of the algorithms under scrutiny we will focus on the peak MSMI at the target range and the difference in MSMI (in dB) between the peak MSMI and the second highest MSMI, denoted as ΔMSMI. The larger the ΔMSMI the larger the capability of an adaptive algorithm to distinguish between a target and residual interference and thus the better is its performance. We begin by presenting some of the updated JDL simulation results.

Figures 4.14 and 4.15 show the MSMI statistic vs range plots for the injected ideal target using JDL. In Fig. 4.14 target amplitude is set to 35dB while in Fig. 4.15 the amplitude is set to 45dB. These large values are the absolute numbers used and are not the target SNR. Note that, in both figures, non-adaptive matched filtering cannot locate the injected target.

Figure 4.15 shows an MSMI vs range plot for the injected real target using JDL. It should be mentioned that the results presented in these figures for JDL are for an optimal angle and Doppler spacing obtained via a brute force search using a LPR composed of 3 angle and 10 Doppler bins. Note that we also superposed on both figures plots of simulation results obtained via non-adaptive matched filtering and adaptive Doppler processing. The adaptive Doppler processing algorithm performs only spatial adaption (i.e., one dimensional adaption) after Doppler filtering while the

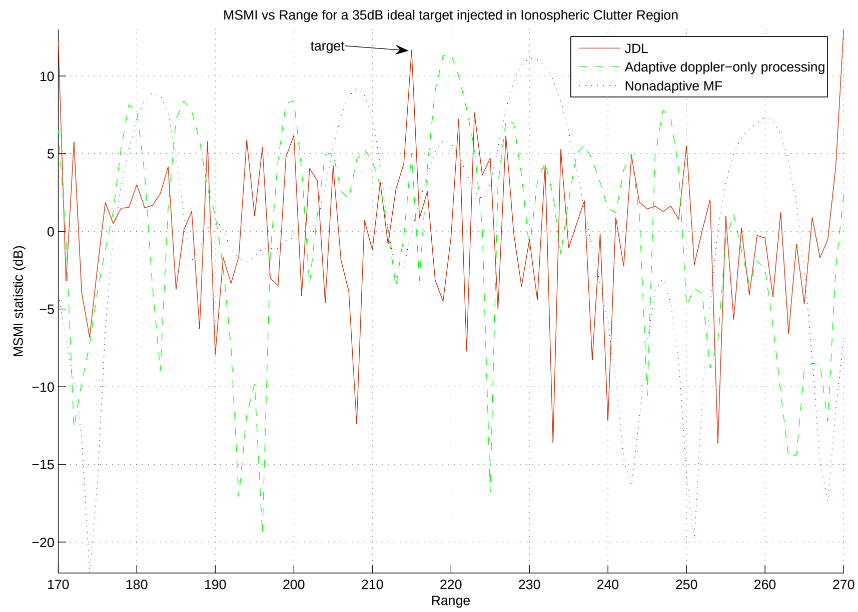

Figure 4.14: Results of using the JDL, Adaptive Doppler filter, and Nonadaptive MF algorithms to detect an ideal target with amplitude 35dB inserted into the Ionospheric clutter region.

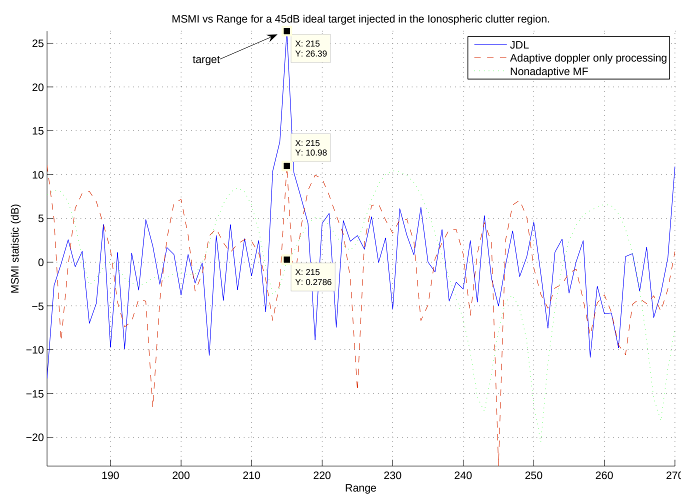

Figure 4.15: Results of using the JDL, Adaptive Doppler filter, and Nonadaptive MF algorithms to detect an ideal target with amplitude 45dB inserted into the Ionospheric clutter region.

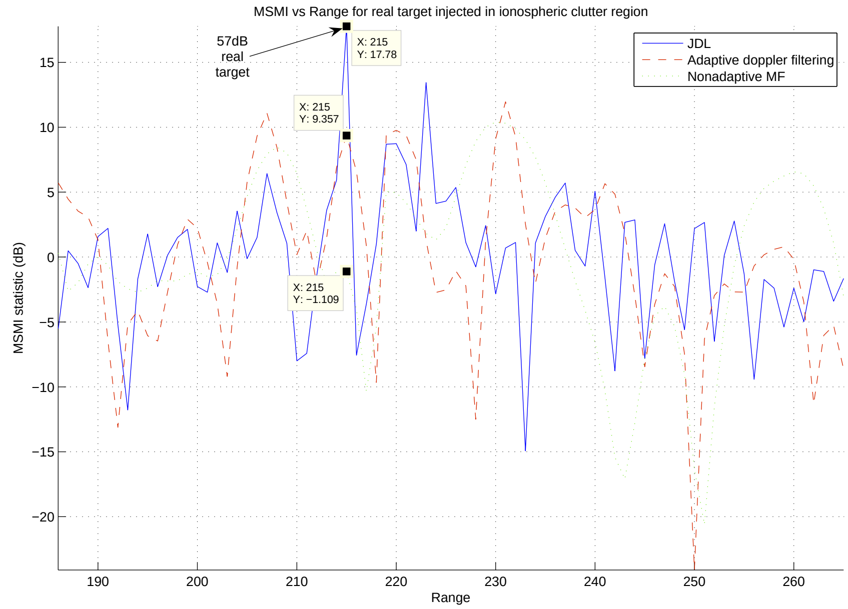

Figure 4.16: Results of using the JDL, Adaptive Doppler filter, and Nonadaptive MF algorithms to detect a real target spread over 7 range cells and with amplitude 57dB inserted into the Ionospheric clutter region.

nonadaptive processing only does non-adaptive Doppler filtering. From the ideal target plot it can be seen that JDL is capable of detecting the relatively weak target correctly even though the target is buried deeply in a region of the angle-Doppler space that is heavily dominated by both the ionospheric clutter as well as the high power external interference. The MSMI at the target is almost 8dB above the surrounding clutter which emphasizes JDL's ability to distinguish between an ideal target and surrounding clutter. Both the non-adaptive matched filtering and adaptive Doppler filtering methods fail at detecting the target. Our simulation results also indicated that for higher target amplitudes JDL's performance for the ideal target case by far exceeded that of both the nonadaptive as well as the adaptive Doppler methods.

For the real target scenario (Figure 4.16) JDL also boasts better performance than that of the adaptive Doppler filter and nonadaptive matched filters, however suffers a significant loss in performance as compared to the case of an ideal target localized to only one range bin. The spread of the target in range is accounted for by using a sufficient number of guard ranges (3 on either side of each look range) thus minimizing the contribution of ranges containing target components to the estimation of the interference covariance matrix. The peak MSMI of JDL in this case is 17.8dB and the corresponding Δ MSMI is about 4dB. Both the nonadaptive MF and adaptive Doppler processor fail to detect the real target.

These new results echo the conclusions reached previously with the additional newly gained confidence that JDL also has the capability to detect relatively weak realistic targets as well. Next we present some of the simulation results obtained by applying the D^3 and hybrid algorithms to detect ideal and real targets injected at various locations in the data-cube under investigation.

In our simulations for the D^3 and the hybrid and due to the large associated computational load of these algorithms we decided to use an under-sampled in pulse version of the datacube. We therefore used only 2048 of the 4096 pulses to run our simulations on the D^3 algorithm and 1024 pulses for the hybrid algorithm. We conducted simulations for both ideal and real targets injected into the region heavily dominated by ionospheric clutter. Figures 4.17 and 4.18 show the results of applying D^3 to the undersampled (in pulse) data-cube to detect ideal and realistic targets of peak amplitude $55dB$. D^3 is incapable of detecting either the real or the ideal injected targets and shows a rather poor performance relative to that of the Spatial adaptive processing algorithm. It should be noted that using a higher power target will inevitably lead to a better detection performance by the D^3 algorithm however its performance will still lag behind that of any statistical based algorithm. D^3's poor performance was anticipated since when used on its own, D^3 is incapable of suppressing the correlated interference present in each look range and thus will suffer a large degradation of performance as compared to a statistical adaptive algorithm such as JDL, for example.

We next went on to evaluate the performance of the hybrid algorithm in detecting ideal and real targets inserted into the region dominated by high power ionospheric clutter returns. Figures 4.19 and 4.20 show the results of using the Hybrid algorithm to detect an ideal and real target injected in the ionospheric region. As can be verified from the results the hybrid algorithm is capable of detecting both the ideal and real targets quite nicely. In fact it outperforms JDL in both the real and ideal cases. For the ideal target the hybrid algorithm yields a very good detection criterion, at the target range, of $32.45dB$ which is about $2.5dB$ greater than that of JDL. It also yields a superior Δ MSMI. In the real target scenario JDL fails to detect the target while the hybrid algorithm does so with about a $1dB$ margin. Note that we are using one fourth of the available number of pulses, and we are still getting quite good results for the hybrid algorithm. Thus the hybrid does a good job of suppressing any uncorrelated interference present in the look range after which it uses the second stage of the statistical JDL algorithm to null out any correlated interference that might be

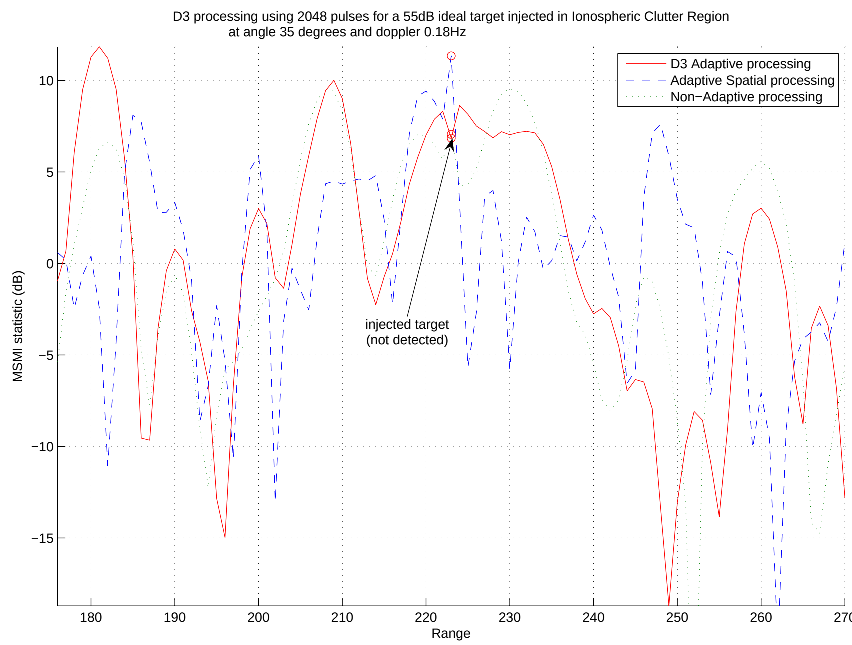

Figure 4.17: Results of using the D^3, Spatial Adaptive Doppler filter, and Nonadaptive MF algorithms to detect an ideal target with amplitude 55dB inserted into the Ionospheric clutter region.

masking the target. Again we emphasize the fact that we are performing all our simulations for a worst case target scenario; i.e., a relatively weak target buried in high power ionospheric clutter and high power external interference, with only a few secondary range bins to estimate an error covariance from.

We next conducted several simulations using the PAMF algorithm. Figures 4.21 and 4.22 plots the results of using the residual sample covariance matrix(RSC) and time average sample covariance matrix(TASC) PAMF methods with an assumed underlying multichannel AR order of 3, to detect ideal and real targets injected in the ionospheric clutter region. For this simulation we used an ideal target amplitude of $59dB$ and a real target amplitude of $57dB$. Both the RSC-PAMF and TASC-PAMF outperform the nonadaptive processor and successfully detected the injected ideal and real targets. Both these versions of the PAMF do not outperform either the adaptive Doppler filter or the JDL algorithm. A possible explanation of this rather unsatisfying performance is that the AR order used in the simulations was an order of 3 which was recognized as the optimal order for airborne radar. However given the highly non-homogeneous structure of the clutter in the HFSWR scenario it is very likely that an order of only 3 would be less than adequate to accurately model the underlying clutter statistics. It should also be noted that in our simulation results the

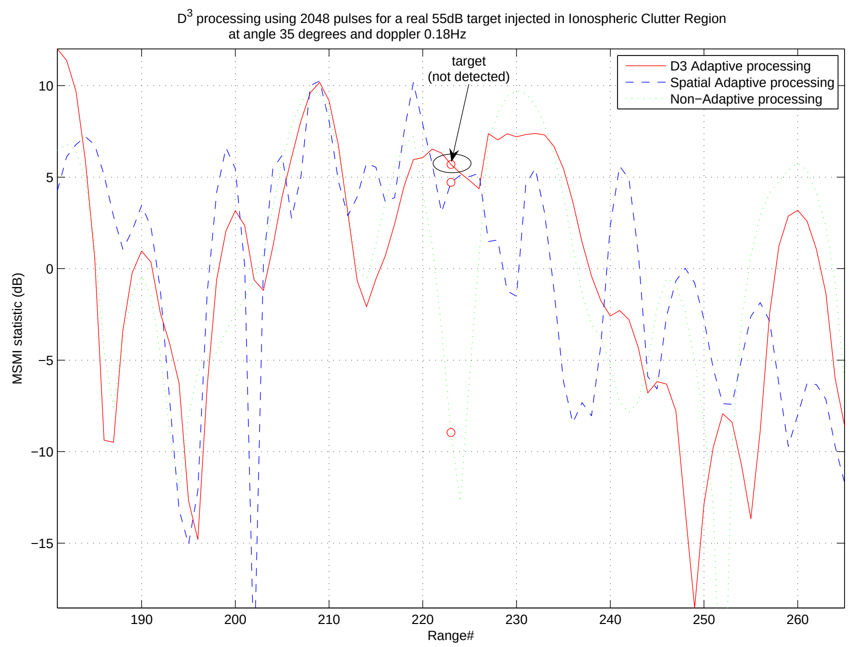

Figure 4.18: Results of using the D^3, Spatial Adaptive Doppler filter, and Nonadaptive MF algorithms to detect a real target spread over 7 range cells and with amplitude 55dB inserted into the Ionospheric clutter region.

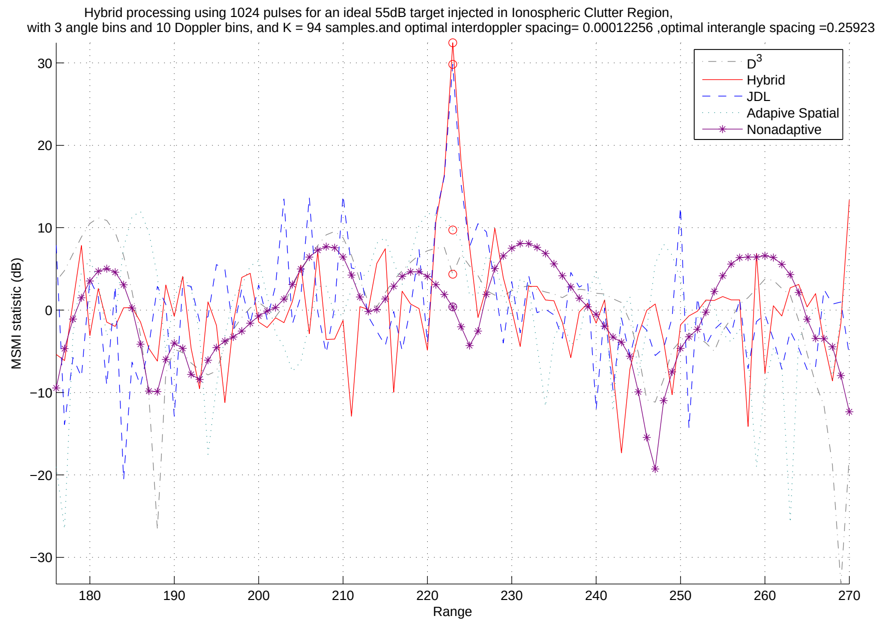

Figure 4.19: Results of using the Hybrid,D^3,JDL, Spatial Adaptive Doppler filter, and Nonadaptive MF algorithms to detect an ideal target with amplitude 55dB inserted into the Ionospheric clutter region.

RSC-PAMF does a better job at detecting the injected target than the TASC-PAMF method.

4.5.1 Discussion on STAP Algorithms

In the area of applying STAP to ionospheric clutter, in this report we presented new simulation results of using several STAP algorithms to suppress high power nonhomogeneous clutter returns from the highly non-stationary ionospheric layers. We began by incorporating real targets into our simulations and testing the various algorithms to see how well they fare against realistic targets. In particular we ran several tests on the JDL algorithm to evaluate its realistic target detection capabilities. Our simulation results indicate that JDL does a good job at detecting such targets even when they are spread over up to 7 range bins.

We also implemented and tested 3 new algorithms in this report, namely the D^3 algorithm, the Hybrid algorithm, and the PAMF algorithm. The D^3 did not perform well for both ideal and real targets. This was expected given the algorithm's weakness against correlated clutter that seems to be the dominant type of clutter in the ranges we analyzed. The Hybrid algorithm on the other hand showed very good detection performance for both ideal, and more importantly, real targets.

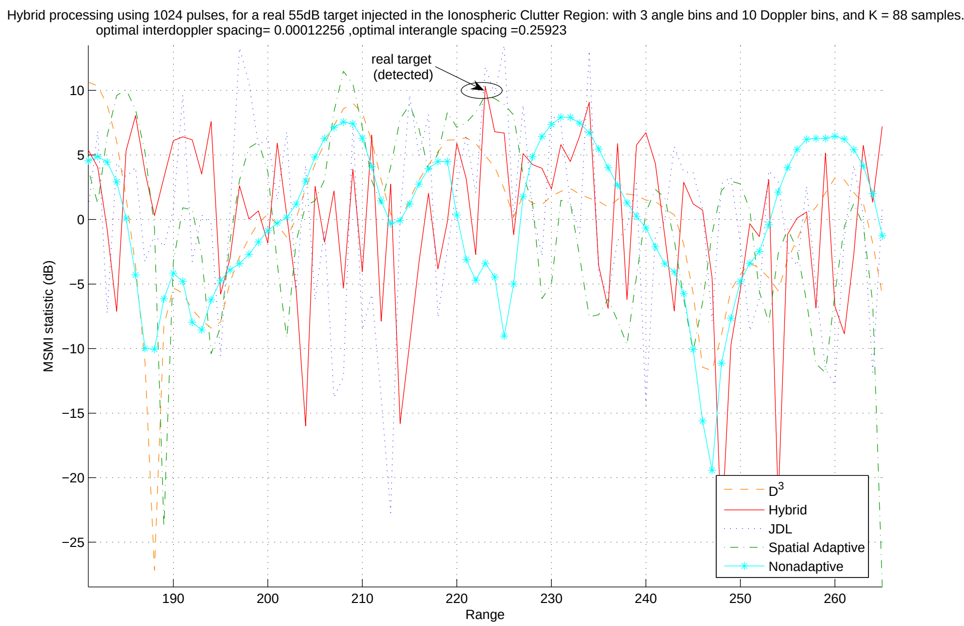

Figure 4.20: Results of using the Hybrid,D^3,JDL, Spatial Adaptive Doppler filter, and Nonadaptive MF algorithms to detect a real target spread over 7 range cells and with amplitude 55dB inserted into the Ionospheric clutter region.

The Hybrid outperformed JDL and all the other tested methods and so far seems to yield the best performance among the algorithms we tested. It is well known that the Hybrid algorithm yield superior results in airborne radar, but our investigations seem to strongly affirm that the Hybrid is also a robust and well performing algorithm in HFSWR applications.

The final algorithm we investigated was the PAMF algorithm which highly depends on assumptions made about the nature of the underlying clutter. Assuming the clutter to be an AR(p) process (which may not be completely justified in the case of ionospheric highly non-homogeneous clutter), we had to select an appropriate order p that yields a sufficiently accurate representation of the clutter statistics. We used an AR order of 3 in our simulations,which is the optimal order for airborne radar. The results obtained with this choice of order and using the PAMF algorithm for ideal and real target detection in the ionospheric region, yielded some modest results that were by no mean striking to us.

The next section describes a key contribution of this report - the development of the Fast Fully Adaptive algorithm, an extremely efficient scheme based on the Fast Fourier Transform (FFT)

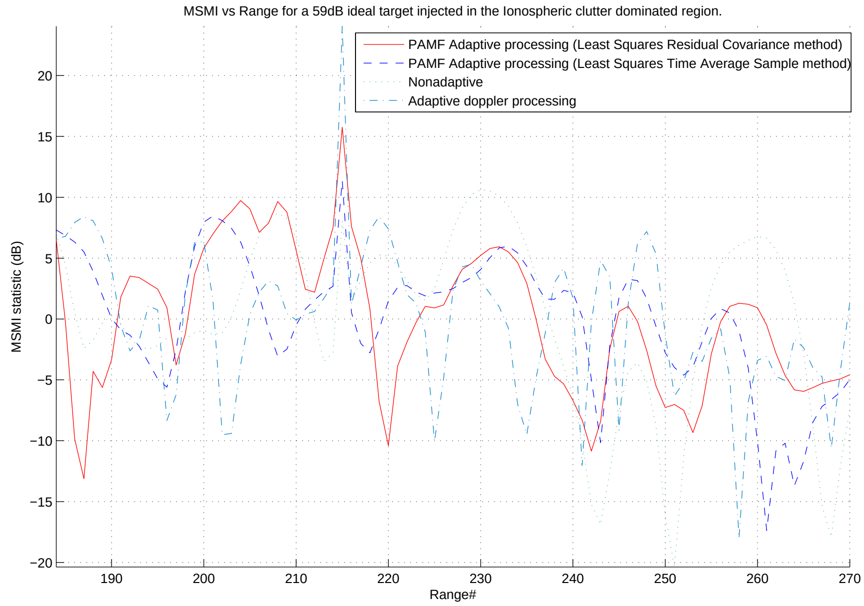

Figure 4.21: Results of using the RSC-PAMF, TASC-PAMF, Adaptive Doppler filter, and Non-adaptive MF algorithms to detect an ideal point target with amplitude 59dB inserted into the Ionospheric clutter region.

4.6 Fast Fully Adaptive Algorithm

In the previous section we provided results of Monte Carlo simulation to evaluate the processing gain of the non-adaptive, spatially adaptive, JDL and parametric adaptive matched filter (PAMF) methods to detect weak targets embedded within the ionospheric clutter that dominates the far ranges of the measured data sets. We also addressed the problem related to the aliasing in pulse due to downsampling without low pass filtering. We then provided a brief complexity analysis of the JDL and Hybrid algorithms. We provided several simulation results that validated our previous work.

In this section we introduce the new FFA algorithm and perform a complexity analysis which we contrast against that of the JDL algorithm. We also evaluate the performance of the FFA algorithm and compare it to that of non-adaptive and JDL methods for HFSWR. We begin by developing the FFA algorithm for a general linear array of isotropic point sensors processing M coherent pulses as in the original STAP work of Ward [44].

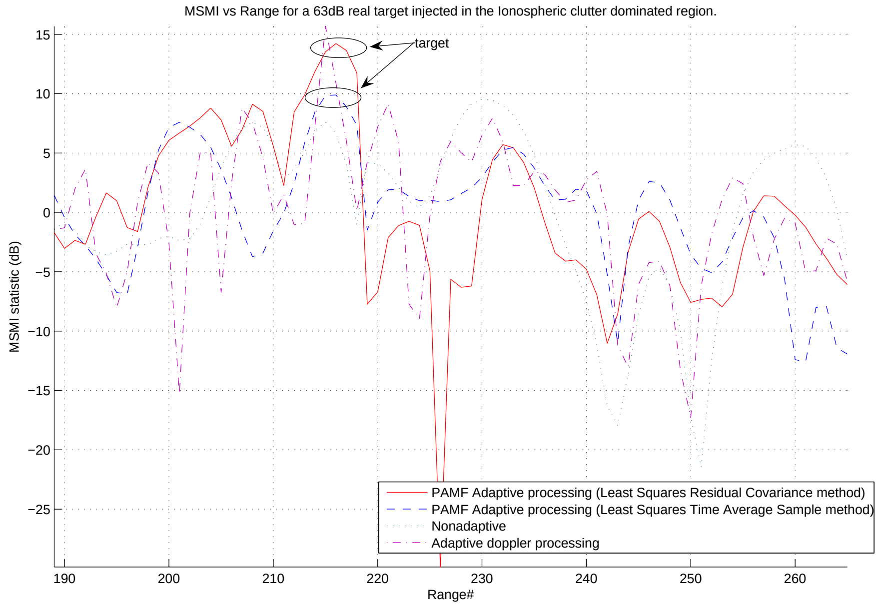

Figure 4.22: Results of using the RSC-PAMF, TASC-PAMF, Adaptive Doppler filter, and Non-adaptive MF algorithms to detect a real target spread over 7 range cells and with amplitude 63dB inserted into the Ionospheric clutter region.

4.6.1 System Model

Since the primary focus of this project is the adaptive suppression of ionospheric clutter in HFSWR applications, we will only evaluate our method using the measured HFSWR data made available to us through Dr. Riddolls. We will treat the combined effects of all clutter sources as colored noise. Ideal targets in the HFSWR scenario can be modeled (quite accurately) in a fashion similar to targets in airborne applications (i.e., point sources localized in azimuth, doppler, and range), and as a result we will use the conventional space-time steering vector, developed in the airborne radar literature [44], to model target returns in HFSWR.

To develop the FFA algorithm, we will adopt the conventional STAP setup. The receiver comprises N spatial channels separated by a distance of $\lambda/2$, processing over M coherent pulses with a pulse repetition frequency (PRF) of f_p. The data comprises any potential target, background clutter (including sea and ionospheric clutter), interference, and receiver noise. This process is repeated for the numerous ranges of interest, and the corresponding $N \times M$ space-time snapshots at each range are compiled into one big data-cube. For a specific range bin, r, the $N \times M$ data matrix is given by:

$$
\begin{aligned}
&\mathbf{X} = \xi\mathbf{V} + \mathbf{C} + \mathbf{N}, \\
&\mathbf{V} = \mathbf{a}(\varphi_t) \otimes \mathbf{b}^T(f_t), \\
&\mathbf{a}(\varphi_t) = \begin{bmatrix} 1 & z_s & \cdots & z_s^{(N-1)} \end{bmatrix}^T \\
&\mathbf{b}(f_t) = \begin{bmatrix} 1 & z_t & \cdots & z_t^{(M-1)} \end{bmatrix}^T \\
&z_s = e^{i2\pi(d/\lambda)\sin(\varphi_t)}, \\
&z_t = e^{i2\pi(f_t/f_R)},
\end{aligned}
\tag{4.63}
$$

where ξ is the target amplitude, $\mathbf{a}(\varphi_t)$ and $\mathbf{b}(f_t)$ are the target spatial and temporal steering vectors respectively, at azimuth φ_t and doppler f_t , and $\mathbf{C}$ and $\mathbf{N}$ represent the clutter and noise space-time contributions respectively. The value of ξ is either zero under the null hypothesis (i.e., no target present) or nonzero for the case when a target is present.

Ideally a target (if present) is localized in range to one range bin, however in real systems the radar ambiguity function leads to a spread of the target over several ranges, and this spread must be accounted for in the target model. It should be noted that for the HFSWR system considered here, the radar waveform consists of a complementary set of 8 phase code pulses. Each of the 8 pulses in turn consists of 8 bits, where each bit is 55 microseconds long, and thus each pulse is 440 microseconds long. Thus in order to account for the spread of the target in range we also use a realistic target space-time vector which is spread over range and extracted from actual real high-SNR target returns present in separately measured data cubes. The target signal is extracted using a matched filter, localizing the target in Doppler.

4.6.2 Fast Fully Adaptive Algorithm

We will begin by briefly describing the optimal MF method and AMF method, since they constitute the core of the FFA method. Assuming prior knowledge of the interference statistics, and as a result of the error covariance matrix $\mathbf{R}$, the matched filter solution leads to the computation of the following optimal weight vector,

$$\mathbf{w}_{opt} = \mathbf{R}^{-1}\mathbf{v}, \tag{4.64}$$

where $\mathbf{R}$ is the known interference covariance matrix and $\mathbf{v}$ is the space-time steering vector at the angle and Doppler of interest. The vector $\mathbf{v}$ is the vectorized version of space-time steering matrix $\mathbf{V}$ used in Eqn. 4.63.

Unfortunately, it is seldom the case that the interference statistics are known apriori, and thus must be estimated from the neighboring ranges. This leads to the AMF solution which is identical to the MF solution with the known covariance $\mathbf{R}$ replaced by its maximum likelihood estimate $\widehat{\mathbf{R}}$ which is given by,

$$\widehat{\mathbf{R}} = \frac{1}{K}\sum_{r=1}^{K}\mathbf{x}_k\mathbf{x}_k^H \tag{4.65}$$

where $\mathbf{x}_k$ is the vectorized space-time snapshot at the k'th range. We can then evaluate the following MSMI statistic, which exhibits CFAR properties,

$$\frac{\left|\mathbf{v}^H\widetilde{\mathbf{R}}^{-1}\mathbf{x}\right|^2}{\mathbf{v}^H\widetilde{\mathbf{R}}^{-1}\mathbf{v}}. \tag{4.66}$$

However computing the estimate $\widetilde{\mathbf{R}}$, and obtaining an accurate inverse requires a large sample support. As developed by the RMB rule [45], the number of *statistically homogeneous* range cells must exceed at least $2NM$. In addition, this inversion leads to an impractical computational load in the order of $O\{(NM)^3\}$. However, it is the requirement of statistically homogeneous sample support that is fundamentally impossible to meet in practice.

In order to surmount this problem we will attempt to adopt a divide and conquer strategy that breaks up the $N \times M$ space time snapshot into $t_s.t_t$ $N' \times M'$ smaller spatio-temporal matrices where N' and M' are chosen to satisfy $N' \ll N$ and $M' \ll M$ respectively. We then apply a modified version of the AMF algorithm on each of these reduced snapshots to end up with a new $t_s \times t_t$ matrix whose entries are composed of *the output statistics of the corresponding AMF processes.* Then this new 'spatio-temporal' reduced size snapshot is once again repartitioned (not necessarily in the same way as the original space-time snapshot) and each partition processed by the modified AMF yielding a further reduced dimensional 'spatio-temporal' snapshot. This procedure is repeated until a final statistic is obtained, which is then compared to an appropriate threshold to decide if a target is present at the look range of interest. Note that this tree like approach of combining successively smaller problems is reminiscent of the radix-2 based FFT algorithms.

To formalize this approach, we begin with the original $N \times M$ space-time snapshot at the range of interest. We next choose an appropriate spatial and temporal partitioning scheme that partitions the $N \times M$ space-time snapshot into $t_s.t_t$ $N' \times M'$ smaller spatio-temporal squares where, as mentioned above, N' and M' are chosen to satisfy $N' \ll N$ and $M' \ll M$ respectively (see 4.23). For this partitioning scheme to be valid t_s must be a factor of the current spatial dimension, N, and t_t must be a factor of the current temporal dimension, M. We apply the same partitioning scheme to the $N \times M$ steering matrix at the angle and Doppler of interest. We will denote the n-th spatial and m-th temporal partition of the space-time snapshot and steering matrix as $\mathbf{X}_{nm}$ and $\mathbf{V}_{nm}$ respectively where $n = 1, 2, .., t_s$ and $m = 1, 2, .., t_t$. It is important to note that each $\mathbf{V}_{nm}$ can be written as,

$$\mathbf{V}_{nm} = z_s^{(n-1)N'} z_t^{(m-1)M'} \mathbf{V}_{11} \tag{4.67}$$

where z_s and z_t are the current spatial and temporal spacings. We begin by processing the first spatial and temporal snapshot, V_{11}. Since the size of the vectorized version of X_{11} is $N'M' \times 1$, significantly reduced sample support to compute an accurate estimate of the error covariance for this particular reduced snap-shot (i.e., on the order of $2N'M'$, not $2NM$ samples) and the computation load is reduced to $O(N'M')^3)$. We next form the optimal AMF weight vector as follows,

$$\mathbf{w}_{11}^{(1)} = (\widehat{\mathbf{R}}_{11}^{(1)})^{-1} \mathbf{v}_{11}^{(1)} \tag{4.68}$$

where $\mathbf{v}_{11}$ is the vectorized form of $\mathbf{V}_{11}$ and is of size $N'M' \times 1$. The superscript is used to indicate the depth in the FFT tree-like structure we are at. At this stage it is set to 1 since we are still using the original space-time snapshot in our processing. Unlike the CFAR AMF we will not utilize the MSMI criterion at this stage; instead we will compute the following statistic,

$$\begin{aligned} y_{11}^{(1)} = \frac{(\mathbf{w}_{11}^{(1)})^H \mathbf{x}_{11}^{(1)}}{(\mathbf{w}_{11}^{(1)})^H \mathbf{v}_{11}^{(1)}} &= \frac{(\mathbf{w}_{11}^{(1)})^H (\mathbf{c}_{11}^{(1)} + \mathbf{n}_{11}^{(1)})}{(\mathbf{w}_{11}^{(1)})^H \mathbf{v}_{11}^{(1)}} + \xi \frac{(\mathbf{w}_{11}^{(1)})^H (\mathbf{v}_{11}^{(1)})}{(\mathbf{w}_{11}^{(1)})^H \mathbf{v}_{11}^{(1)}}, \\ &= \frac{(\mathbf{w}_{11}^{(1)})^H (\mathbf{c}_{11}^{(1)} + \mathbf{n}_{11}^{(1)})}{(\mathbf{w}_{11}^{(1)})^H \mathbf{v}_{11}^{(1)}} + \xi = s_{11}^{(1)} + \xi, \end{aligned} \tag{4.69}$$

where $\mathbf{c}_{11}^{(1)}$ and $\mathbf{n}_{11}^{(1)}$ are the clutter and noise components in the current partition, and where we denote the residual noise plus interference statistic as $s_{11}^{(1)}$. In a similar fashion we can compute the optimal weight of the (n, m)'th partition as follows,

$$\mathbf{w}_{nm}^{(1)} = (\widehat{\mathbf{R}}_{nm}^{(1)})^{-1} \mathbf{v}_{nm}^{(1)}. \tag{4.70}$$

We are now ready to compute the modified AMF statistic as follows,

$$\begin{aligned} y_{nm}^{(1)} = \frac{(\mathbf{w}_{nm}^{(1)})^H \mathbf{x}_{nm}^{(1)}}{(\mathbf{w}_{nm}^{(1)})^H \mathbf{v}_{11}^{(1)}} &= \frac{(\mathbf{w}_{nm}^{(1)})^H (\mathbf{c}_{nm}^{(1)} + \mathbf{n}_{nm}^{(1)})}{(\mathbf{w}_{nm}^{(1)})^H \mathbf{v}_{11}^{(1)}} + \xi \frac{(\mathbf{w}_{nm}^{(1)})^H (\mathbf{v}_{nm}^{(1)})}{(\mathbf{w}_{nm}^{(1)})^H \mathbf{v}_{11}^{(1)}}, \\ = \frac{(\mathbf{w}_{nm}^{(1)})^H (\mathbf{c}_{nm}^{(1)} + \mathbf{n}_{nm}^{(1)})}{(\mathbf{w}_{nm}^{(1)})^H \mathbf{v}_{11}^{(1)}} &+ \frac{\xi (\mathbf{w}_{nm}^{(1)})^H (\mathbf{v}_{11}^{(1)} z_s^{(n-1)N'} z_t^{(m-1)M'})}{(\mathbf{w}_{nm}^{(1)})^H \mathbf{v}_{11}^{(1)}}, \\ &= \frac{(\mathbf{w}_{nm}^{(1)})^H (\mathbf{c}_{nm}^{(1)} + \mathbf{n}_{nm}^{(1)})}{(\mathbf{w}_{nm}^{(1)})^H \mathbf{v}_{11}^{(1)}} + \xi z_s^{(n-1)N'} z_t^{(m-1)M'} \\ &= s_{nm}^{(1)} + \xi z_s^{(n-1)N'} z_t^{(m-1)M'} \end{aligned} \tag{4.71}$$

where we made use of the relation in 4.67 between the (n, m)-th steering matrix partition and the first steering matrix partition. Defining $z_s^{\{1\}}$ and $z_t^{\{1\}}$ as follows,

$$\begin{aligned} z_s^{\{1\}} &= z_s^{N'} \\ z_t^{\{1\}} &= z_t^{M'} \end{aligned} \tag{4.72}$$

and comparing $y_{11}^{(1)}$ and $y_{nm}^{(1)}$, we notice that the residual signal component of $y_{nm}^{(1)}$ is $(z_s^{\{1\}})^{n-1}(z_t^{\{1\}})^{m-1}$ times the residual signal component of $y_{11}^{(1)}$. This indicates that through our careful choice of a modified statistic, we have preserved the phase relationship between the residual signal components of different spatio-temporal partitions after being processed through the modified AMF filters. We can thus regard the resulting $t_s \times t_t$ matrix as a new 'spatio-temporal' snapshot with a fraction of the temporal and spatial degrees of freedom (DoF) of the original space-time snapshot, and containing a target with the same amplitude but with *new Doppler and angle phase shifts* given by $z_t^{\{1\}}$ and $z_s^{\{1\}}$ respectively.

Choosing a new set of spatial and temporal partitions for the resulting spatio-temporal matrix at each depth, and repeating the modified AMF algorithm on each of these partitions, will systematically lead to the evaluation of a final detection statistic which indirectly incorporates all the DoF of the original data-cube at different depths of the algorithm. However the resulting statistic is not CFAR. To overcome this problem we use the MSMI CFAR statistic as the detection statistic computed at the final stage of the algorithm where only one final spatio-temporal partition remains. This has the effect of making the final statistic CFAR. It should also be mentioned that at every depth we must also 'modify' the secondary data appropriately. To accomplish this we perform the same computation, conducted at the look range of every partition, to all the corresponding spatio-temporal partitions at all the secondary ranges used.

4.6.3 Complexity Analysis

The FFA algorithm yields significant improvement in computation speed load compared to the practically un-achievable AMF. However the real test of valor will be a comparison of the complexity of the FFA Algorithm to other STAP algorithms that have been designed for their low computation load, such as the JDL algorithm. It is somewhat difficult to compare complexities of algorithms that have numerous defining parameters such as the number of angle and doppler bins that dictate the complexity of JDL, or the spatio-temporal partition sequence choice that almost fully characterizes the complexity and performance of the FFA Algorithm. Nonetheless, we will attempt to provide

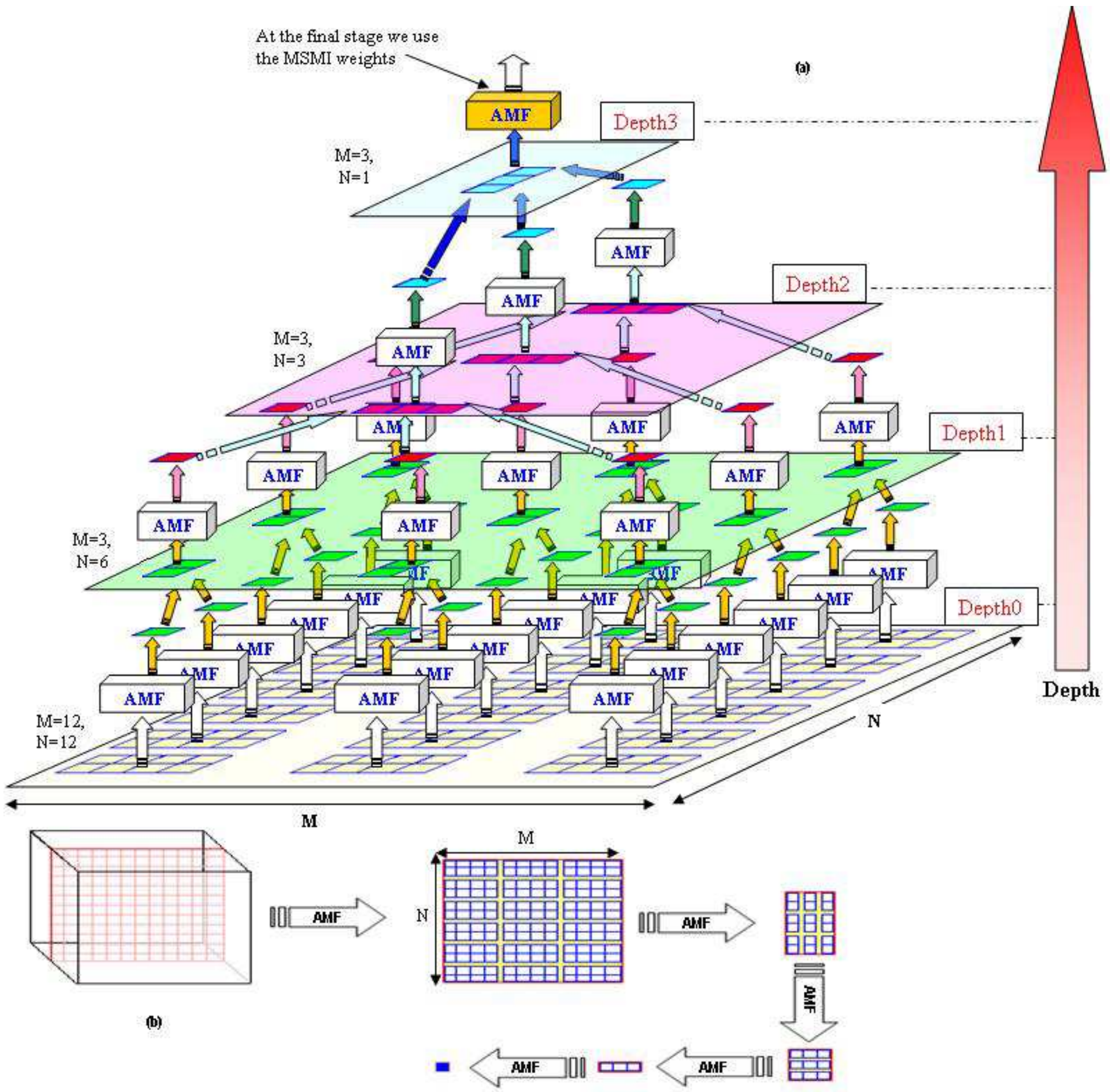

Figure 4.23: A tree-like representation of the FFA method for a datacube with $M = 12$ pulses, $N = 12$ elements, spatial-partitioning-sequence=[2 2 1 3], and temporal-partitioning-sequence=[4 1 3 1].

some sense of complexity evaluation that, in turn, will better allow us to characterize the utility of our algorithm in practical STAP scenarios. The algorithm we choose to compare complexity against is the JDL algorithm since it is a reduced dimension algorithm that has been designed with a particular focus on reduction of complexity. As a starting point we will derive the 'generic' expression defining the complexity of JDL and the FFA Algorithm in terms of their corresponding parameters.

Beginning with JDL, we assume a local processing region (LPR) comprising η_a angle bins and η_d Doppler bins. Reducing the size of the LPR leads to a reduction in the computation times of the JDL algorithm, but also leads to a loss of performance. The algorithm running time for one look range can be approximated as $T_{JDL} = \eta_a \eta_d (T_1) + \epsilon$ where T_1 is the time needed to compute 1 column entry of the JDL transformation matrix, and ϵ is the time needed to perform inversion of the covariance matrix and is a function of $O((\eta_a \eta_d)^3)$. However the transformation matrix needs to be computed only once, and not for every look range. Consequently for r look ranges the running time of JDL would approximately be $\eta_a \eta_d (T_1) + rO((\eta_a \eta_d)^3)$.

Next we derive the complexity of the FFA Algorithm. In essence its complexity for a spatio-temporal partition of size $N' \times M'$ is that of the AMF and is primarily defined by the complexity associated with the inversion of an $N'M' \times N'M'$ matrix, and is therefore $O((N'M')^3)$. This process is repeated $t_s^d.t_t^d$ times at every depth, d, where t_s^d must be a factor of N and t_t^d must be a factor of M. Thus assuming a given spatial partitioning sequence $S_N = \{n_1, n_2, ..., n_{\max(k_N,k_M)}\}$ and a temporal partitioning sequence $S_M = \{m_1, m_2, ..., m_{\max(k_N,k_M)}\}$, where m_i and n_i are the spatial and temporal dimensions of the partitions at depth i, and k_N and k_M are the largest non-unit spatial and temporal factor indices respectively. In order to make both spatial and temporal sequences of the same size we augment the shorter sequence with $1's$ until both sequences are the same length. Thus the maximum depth of the FFT-like tree is given by $\max(k_N, k_M)$. As a result the complexity of the FFA per range can be written as,

$$T_{FFA} = \sum_{d=1}^{\max(k_N,k_M)} \left\{ \frac{NM}{\prod_{i=1}^{d} n_i m_i} O\left((n_d m_d)^3\right) \right\} = \sum_{d=1}^{\max(k_N,k_M)} \left\{ \left(\prod_{i=d}^{\max(k_N,k_M)} n_i m_i \right) O\left((n_d m_d)^2\right) \right\} \tag{4.73}$$

and since this process must be repeated for all look ranges, then for r ranges the running time would be rT_{FFA}. As can be seen by comparing the 2 expressions outlining the complexities of the 2 algorithms being evaluated, it is not straight forward to draw a definite conclusion. We

Table 4.3: Average Running Time of various algorithms per look range per look angle per look doppler

Algorithm	Avg Running Time(sec)
Nonadaptive	0.005
Spatial Adaptive	0.007
JDL (with 3 angle and 11 doppler bins)	0.57
D^3 (using 2048 pulses)	15.35
PAMF(with AR order of 5)	6.66
Hybrid(using 2048 pulses with 3 angle and 11 doppler bins)	497.25
FFA	2.8404

can manipulate the various parameters of each algorithm to favor either algorithm, in terms of complexity. However the performance is directly related to the parameters and is often characterized by an inverse relationship with the complexity, and therefore a tradeoff is inevitable. In general, in terms of computation load, JDL has the distinct advantage that it requires the solution of single size-$\eta_a\eta_d$ matrix while the FFA approach requires several AMF solutions. On the other hand, in terms of performance, the FFA algorithm uses all NM adaptive DoF while the JDL is restricted to just $\eta_a\eta_d$.

Table 4.3 shows some example average running times for the FFA, JDL, Hybrid, D^3, and PAMF methods obtained from simulations using the measured data-cubes made available to us by the DRDC. The processor used is a DuoCore2 processor with 2GB of RAM and a speed of 2.13GHz running the Windows XP operating system.

The above JDL results are for 11 doppler bins and 3 angle bins, and the FFA results are for a spatial-partitioning-sequence= $[2, 2, 2, 2]$ and a temporal-partitioning-sequence= $[4, 4, 16, 16]$. Note that the time results for D^3 and hybrid algorithms are for a decimated datacube by a factor of 4, and the result for the PAMF algorithm is for an assumed AR order of 5. Also we are using a LPR composed of $\eta_a = 3$ angle bins and $\eta_d = 11$ doppler bins. In this case JDL is about 78% faster than FFA for the chosen partitioning scheme. It should be noted that the FFA program used in our simulations has not yet been optimized for minimal running time, while the JDL program has undergone code optimization. However comparing the FFA (for this particular partitioning scheme)to the Hybrid, D^3, and PAMF methods we can see a significant speedup. Furthermore, as we will see, the performance of FFA algorithm is hugely superior to that of the JDL algorithm.

It should be noted that for the FFA method to yield complexity reductions both N and M must have factors that are relatively small (for example both N and M are powers of 2 - this is similar to that required by the FFT algorithm).

4.6.4 Simulation Results

In this section we will evaluate the performance of the FFA algorithm in the HFSWR setup using both ideal point targets and realistic targets spread in range. We will provide MSMI statistic versus Range plots to characterize the performance of our algorithm and compare it to that of the non-adaptive and JDL methods. We will thus inject ideal and real targets at specific locations in the datacube, and use the three methods to attempt to detect the injected target. We will also focus on the difference between the target MSMI statistic (assumed to be the largest) and the second largest MSMI statistic, termed Δ MSMI, which we will use as a sensitivity measure i.e., the larger the Δ MSMI of a certain algorithm, the larger its ability to distinguish a target from a background of interference and noise. Since we neither have sufficient measured data to evaluate a detection threshold for a given probability of false alarm, nor the capability to generate such data due to the absence of an accurate model for ionospheric clutter, we will only declare a target detection to be successful if the MSMI statistic at the target range is the maximum among the look ranges being scanned for targets. We will begin with the ideal target scenario, where we inject a weak ideal point target into the measured HFSWR data cubes, to test the target detection capability of each of the FFA,Nonadaptive, and JDL methods.

In our example, we inject our ideal $45dB$ target at range number 223 which is at the center of the ionospheric clutter region, at an angle of $35°$ which is within the external interference angle span, and at a Doppler of $0.18Hz$ which coincides with the Bragg-Line Doppler frequency of the data-cube at hand. It is important to note that $45dB$ measures the absolute amplitude of the injected target, as opposed to the SINR. It should also be noted that due to the large number of pulses (4096) it is computationally impossible to produce MSMI versus range plots for the AMF since the inversion of the associated covariance would be on the order of $O((MN)^{3)} = O(2.8147e{+}014)$. Instead we focus on a comparison between the performance of the FFA method and that of JDL and nonadaptive processing. Figure 4.25 shows the detection results for the methods being investigated. For this simulation the spatial-partitioning sequence and temporal-partitioning sequence we selected for FFA are $[2, 2, 2, 2]$ and $[4, 4, 16, 16]$ respectively, and the JDL parameters are the same ones used in the airborne radar simulations presented earlier. As can be seen from Fig. 4.25 the nonadaptive algorithm fails at detecting the target, while both the FFA and JDL methods do successfully detect the presence of a target. However it is evident from examining the curves that the FFA shows about a $10dB$ *improvement in* Δ *MSMI as compared to JDL*, which emphasizes the FFA's superior target discrimination capabilities. It should be noted that the FFA results for this simulation are for only one possible spatio-temporal partition sequence, which has not been optimized in any way. We therefore expect that there exists other spatio-temporal sequences that may yield even larger improvements in performance and push the performance boundary even closer to that of the AMF with ample sample support. We next investigate how the FFA fairs in a reduced DoF scenario where we use only a fraction of the available 4096 pulses for target detection. Figure 4.26 plots the MSMI versus range curves for the FFA, JDL, and Nonadaptive methods using only 128 out of the 4096 available pulses (i.e., a reduction by a factor of 32). Once again the non-adaptive method fails, while both the FFA and JDL methods succeed at localizing the target. Note that due to the decimation in pulse, the performance of both algorithms is worse than before, however the FFA still outperforms the JDL by a Δ MSMI margin of about $3.5dB$, again asserting its superior target discrimination capacity. It should be mentioned that for this simulation we used a spatial-partitioning sequence of $[2, 2, 2, 2]$ and temporal-partitioning sequence of $[2, 4, 4, 4]$ for the FFA method.

We next investigate the performance of the FFA method for real target scenarios. In this simulation we inject real targets spread over several ranges, which have been extracted from actual target returns present in the data-cubes made available to us by the DRDC. We use the same FFA and JDL parameters used in the ideal target simulation utilizing all 4096 pulses. The results are shown in Fig. 4.27, where it is evident that both the nonadaptive *as well as the JDL methods fail to detect the buried real target* while the FFA method successfully does so with a Δ MSMI margin of $12.8dB$. We next repeat the simulations for a reduced pulse scenario. Again we use the same setup outlined in the decimated in pulse ideal target case. The results are shown in Fig. 4.28, and once again indicate that only the FFA method can successfully detect the real target and does so with a margin of more than $8dB$.

To further illustrate the superiority of the FFA method, we produce Δ MSMI vs Target Ampli-

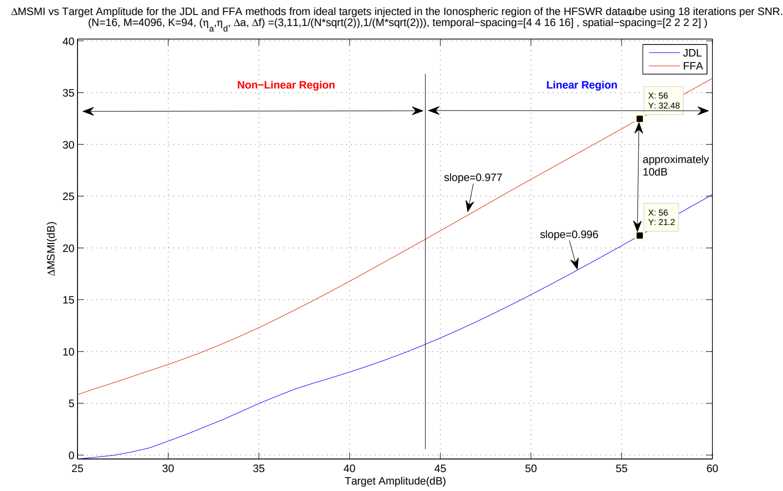

Figure 4.24: ΔMSMI versus target amplitude for JDL, and FFA algorithms

tude plots for both the JDL and FFA algorithm. We use 18 (a relatively small number) iterations per target amplitude to obtain the curve. The range of Target Amplitudes we scan over is from 25dB to 60dB in steps of 1dB. Again since we have no means to determine the actual noise power, we use Target Amplitude as a proxy for SNR. Figure 4.24 shows the results for the JDL and FFA methods. In this simulation we use 3 angle and 11 doppler bins for the JDL method and a spatial and temporal partitioning sequence of $[2, 2, 2, 2]$ and $[4, 4, 16, 16]$ respectively for the FFA method. The JDL's nonlinear region seems to extend well into the linear region of the FFA method before itself entering into its linear region(at around 44dB target amplitude). The slope of both curves in their linear region is very close to 1, and the difference between the curves is approximately 10dB in the linear region. These results reemphasize the superior performance of the FFA method in a more credible fashion.

These simulations indicate that the FFA method appears to be a highly practical method that performs well in real target detection scenarios under limited sample support, few available DoF, and at a relatively low complexity for HFSWR applications.

The FFA algorithm as reviewed here was shown to provide significant performance gains over other reduced DoF schemes such as JDL [11]. The next section describes a generalization of this scheme wherein the partitions are interleaved with each other.

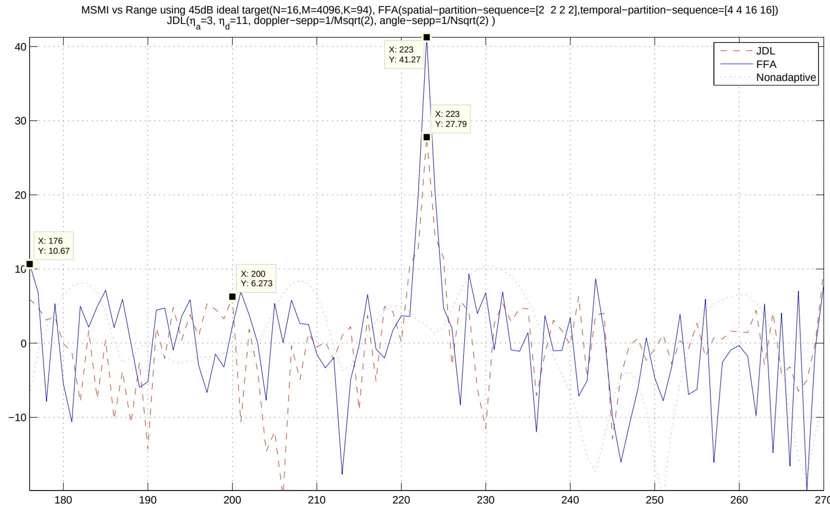

Figure 4.25: MSMI vs Range plots for using the Nonadaptive, JDL, and FFA methods to detect an ideal target in Ionospheric clutter region. All 4096 pulses are used in this simulation.

4.7 Interleaved FFA Description

In this section we will develop a more general partitioning scheme for the FFA method. We will denote this new partitioning method when combined with the FFA method as the Interleaved FFA method for reasons that will become obvious shortly. In the regular FFA method described above we partitioned the spatial and temporal dimensions at each depth into *disjoint* partitions whose union resulted in the original spatio-temporal data cube. However it is not imperative that the partitions be disjoint, and it is possible to select a partitioning scheme in which the different spatial and/or temporal partitions overlap, thus reusing the same DoF more than once in each of the overlapping partitions.

To formalize this scheme, we begin with several definitions(refer to Figure 4.29). We define d_N and d_M as the length of the spatial and temporal partitions respectively at a certain depth of the FFA tree. Next we define s_N and s_M as the distance between two consecutive spatial and temporal partitions. Figure 4.29 might represent either the data-matrix of space-time samples at a certain depth or the corresponding steering matrix in the direction of the look angle and doppler.

In the example shown in Fig. 4.29, $d_N = 3$, $s_N = 2$, $d_M = 5$, and $s_M = 3$. If we assume the space-time matrix in Fig. 4.29 to represent the steering matrix at a certain depth, where z_s and z_t are the current spatial and temporal spacings, we can write the spatio-temporal partition steering

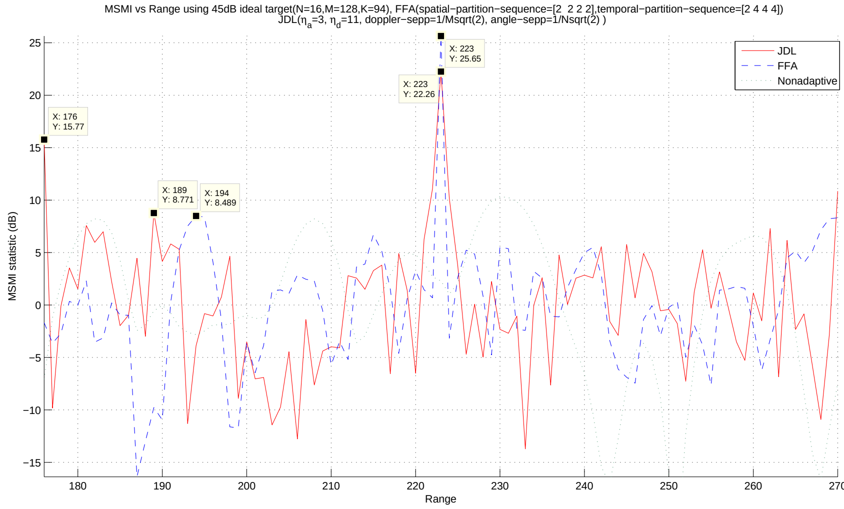

Figure 4.26: MSMI vs Range plots for using the Nonadaptive, JDL, and FFA methods to detect an ideal target in Ionospheric clutter region. Only 128 pulses are used in this simulation.

matrix of the $(n, m)^{\text{th}}$ partition in terms of the first steering matrix as follows,

$$\mathbf{v}_{nm} = \mathbf{v}_{11} z_s^{(n-1)s_N} z_t^{(m-1)s_M}, \tag{4.74}$$

where $n \in [1, \ldots, \lfloor N/(s_N+1) \rfloor]$ and $m \in [1, \ldots, \lfloor M/(s_M+1) \rfloor]$. The remainder of the FFA method remains unchanged except that at the final stage after all the spatio-temporal partitions of the current depth have been processed, we update the spatial and temporal spacings at the new depth as follows,

$$\begin{aligned} z_s' &= z_s^{s_N}, \\ z_t' &= z_t^{s_M}, \end{aligned} \tag{4.75}$$

where z_s and z_t are the spatial and temporal spacings at the depth we just processed, and where z_s' and z_t' are the new spatial and temporal spacings. At every new depth a different interleaved partitioning scheme can be used (assuming that it is valid).

Next we will address the issue of determining which combinations of d_N, s_N, d_M, and s_M are valid at a certain depth. Assuming we are at depth i, we can write,

$$\begin{aligned} M(i) &= d_M(i) + (M(i+1) - 1) \times s_M(i), \\ & \qquad\qquad\qquad i = 0, \cdots, t-1, \\ \Rightarrow M(i+1) &= \frac{M(i) - d_M(i)}{s_M(i)} + 1, \end{aligned} \tag{4.76}$$

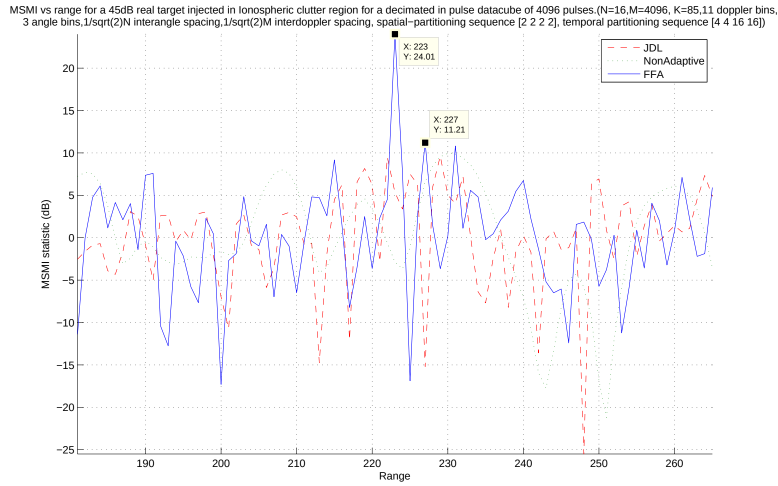

Figure 4.27: MSMI vs Range plots for using the Nonadaptive, JDL, and FFA methods to detect a real target in Ionospheric clutter region. All 4096 pulses are used in this simulation.

where

$$\begin{aligned} M(0) &= M_0, \\ M(t) &= 1, \end{aligned} \tag{4.77}$$

where t is assumed to be the final depth of the FFA tree, and $M(0)$ is the initial spatial dimension of the space-time steering or data matrices. Similarily for the temporal dimension we can write,

$$N(i+1) = \frac{N(i) - d_N(i)}{s_N(i)} + 1, \tag{4.78}$$

where,

$$\begin{aligned} N(0) &= N_0, \\ N(t) &= 1. \end{aligned} \tag{4.79}$$

We can also write $M(i)$ in terms of M_0, $d_M(k)$, and $s_M(k)$ for $k \in [0, \ldots, i-1]$ as follows,

$$M(i) = \left\lfloor \frac{M_0 - \sum_{k=0}^{i-1} \left(\prod_{l=0}^{k-1} s_M(l) \left[d_M(k) - s_M(k) \right] \right)}{\prod_{k=0}^{i-1} s_M(k)} + 1 \right\rfloor, \tag{4.80}$$

where

$$d_M(-1) = s_M(-1) = 1. \tag{4.81}$$

A similar expression is valid for the temporal dimension. Noting that the size of the spatial and temporal dimensions at depth $i+1$ must be less than or equal to the size of the spatial and temporal

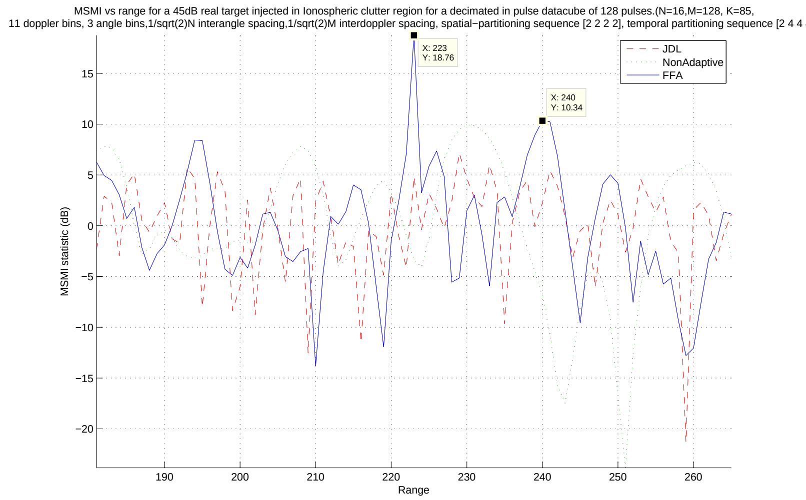

Figure 4.28: MSMI vs Range plots for using the Nonadaptive, JDL, and FFA methods to detect a real target in Ionospheric clutter region. Only 128 pulses are used in this simulation.

dimensions respectively at depth i, we can write,

$$\begin{aligned}1 \leqslant d_M(i) &\leqslant \lfloor s_M(i)\,[M(i)-1] - M(i) \rfloor \\ &= \left\lfloor \left(\frac{M_0 - \sum\limits_{k=0}^{i-1} \left(\prod\limits_{l=0}^{k-1} s_M(l)\,[d_M(k) - s_M(k)] \right)}{\prod\limits_{k=0}^{i-1} s_M(k)} + 1 \right) [s_M(i) - 1] - s_M(i) \right\rfloor \end{aligned} \tag{4.82}$$

where we substituted the value of $M(i)$ in the above expression. A similar expression can be derived for s_M":

$$\begin{aligned}1 \leqslant s_M(i) &\leqslant \left\lfloor \frac{M(i) - d_M(i)}{M(i) - 1} \right\rfloor \\ &= \left\lfloor \frac{M_0 - \sum\limits_{k=0}^{i-1} \left(\prod\limits_{l=0}^{k-1} s_M(l)\,[d_M(k) - s_M(k)] \right) + \prod\limits_{k=0}^{i-1} s_M(k) - d_M(i) \prod\limits_{k=0}^{i-1} s_M(k)}{M_0 - \sum\limits_{k=0}^{i-1} \left(\prod\limits_{l=0}^{k-1} s_M(l)\,[d_M(k) - s_M(k)] \right)} \right\rfloor \end{aligned} \tag{4.83}$$

Similar expressions can be derived for the temporal dimension. Thus upon specifying either the $s_M(i)$ or $d_M(i)$ at a certain depth i, we can choose an upper bound for the other. It is interesting to note that if we set $s_M(i) = d_M(i)$ and $s_N(i) = d_N(i)$ at every depth, the interleaved FFA simplifies to the regular FFA described in the previous section.

A final point worth mentioning is that it is not necessary to use all the spatial and temporal elements contained within each partition in the modified AMF solution. It is possible to only select

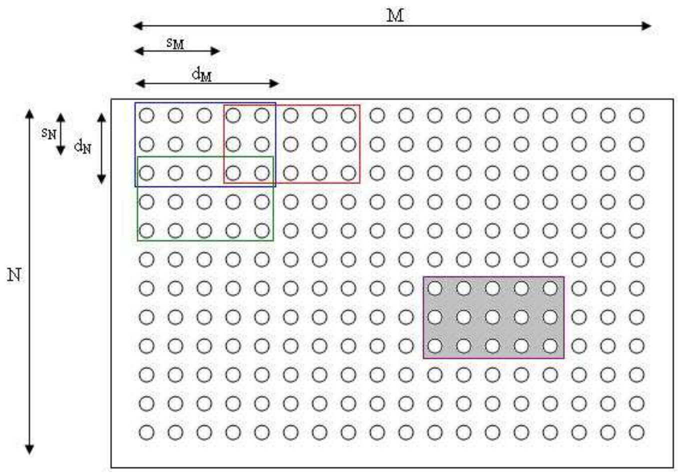

Figure 4.29: A representation of the Interleaved-FFA method.

every k^{th} spatial and every l^{th} temporal element within each spatio-temporal partition. However the same spatial and temporal sampling must be selected for all the partitions at the current depth. Note that using fewer DoF per partition might lead to worse results than if all the DoF were used since fewer DoF are harnessed towards suppressing the clutter and enhancing the target.

This new interleaved partitioning scheme is better than the original, since the different combinations of DoF yield different intermediate statistics which better utilize the set of available DoF at a certain depth to null the residual interference and enhance the buried target. Another advantage of the interleaved FFA is that this partitioning scheme can be used with values of M and N that are prime or do not admit numerous factors. Unfortunately using interleaved partitions further complicates the task of choosing an optimal spatio-temporal partition sequence, as we are no longer bound to utilizing combinations of the factors of N and M, and the performance and complexity is now determined by 4 parameter sequences (ignoring the available sample support K) instead of only 2.

4.8 Complexity Analysis

Earlier we performed a complexity analysis on the regular FFA method and were able to derive an expression for its asymptotic behavior. The interleaved FFA method's complexity is somewhat more difficult to characterize since it involves twice the number of parameters as the regular FFA method. At a certain depth, i, and for the spatial and temporal partitions $d_N(i)$, $s_N(i)$, $d_M(i)$, and

$s_M(i)$ we must process $M'N'$ spatio temporal partitions using the modified AMF method, where,

$$\begin{aligned} M'(i) &= \left\lfloor \frac{M(i) - d_M(i)}{s_M(i)} + 1 \right\rfloor, \\ N'(i) &= \left\lfloor \frac{N(i) - d_N(i)}{s_N(i)} + 1 \right\rfloor. \end{aligned} \tag{4.84}$$

The AMF solution requires the inversion of an $M'N' \times M'N'$ matrix, which is $O((M'N')^3)$. Thus the complexity of the interleaved FFA method can be shown to be,

$$\begin{aligned} T_{\text{int}\,FFA} &= \sum_{i=1}^{\max(k_N,k_M)} \left\{ N'(i)M'(i)O((d_N(i)d_M(i))^3) \right\} \\ &= \sum_{i=1}^{\max(k_N,k_M)} \left\{ \left\lfloor \frac{N(i) - d_N(i)}{s_N(i)} + 1 \right\rfloor \left\lfloor \frac{M(i) - d_M(i)}{s_M(i)} + 1 \right\rfloor O((d_N(i)d_M(i))^3) \right\}, \end{aligned} \tag{4.85}$$

where the value of $M(i)$ is given in Eqn. (4.80), and that of $N(i)$ can be inferred from Eqn. (4.80). This expression compares to

$$T_{FFA} = \sum_{d=1}^{\max(k_N,k_M)} \left\{ \frac{NM}{\prod_{i=1}^{d} n_i m_i} O\left((n_d m_d)^3\right) \right\} = \sum_{d=1}^{\max(k_N,k_M)} \left\{ \left(\prod_{i=d}^{\max(k_N,k_M)} n_i m_i \right) O\left((n_d m_d)^2\right) \right\}, \tag{4.86}$$

for the original FFA algorithm.

As can be seen by comparing the expressions outlining the complexities of the two algorithms being evaluated, it is not straight forward to draw a definite conclusion. We can manipulate the various parameters of each algorithm to favor either algorithm, in terms of complexity. However the performance is directly related to the parameters and is often characterized by an inverse relationship with the complexity, and therefore a tradeoff is inevitable. In general, in terms of computation load, JDL has the distinct advantage that it requires the solution of single size-$\eta_a\eta_d$ matrix while the FFA approach (in both its versions) requires several AMF solutions. On the other hand, in terms of performance, the regular FFA algorithm uses all NM adaptive DoF while the JDL is restricted to just $\eta_a\eta_d$ DoF. The interleaved FFA method goes beyond the regular FFA method and reuses the DoF at each depth in the computation of intermediate statistics, and outperforms the regular FFA method for a reasonably good choice of partitioning sequences.

4.8.1 Unequal Partitions

So far we have assumed that the partitions at each depth are of equal size, i.e., all the spatio-temporal 'rectangles' at a certain depth are of equal dimensions. Although this might seem necessary so as to be able to express all the partial steering matrices at a given level in terms of the first partial steering matrix at this level, we will show that this requirement can be easily bypassed by using steering vectors that do not have constant phase progressions from element to element and/or pulse to pulse. We will begin by assuming unequal but disjoint spatial and temporal partitions. Starting with the original data-square of dimension $N \times M$ at a given look range we segment the spatial and temporal dimensions into N_1 and M_1 unequal partitions respectively. We only require that each of the spatial and temporal partitions be disjoint in order to simplify the presentation. We can surely use an interleaved partitioning scheme as described in the previous section to bypass the disjoint partitions requirement as well as use unequal partition sizes at any given depth of the FFA tree structure. For the time being, however, we will assume disjoint partitions so as to avoid overcomplicating an inherently simple idea. As a result we we will partition the spatial dimension into N_1 disjoint partitions of lengths $\left\{n_1^{(1)}, n_2^{(1)}, \ldots, n_{N_1}^{(1)}\right\}$ where, $\sum\limits_{l=1}^{N_1} n_l^{(1)} = N_0$. Similarly, we will partition the temporal dimension into M_1 disjoint partitions of lengths $\left\{m_1^{(1)}, m_2^{(1)}, \ldots, m_{M_1}^{(1)}\right\}$ where, $\sum\limits_{k=1}^{M_1} m_k^{(1)} = M_0$.

Denote as $\mathbf{X}_{lk}^{(1)}$ and $\mathbf{V}_{lk}^{(1)}$ the (l,k)-th spatio-temporal partition of the space-time snapshot and steering matrix at the current depth respectively. Here $l = 1, 2, .., N_1$ and $k = 1, 2, .., M_1$. We next process each spatio-temporal partition in a similar manner to the regular FFA method, except instead of dividing by $\left(\mathbf{w}_{lk}^{(1)}\right)^H \mathbf{v}_{11}^{(1)}$ where $\mathbf{v}_{11}^{(1)}$ is the actual first space-time partition of the steering vector at the current depth, we replace $\mathbf{v}_{11}^{(1)}$ by the vectorized form of a steering matrix partition of dimension $n_l^{(1)} \times m_k^{(1)}$ whose first entry coincides with the first entry of the space-time steering matrix of the current depth. We will denote this improvised steering matrix partition as $\mathbf{V}_{11}^{(1)}(n_l^{(1)}, m_k^{(1)})$. Thus the expression for the (l,k)'th statistic evaluated from the $(l,k)^{\text{th}}$ spatio-temporal data partition would be given by

$$\begin{aligned} y_{lk}^{(1)} &= \frac{\left(\mathbf{w}_{lk}^{(1)}\right)^H x_{11}^{(1)}}{\left(\mathbf{w}_{lk}^{(1)}\right)^H \mathbf{v}_{11}^{(1)}(n_l^{(1)}, m_k^{(1)})} = \frac{\left(\mathbf{w}_{lk}^{(1)}\right)^H \left(noise_{11}^{(1)} + clutter_{11}^{(1)}\right)}{\left(\mathbf{w}_{lk}^{(1)}\right)^H \mathbf{v}_{11}^{(1)}(n_l^{(1)}, m_k^{(1)})} + \frac{\left(\mathbf{w}_{lk}^{(1)}\right)^H \left(\xi v_{lk}^{(1)}\right)}{\left(\mathbf{w}_{lk}^{(1)}\right)^H \mathbf{v}_{11}^{(1)}(n_l^{(1)}, m_k^{(1)})}, \\ &= s_{lk}^{(1)} + \xi p_{lk}^{(1)}, \end{aligned} \tag{4.87}$$

where,

$$p_{lk}^{(1)} = \frac{\left(\mathbf{w}_{lk}^{(1)}\right)^H v_{lk}^{(1)}}{\left(\mathbf{w}_{lk}^{(1)}\right)^H \mathbf{v}_{11}^{(1)}(n_l^{(1)}, m_k^{(1)})}. \tag{4.88}$$

is the (l,k)'th entry of the next depth's spatio-temporal steering matrix. Thus by updating the steering matrix at each depth we are not forced to rely on a preservation of a linear phase shift throughout the depth of the FFA-tree structure. In fact the steering matrix need not be characterized by any phase relationship amongst its entries; it suffices to know the form of the steering matrix at any given depth in order to be able to perform the FFA processing at that depth. Actually this is also true for the AMF method which does not impose a particular form that should be strictly adhered to by the steering matrix. The only strict requirement is that the steering matrix be known apriori so that it may be used in the computation of the weight vector.

Thus it is possible to use unequal partition sizes at each depth, and still be able to perform FFA processing. A further generalization of the FFA scheme is the combination of unequal partition sizes at every depth with the use of interleaved sequences. This generalized form of the FFA could prove to be very powerful, as it no longer requires N and M to be integers with numerous factors, and it allows the possibility of DoF 'recycling' which improves the detection capability of the algorithm.

A final yet very interesting thing to note, is that since we are not bound by any phase preservation rule we need not divide by $\left(\mathbf{w}_{lk}^{(1)}\right)^H \mathbf{v}_{11}^{(1)}$ to preserve a constant phase shift from element to element after each processing stage. In fact we do not even need to use rectangular partitions. We can simply choose any number of space-time elements at any random position in the current data-square and subject them to a modified AMF processing. The resulting statistics can be grouped into a new 'data-square' and reprocessed again in the forthcoming stage. Since we are free to choose as many combinations of space-time elements to process at a given depth, we can end up with the same, fewer , or more, number of elements at the next stage. As a result the method looses the FFT like structure that originally inspired its development. In fact this method has no structural pattern and becomes increasingly difficult to analyze. There are literally an infinite number of ways to process a given cube using this unstructured method, and one can no longer think in the direction of optimization. A practical implementation might rely on randomly choosing H bundles of elements at every stage, performing the modified AMF on each bundle, then regrouping the resulting statistics into a new vector. The sizes of each bundle could be chosen in such a way as to yield decreasing subsequent vector sizes until a final statistic has been obtained. The ΔMSMIs could then be tested for, and if the results are unsatisfying, the processing could be repeated using a different choice of bundle sizes and/or element-bundle mappings. Another possibility would be to repeat the above processing for a variety of element-bundle mappings, and averaging the final statistic.

4.8.2 Simulation Results

In this section we will evaluate the performance of the FFA algorithm using probability of detection versus SNR curves. We will compare the performance of the FFA algorithm with that of the JDL approach. We will also evaluate the performance of the interleaved-FFA as a first step towards a more general characterization of the FFA method.

4.8.3 Probability of Detection versus SNR

In this section we will provide probability of error versus SNR plots for a given CFAR using the FFA and JDL algorithms for the HFSWR radar scenario. To generate sufficient HFSWR data-cubes for a Monte-Carlo simulation we will use the model for Ionospheric clutter developed by Dr. Riddolls, and implemented in Matlab by Dr. Ravan. The thresholds required for the MSMI statistic correspond to a probability of false alarm $P_{fa} = 0.1$. This results in thresholds of 9.1dB and 5.4dB for the FFA and JDL methods respectively. To compute the threshold we generated a data-cube with 4000 ranges, 4096 pulses, and 16 elements, and computed the MSMI statistic (using each of the above three methods) of each of the 4000 ranges in the absence of a target. We used 200 secondary ranges centered (as best as possible) around each look range in order to estimate the corresponding error covariance matrix. For this simulation we used an localized processing region for the JDL method, composed of $\eta_a = 11$ angle and $\eta_d = 3$ Doppler bins, with angle and doppler spacings of $(1/N\sqrt{2})$ and $(1/M\sqrt{2})$ respectively, where $N = 16$ and $M = 4096$. For the FFA method we used a spatial partitioning sequence of $[4, 2, 2]$ and a temporal partitioning sequence of $[16, 16, 16]$. For the interleaved-FFA method we used the following set of sequences: $d_M = [2, 8, 8, 2, 16]$, $s_M = [2, 8, 8, 2, 16]$, $d_N = [2, 2, 2, 2, 1]$, and $s_N = [2, 2, 2, 2, 1]$. It should be noted that the chosen sequences for both the FFA and interleaved-FFA methods were selected somewhat arbitrarily (we wanted to choose small values for the size of the partitions) and without any optimization in mind. The number of trials we chose for the Monte-Carlo simulation was 4000. It should be noted that for this simulation we used 200 secondary ranges for the covariance estimation step. Figure 4.30 plots the probability of detection versus SNR for each of the methods being evaluated, using the pre-computed thresholds mentioned above.

As can be seen from the plots, the FFA method is up to 9dB better than the JDL method for a probability of detection of 0.5. It should be noted that the number of secondary ranges used in

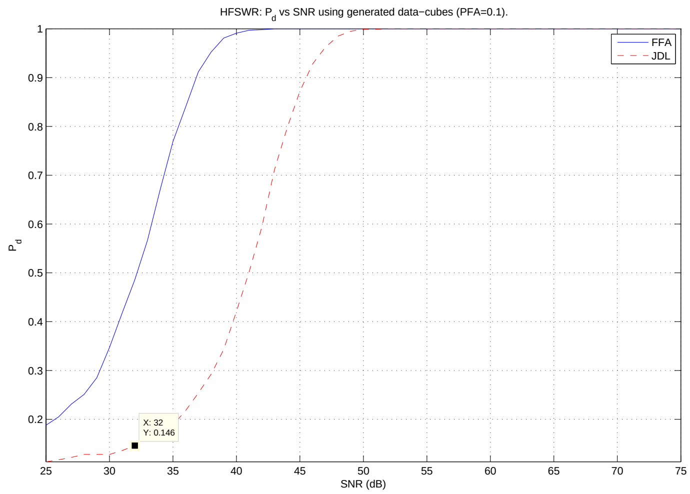

Figure 4.30: Probability of detection versus SNR for a PFA=0.1, using JDL, regular FFA, and interleaved FFA methods.

this simulation is by far smaller than the required $2MN$ secondary samples required by the RMB rule for optimal AMF performance. Unfortunately, given the time required, a corresponding plot for the interleaved-FFA could not be obtained.

For completeness we will also evaluate the performance of the interleaved-FFA method (for the chosen set of sequences) in the case of measured HFSWR data using both ideal and real targets. Figures 4.31 and 4.32 show a ΔMSMI versus range plot for the interleaved-FFA methods in both ideal and real target scenarios. As can be noted from the two figures, the interleaved-FFA method outperforms the regular FFA method by approximately 3.5dB in the ideal target case and by 5.4dB in the real target case. We repeat the above simulations for a reduced DoF scenario where only 128 of the available 4096 pulses are used (after appropriate decimation in pulse). In this simulation we use a spatial-partitioning sequence of $[2, 2, 2, 2]$ and temporal-partitioning sequence of $[2, 4, 4, 4]$ for the regular FFA method, and the following set of sequences for the interleaved-FFA method: $d_M = [2, 34, 16, 1]$, $s_M = [2, 2, 13, 1]$, $d_N = [2, 5, 3, 2]$, and $s_N = [2, 1, 1, 2]$ due to low sample support (only 80 secondary samples used). We also use a spatial sampling sequence of $[1, 2, 1, 1]$, and a temporal sampling sequence of $[1, 21, 2, 1]$. The results for both ideal and real targets are shown in Figures 4.33 and 4.34 respectively, where it can be seen that the interleaved-FFA method is able to discriminate the 45dB ideal (real) targets with a margin of 8dB (7dB) over the regular FFA method. As noted in an earlier report, the 45dB *does not* indicate the target signal-to-noise ratio.

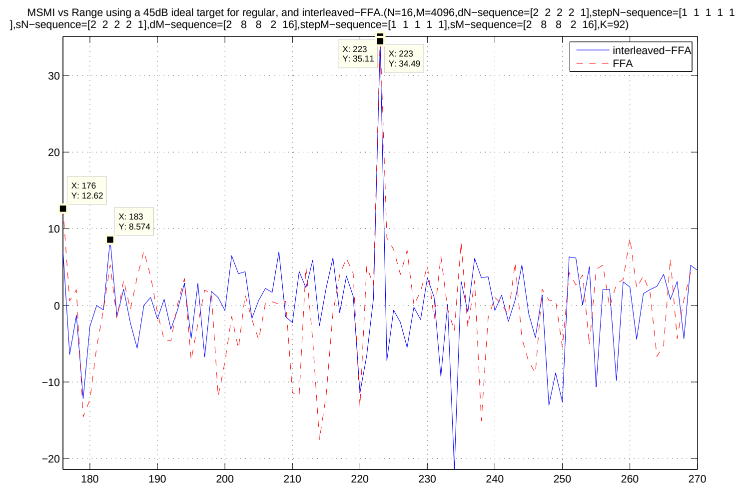

Figure 4.31: MSMI versus range plot for interleaved-FFA method using 4096 pulses in an ideal target scenario

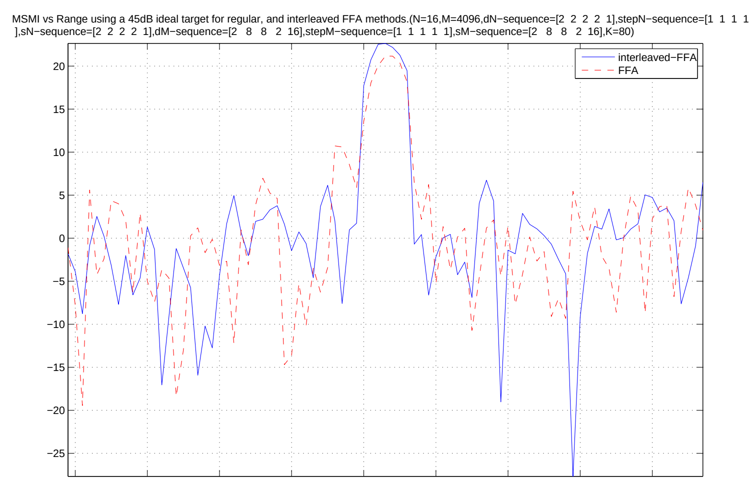

Figure 4.32: MSMI versus range plot for interleaved-FFA method using 4096 pulses in a real target scenario

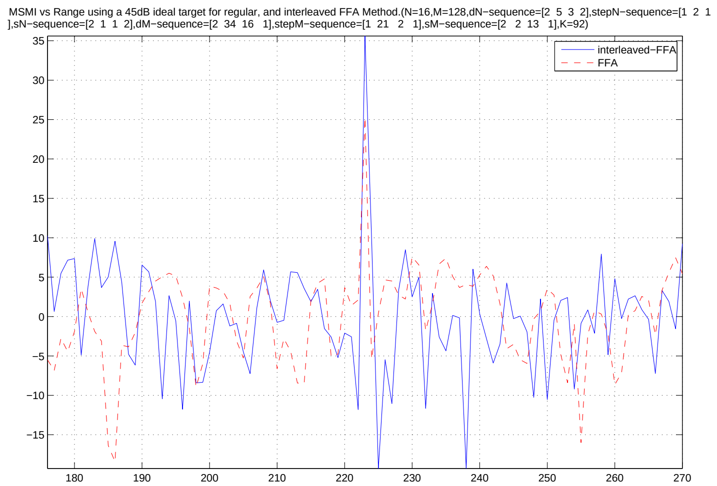

Figure 4.33: MSMI versus range plot for interleaved-FFA method using 128 pulses in an ideal target scenario

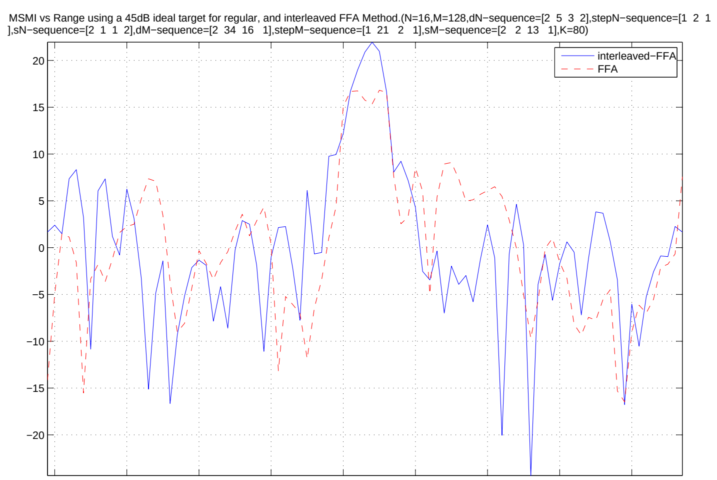

Figure 4.34: MSMI versus range plot for interleaved-FFA method using 128 pulses in a real target scenario

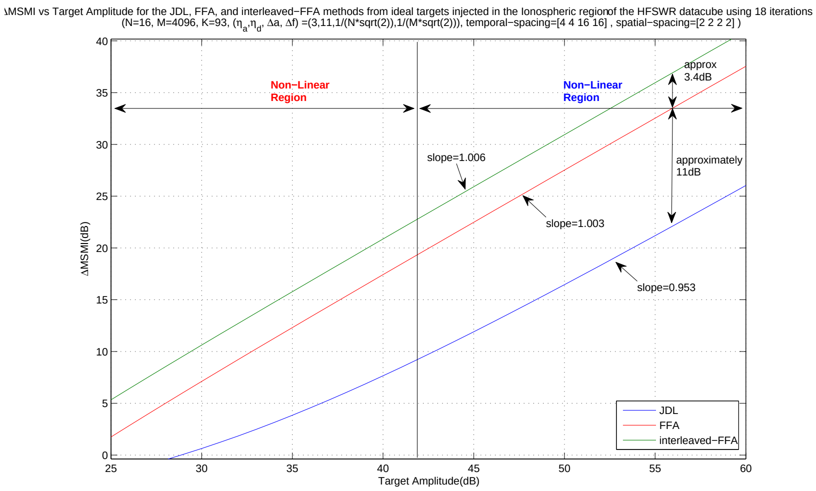

Figure 4.35: ΔMSMI versus target amplitude for JDL, FFA, and interleaved-FFA algorithms

We also provide a ΔMSMI versus target amplitude plot for the case of the interleaved-FFA method as a further indication of its enhanced performance. We choose to include this plot because it describes the performance of the interleaved-FFA on measured data (as opposed to generated data) in a much more convincing fashion than can be portrayed using MSMI versus Range plots. For convenience we also include the ΔMSMI versus target amplitude plots for each of the FFA and JDL methods. The sequences we used in this simulation for the interleaved-FFA method are $d_M = [2, 8, 8, 2, 16]$, $s_M = [2, 8, 8, 2, 16]$, $d_N = [2, 2, 2, 2, 1]$, and $s_N = [2, 2, 2, 2, 1]$, while the number of secondary range samples used is 93. As can be seen from Figure 4.35, the performance of the interleaved-FFA method (for the chosen sequence and sample support) by far exceeds that of the JDL method, and is also better than that of the regular FFA method by approximately $3.4dB$.

4.9 Summary and Conclusions

The FFA method is a very robust and practical method, that seems to have good promise in HFSWR applications. However so far we have only begun to scratch the surface of this new technique, and their is still much work that can be done to further our understanding of how to better select the various parameters that characterize the FFA method to improve performance, decrease running time, and combat interference. The more generalized version of the FFA method described in this report also invites further investigation, as well as a more thorough complexity analysis. We do not yet know how to choose the various parameters that characterize the FFA method so as to maximize it performance, nor do we fully understand how these parameters impact target discrimination and clutter mitigation. A more elaborate investigation of the FFA technique is necessary before the full picture portrayed by this elegant method can be seen.

In this section we introduced a generalized form of the FFA method introduced in Section 4.6. We also used the new Ionospheric clutter model developed by Dr. Riddolls to generate HFSWR datacubes corrupted by Ionospheric clutter, which we required to generate probability of detection versus SNR plots that better characterize the performance of the FFA method. We also provided a ΔMSMI versus target amplitude plots for the interleaved-FFA method and used it to further describe the performance of this more general version of the FFA as applied to measured HFSWR.

Chapter 5

Conclusion

This project has dealt with the development of practical space-time adaptive processing schemes for the high frequency surface wave radar operated by Defense Research and Development Canada. The performance of this radar system is largely limited by ionospheric clutter. Our goal was two-fold: (a) develop a data model to accurate simulate ionospheric clutter and (b) investigate STAP algorithms and approaches to determine the best knowledge-based STAP (KB-STAP) approach. Both goals were met successfully.

With regard to the simulation of ionospheric clutter, we investigated two potential data models: that of Fabrizio [1] and Riddolls [20]. At the start of the project it appeared that Fabrizio's model was the most well-developed and had a clear path to implementation. The model treats ionospheric clutter as the superposition of multiple modes. The parameters of these modes can be estimated, for example, using measured data for "training". However, in implementing this model we found that the parameter estimation process resulted in physically un-realizable solutions. One should not construe this as a criticism of the model since that was developed for over-the-horizon radar and the data sets we were trying to emulate were HFSWR data.

A considerable portion of this project dealt with implementing the model of Riddolls [20]. The theoretical underpinnings of this model match that of HFSWR and this theory was justified in our testing of our implementation. The data cubes generated by our scheme closely matched that of the measured data. In this regard, the implementation and testing of this model is a significant accomplishment in this project.

The other aspect of this effort dealt with KB-STAP for HFSWR. The ability to detect a weak target is largely restricted by the ionospheric clutter. The HFSWR data sets are characterized by the very large available degrees of freedom (M = 4096 pulses, N =16 elements) and the extremely restricted available training data (approximately 80 range cells in total including oversampled range cells). Our initial effort, therefore, was focused on the implementation and testing of popular reduced DoF algorithms (with attendant reductions in required training). We implemented and tested the joint domain localized (JDL), direct data domain (D^3), hybrid and parametric adaptive matched filter (PAMF) schemes. The JDL and hybrid schemes were considered the most promising.

The continued investigation of these schemes was superseded by the development of a new space-time adaptive processing scheme: the fast fully adaptive (FFA) algorithm. This scheme draws its inspiration from the popular FFT scheme - the overall fully adaptive scheme that uses all NM DoF is sub-divided into a a nested process of significantly smaller "fully" adaptive problems. At each level, only limited secondary training samples are required but the overall solution exploits all available DoF.

In this report we have detailed the FFA algorithm and its variants, the interleaved FFA scheme and a general scheme with potentially unequal spacings. The performance of these schemes are documented using the measured data and the simulated data as described above.

Bibliography

[1] G. Fabrizio, "Space-time characterization and adaptive processing of ionospherically propagated hf signals," Ph.D. dissertation, The University of Adelaide,, 2000.

[2] R. J. Riddolls, "a model of radio wave propagation in ionospheric irregularities for prediction of high-frequency radar performance," Defense Research Development Canada - Ottawa, Tech. Rep. TM 2006-284, December 2006.

[3] M. Ravan, O. Saleh, R. Adve, and K. Plataniotis, "KB-STAP implementaion for HFSWR: Progress report," Tech. Rep. W7714-060999/001/SV, June 2007.

[4] ——, "KB-STAP implementaion for HFSWR: Progress report," Tech. Rep. W7714-060999/001/SV, September 2007.

[5] R. S. Adve, T. B. Hale, M. C. Wicks, and P. A. Antonik, "Ground moving target indication using knowledge based space-time adaptive processing," in *Proceedings of the 2000 IEEE International Radar Conference*, May 2000, washington, DC.

[6] R. S. Adve, T. B. Hale, and M. C. Wicks, "Knowledge based adaptive processing for ground moving target indication," *DSP: A Review Journal*, available on-line August 2005. Also available at http://www.comm.utoronto.ca/ rsadve/publications.html.

[7] ——, "Joint domain localized adaptive processing in homogeneous and non-homogeneous environments. part II: Non-homogeneous environments," *IEE Proceedings on Radar Sonar and Navigation*, vol. 147, no. 2, pp. 66–73, April 2000.

[8] R. Adve, P. Missailidis, and K. Plataniotis, "KB-STAP implementaion for HFSWR: Progress report," Tech. Rep. W7714-060999/001/SV, March 2007.

[9] H. Wang and L. Cai, "On adaptive spatial-temporal processing for airborne surveillance radar systems," *IEEE Transactions on Aerospace and Electronic Systems*, vol. 30, no. 3, pp. 660–699, July 1994.

[10] R. S. Adve, T. B. Hale, and M. C. Wicks, "Joint domain localized adaptive processing in homogeneous and non-homogeneous environments. part I: Homogeneous environments," *IEE Proceedings on Radar Sonar and Navigation*, vol. 147, no. 2, pp. 57–65, April 2000.

[11] M. Ravan, O. Saleh, R. Adve, and K. Plataniotis, "KB-STAP implementaion for HFSWR: Progress report," Tech. Rep. W7714-060999/001/SV, December 2007.

[12] J. W. X. Kun Lu, "A piecewise parametric method based on polynomial phase model to compensate ionospheric phase contamination," *IEE Proceedings on Radar, Sonar and Navigation*, 2003.

[13] K. Lu, X. Liu, and Y. Liu, "A multiple-Sweep-Frequencies Scheme Based on Eigen-decomposition to Compensate Ionospheric Phase Contamination," in *Proceedings of the 2003 IEEE International Radar Conference*, September 2003, pp. 706–710.

[14] A. Bourdillon, "Use of of maximum entropy spectral analysis to improve ship detection by over-the-horizon radar," *Radio Science*, vol. 22, no. 2, pp. 313–320, 1987.

[15] J. Parent and A. Bourdillon, "A method to correct hf sky-wave backscattered signals for ionosphere frequency modulation," *IEEE Transactions on Antennas and Propagation*, vol. 36, no. 1, pp. 127–135, 1988.

[16] Y. Abramovich, S. Anderson, and Soloman, "Adaptive ionospheric distortion correction techniques for HF sky-wave radar," in *Proceedings of the 1994 IEEE National Radar Conference*, 1994.

[17] M. D. M. Paul D. Mountcastle, "Monte-carlo simulation of ionospheric scintillation," in *Proceedings of the 2002 IEEE Radar Conference*, 2002.

[18] C. J. Coleman, "A model of HF sky wave radar clutter," *Radio Science*, vol. 31, no. 4, pp. 869–876, August 1996.

[19] ——, "A propagation model for HF radiowave systems," in *Conference Record of the 1994 IEEE Military Communications Conference, 1994*, vol. 3, October 1994, pp. 875–879.

[20] R. J. Riddolls, "A model of radio wave propagation in ionospheric irregularities for prediction of high-frequency radar performance," Defense Research Devlopment Canada - Ottawa, Tech. Rep. DRDC Ottawa TM 2006-284, December 2006.

[21] R. Riddolls, "Measurement of ionospheric density irregularity spectra for evaluation of next-generation OTH radar systems," in *Proceedings of the 2007 Union of Radio Science International Conference*, July 2007.

[22] H. C. Chan, "Characterization of ionospheric clutter in HF surface-wave radar," Defense Research Devlopment Canada - Ottawa, Tech. Rep. DRDC Ottawa TR 2003-114, September 2003.

[23] L. Sevgi, A. Ronsford, and H. C. Chan, "An integrated maritime surveillance system based on high-frequency surface wave radars, part 1: Theoretical background and numerical simulations," *IEEE Antennas and Propagation Magzine*, vol. 43, no. 4, pp. 28–42, 2001.

[24] ——, "An integrated maritime surveillance system based on high-frequency surface wave radars, part 2: Operational status and system performance," *IEEE Antennas and Propagation Magzine*, vol. 43, no. 4, pp. 52–63, 2001.

[25] L. Sevgi, "Stochasting modelling of target detection and tracking in surface wave radar," *International Journal of Numerical Modelling*, vol. 11, no. 3, pp. 168–181, 1998.

[26] R. H. Anderson and J. L. Krolik, "Track association for over-the-horizon radar with a statistical ionospheric model," *IEEE TRANSACTIONS ON SIGNAL PROCESSING*, vol. 50, no. 11, pp. 2632–2643, November 2002.

[27] H. Leong, "Adaptive nulling of skywave interference using horizontal dopole antennas in a coastal surveillance HF surfave wave radar system," Defense Research Establishment Ottawa, Tech. Rep. 506722 (System Number), June 1997.

[28] ——, "Adaptive suppression of interference in HF surfave wave radar using auxiliary horizontal dopole antennas," Defense Research Establishment Ottawa, Tech. Rep. 1336 (Report Number), Sept. 1998.

[29] ——, "A comparison of sidelobe cancellation techniques using auxiliary horizontal and vertical antennas in HF surface wave radar," Defense Research Establishment Ottawa, Tech. Rep. DREO TM 1999-121, November 1999.

[30] H. C. Chan and E. K. L. Tung, "An investigation in interference suppression in HF surface wave radar," Defense Research Establishment Ottawa, Tech. Rep. DREO TR 2000-028, December 1999.

[31] Y. Abramovich, S. Anderson, Y. Lyudviga, N. Spencer, P. Turcaj, and B. Hibble, "Space-time adaptive techniques for ionospheric clutter mitigation in HF surface wave radar systems," in *Proceedings of the 2004 IEEE International Radar Conference*, 2004.

[32] G. A. Fabrizio, A. Farina, and M. Turley, "Spatial adaptive subspace detection in OTH radar," *IEEE Transactions on Aerospace and Electronic Systems*, vol. 39, no. 4, pp. 1407–1427, 2003.

[33] G. A. Fabrizio, L. L. Scharf, A. Farina, and M. Turley, "Ship detection with HF surface wave radar using short integration times," in *Proceedings of the 2004 IEEE International Radar Conference*, 2007.

[34] G. A. Fabrizio, G. J. Frazer, and M. Turley, "STAP for clutter and interference cancellation in a HF radar system," in *Proceedings of ICASSP 2006*, 2006.

[35] S. Kraut, L. L. Scharf, and T. McWhorter;, "Adaptive subspace detectors," *IEEE Transactions on Signal Processing*, vol. 49, no. 1, pp. 1–16, January 2001.

[36] G. A. Fabrizio and A. Farina, "GLRT-based adaptive processing for HF radar systems," in *Proceedings of the 2007 IEEE Radar Conference*, 2007.

[37] G. Li, L. Li, and R. Xu, "A novel adaptive beamforming method for non-stationary interference cancellation in HF surface wave radar," in *Proceedings of the 2004 IEEE International Radar Conference*, 2004.

[38] W. Xianrong, K. Hengyu, and W. Biyang, "Adaptive cochannel interference suppression based on subarrays for HFSWR," *IEEE Signal Processing Letters*, vol. 12, no. 2, pp. 162–165, Feb. 2005.

[39] W. Xianrong, C. Feng, and K. Hengyu, "Experimental trials on ionospheric clutter suppression for high-frequency surface wave radar," *IEE Proceedings on Radar, Sonar and Navigation*, vol. 153, no. 1, pp. 23–29, Feb. 2006.

[40] K. Lu and X. Liu, "STAP for clutter and interference cancellation in a HF radar system," in *Proceedings of ICASSP 2004*, 2004.

[41] K. Lu, X. Liu, and Y. Liu, "Ionospheric decontamination and sea clutter suppression for HF skywave Radars," *IEEE Journal of Oceanic Engineering*, vol. 30, no. 2, pp. 455–462, April 2005.

[42] A. Bourdillon, P. Dorey, and G. Auffray, "Ship echo discrimination in HF radar sea-clutter," in *Proceedings of the 2003 IEEE International Radar Conference*, 2003, pp. 584–587.

[43] S. Kraut, K.Harmanci, and J. Krolik, "Space-time adaptive processing for over-the-horizon spread-doppler clutter mitigation," in *Proceedings of the SAM signal Processing Workshop*, 2000.

[44] J. Ward, "Space-time adaptive processing for airborne radar," MIT Linclon Laboratory, Tech. Rep. F19628-95-C-0002, December 1994.

[45] I. S. Reed, J. Mallett, and L. Brennan, "Rapid convergence rate in adaptive arrays," *IEEE Transactions on Aerospace and Electronic Systems*, vol. 10, No. 6, pp. 853–863, Nov. 1974.

[46] L. Cai and H. Wang, "Performance comparisons of modified SMI and GLR algorithms," *IEEE Transactions on Aerospace and Electronic Systems*, vol. 27, no. 2, pp. 487–491, Apr. 1991.

[47] Y. Abramovich, A. Ghorokhov, and C. Demeure, "Adaptive verification of a general multivariate propagation model for ionospheric hf signals," in *Proceedings of the 1996 EUSIPCO*, 1996.

[48] T. K. Sarkar and N. Sangruji, "An adaptive nulling system for a narrow-band signal with a look-direction constraint utilizing the conjugate gradient method," *IEEE Transactions on Antennas and Propagation*, vol. 37, no. 7, pp. 940–944, July 1989.

[49] J. Roman, M. Rangaswamy, D. Davis, Q. Zhang, B.Himed, and J. Michels, "Parametric adaptive matched filter for airborne radar applications," *IEEE Transactions on Aerospace and Electronic Systems*, vol. 36, No. 2, pp. 677–692, 2000.

[50] J. Goldstein, L. Scharf, and I. Reed, "A multistage representation of the wiener filter based on orthogonal projections," *IEEE Transactions on Information Theory*, vol. 44, no. 7, pp. 2943–2959, July 1998.

[51] E. Yang, J. Chun, and R. Adve, "A hybrid d3-sigma delta stap algorithm in non-homogeneous clutter," *To appear, IEEE International Radar Conf.*, October 2007.

[52] S. Marple, *Digital Spectral Analysis with Applications*. Prentice Hall, 1987.